

Controllable formation of microparticles via microfluidic technique



A Dissertation Submitted in Partial Fulfillment of the Requirements  
for the Degree of Doctor of Engineering in Chemical Engineering

Department of Chemical Engineering

FACULTY OF ENGINEERING

Chulalongkorn University

Academic Year 2021

Copyright of Chulalongkorn University

การเกิดอนุภาคขนาดไมโครที่ควบคุมได้ด้วยเทคนิคไมโครฟลูอิดิกส์



วิทยานิพนธ์นี้เป็นส่วนหนึ่งของการศึกษาตามหลักสูตรปริญญาวิศวกรรมศาสตรดุษฎีบัณฑิต

สาขาวิชาวิศวกรรมเคมี ภาควิชาวิศวกรรมเคมี

คณะวิศวกรรมศาสตร์ จุฬาลงกรณ์มหาวิทยาลัย

ปีการศึกษา 2564

ลิขสิทธิ์ของจุฬาลงกรณ์มหาวิทยาลัย



นารินทร์ ไพบูลย์ : การเกิดอนุภาคขนาดไมโครที่ควบคุมได้ด้วยเทคนิคไมโครฟลูอิดิกส์. (Controllable formation of microparticles via microfluidic technique) อ.ที่ปรึกษาหลัก : ผศ. ดร.อภิรักษ์ สุทธิธรร  
 วัช, อ.ที่ปรึกษาร่วม : ดร.สุวิมล สุรัสโม,ดร.มิชาเอล คาพิล

ไมโครฟลูอิดิกส์แบบก่อยอด (Droplet microfluidic) เป็นเครื่องมือที่น่าสนใจในกระบวนการห่อหุ้ม (Encapsulation) เนื่องจากมีศักยภาพในการผลิตไมโครพาทิเคิล (Microparticles) และไมโครแคปซูล (Microcapsules) ที่มีขนาดสม่ำเสมอ มีการกระจายตัวของขนาดที่แคบ และยังสามารถควบคุมสมบัติได้ งานวิจัยนี้ได้ศึกษาการเตรียมหยดอิมัลชันแบบน้ำในน้ำมันสำหรับการเตรียมไมโครพาทิเคิลภายใต้สภาวะการทำงานที่หลากหลายรวมถึงชนิดของของเหลวที่หลากหลาย โดยทำการเก็บข้อมูลจากผลการทดลอง 12 ชุดการทดลองมากกว่า 100 ผลการทดลองในอุปกรณ์ไมโครฟลูอิดิกส์ 2 ขนาด พบว่าระบบ narrowing jet และ tip streaming สามารถผลิตอนุภาคแบบหยดที่มีขนาดสม่ำเสมอและยังสามารถผลิตได้ในปริมาณมาก โดยงานวิจัยนี้ได้เสนอความสัมพันธ์ระหว่างสัดส่วนของขนาดอนุภาคแบบหยดต่อขนาดของจุดเชื่อมของอุปกรณ์ไมโครฟลูอิดิกส์ กับตัวเลขไร้มิติ 3 ตัว ได้แก่ อัตราส่วนของกรไหล อัตราส่วนของความหนืดและตัวแปรไร้หน่วยคาพิลารี ซึ่งพบว่าความสัมพันธ์ดังกล่าว เป็นประโยชน์ในการผลิตอนุภาคแบบหยดที่มีขนาดสม่ำเสมอ ซึ่งสามารถคาดการณ์และควบคุมได้ในระบบกระบวนการไหลสูง ในการเตรียมไมโครพาทิเคิลหรือไมโครแคปซูลโดยใช้แอลจินตเป็นตัวพาในระบบไบเฟส จำเป็นต้องศึกษาที่วิธีการเชื่อมขวางของตัวพาด้วย จึงมีการศึกษาการเกิดเจลภายในของอนุภาคแอลจินตโดยใช้แคลเซียมเอทิลีนไดอะมีนเตตระอะซิติก (Ca-EDTA) ซึ่งเป็นสารที่ละลายน้ำได้ มาใช้เป็นแหล่งแคลเซียมเพื่อควบคุมการเชื่อมต่อและรูปร่างของอนุภาค โดยทำการศึกษาผลของความเร็วอิมัลซิฟิเคชัน ความเข้มข้นของ Ca-EDTA เวลาเชื่อมขวางต่อลักษณะทางสัณฐานวิทยา ร้อยละผลผลิต สมบัติเชิงกล สมบัติทางรีโอโลยี และปริมาณแคลเซียม เพื่อศึกษาความหนาแน่นของการเชื่อมขวาง (crosslink density) ด้วยวิธีอิมัลซิฟิเคชัน จากนั้นเลือกสภาวะที่เหมาะสมที่สุดของการเกิดเจลภายในถูกใช้ในเตรียมไมโครพาทิเคิลด้วยเทคนิคไมโครฟลูอิดิกส์ ซึ่งผลปรากฏว่าเทคนิคไมโครฟลูอิดิกส์สามารถเตรียมอนุภาคแอลจินตแบบไมโครพาทิเคิลที่มีความสม่ำเสมอมากกว่าเมื่อเทียบกับวิธีอิมัลซิฟิเคชัน จากนั้นได้ศึกษาการเตรียมอนุภาคไมโครแคปซูลที่มีแกนเดี่ยว (Single-core-microcapsules) และหลายแกน (Multiple-core-microcapsules) โดยใช้การเชื่อมต่อกันของอุปกรณ์ไมโครฟลูอิดิกส์ 2 ชั้น หยดน้ำมันซึ่งเป็นแกนของอนุภาคไมโครแคปซูลถูกเตรียมขึ้นก่อนจากนั้นจึงถูกคลุมด้วยอัลจินตแล้วจึงเชื่อมขวางอนุภาคให้เป็นเปลือกของแข็ง งานวิจัยนี้ศึกษาขนาดของอนุภาคและความหนาของเปลือกไมโครแคปซูลที่สภาวะการไหลต่างๆ โดยผลจากงานวิจัยนี้สามารถนำไปประยุกต์การใช้งานด้านการห่อหุ้มอาหารและยาได้ต่อไป

สาขาวิชา	วิศวกรรมเคมี	ลายมือชื่อนิสิต .....
ปีการศึกษา	2564	ลายมือชื่อ อ.ที่ปรึกษาหลัก .....
		ลายมือชื่อ อ.ที่ปรึกษาร่วม .....
		ลายมือชื่อ อ.ที่ปรึกษาร่วม .....

## 5971483321 : MAJOR CHEMICAL ENGINEERING

KEYWORD: Microfluidic, Microparticle, Alginate

Narin Paiboon : Controllable formation of microparticles via microfluidic technique. Advisor:  
Asst. Prof. Dr. APINAN SOOTTITANTAWAT Co-advisor: Dr. Suvimol Surassmo, Dr. Michael  
Kappl

Droplet microfluidics is an interesting tool in the encapsulation process due to its potentiality for microparticles and microcapsules fabrication with uniform size and narrow size distribution. The formation of water-in-oil (W/O) emulsion droplets in a microfluidic flow-focusing device for microparticles production were investigated under a wide selection of operating parameters together with liquid materials. Experimental results of 12 data sets from over 100 experiments in two different-sized channels were assessed. The stable narrowing jet and tip streaming regime noticeably created monodisperse droplet formation with high throughput. The droplet size to junction size has been found to correlate with the three dimensionless numbers which are flow rate ratio ( $Q_c/Q_d$ ), viscosity ratio ( $\mu_c/\mu_d$ ), and capillary number (Ca). This correlation will be beneficial in predictable and controllable monodisperse droplets in a high flow process regime. To generate either the microparticles or microcapsules using alginate as a carrier in a biphasic system, it is necessary to focus on the crosslinking method. The internal gelation of alginate microparticles using a water-soluble calcium-ethylenediaminetetraacetic acid (Ca-EDTA) as a calcium source was studied to control crosslink density and the shape of particles. Effects of emulsification speed, Ca-EDTA concentration, crosslinking time on morphology, %yield, mechanical properties, rheological properties, and Ca content for crosslink density were studied in the oil (W/O) emulsification method. The optimum condition of internal gelation was used in the microfluidic technique which generated monodisperse alginate particles with more uniformity and controllable size. Then, single- and multiple-core-shell microcapsules were fabricated by connecting two flow-focusing microfluidic chips. The oil droplets as a core were first formed and then entrapped with the alginate substance via microfluidic technique and crosslinked to a solid shell. Droplet size and shell thickness over the operating parameters were studied. The resultant would show a great potential application in the field of food and pharmaceutical encapsulation.

Field of Study: Chemical Engineering

Student's Signature .....

Academic Year: 2021

Advisor's Signature .....

Co-advisor's Signature .....

Co-advisor's Signature .....

## ACKNOWLEDGEMENTS

I would like to sincere gratitude to my thesis advisor, Asst. Prof. Dr. Apinan Soottitantawat. This research effort would not be possible without his enthusiastic guidance, valuable suggestions, friendly discussions, and persistent supervision which are indispensable for the completion of the thesis work.

My appreciation also goes to my co-advisor, Dr. Suvimol Surassmo for her technical support, especially helping with the guidance of laboratory instruments. Special thanks to all researchers, research assistants, technicians, and all friends at National Nanotechnology Center, National Science and Technology Development Agency for all their support. I would like to extend my thank to Dr. Uracha Rungsardthong Rukthanonchai for her extensive guidance and deep discussion of this work.

I also would like to thank Dr. Michael Kappl who kindly supported and suggested me during my research at the Max Plank Institute for Polymer Research, Mainz, Germany. Many thanks also go to technicians, staff, and friends in the department of Prof. Hans-Jürgen Butt for their help, suggestion, and warm welcome.

Furthermore, I would like to thank Prof. Dr. Sarawut Rimdusit, Asst. Prof. Dr. Nattaporn Tonanon, and Asst. Prof. Dr. Rungtiwa Methaapanon for their useful discussions and participation on the thesis committee.

The authors are grateful for funding from the Thailand Graduate Institute of Science and Technology (TGIST) and the National Science and Technology Development Agency (NSTDA), Thailand (Grant no. TG-55-09-60-003D). Also, this work has been supported by the Overseas Research Experience Scholarship for Graduate Student by the Department of Chemical Engineering, Faculty of Engineering and Graduate School, Chulalongkorn University, Thailand.

Last, but not least I would like to show my gratitude to my dear parents for their love and encouragement. Your support always allows me to face all challenges bravely.

Narin Paiboon

## TABLE OF CONTENTS

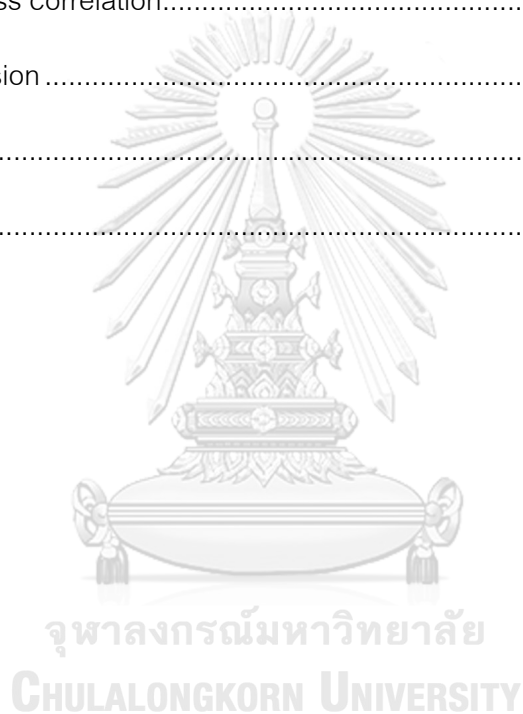
	Page
.....	iii
ABSTRACT (THAI) .....	iii
.....	iv
ABSTRACT (ENGLISH) .....	iv
ACKNOWLEDGEMENTS .....	v
TABLE OF CONTENTS .....	vi
LIST OF TABLES.....	x
LIST OF FIGURES.....	xi
Chapter 1 Introduction.....	1
1.1 Background and motivation.....	1
1.2 Objective of this research.....	4
1.3 Scope of research .....	4
1.3.1 Hydrodynamic control of droplet formation in narrowing jet and tip streaming regime using microfluidic flow-focusing.....	4
1.3.2 Internal gelation of alginate microparticle prepared by emulsification and microfluidic method: Effect of Ca-EDTA as a calcium source .....	4
1.3.3 Fabrication of single- and multiplied-core-shell of alginate microcapsules via microfluidic flow-focusing .....	5
1.4 Expected benefits.....	5
Chapter 2 Theory literature review.....	6
2.1 Encapsulation technology .....	6

2.2 Microfluidic technique .....	10
2.2.1 Droplet microfluidics .....	11
2.2.2 Droplet-microfluidic geometry .....	11
2.2.3 Droplet generation .....	12
2.2.4 Dimensionless number .....	14
2.2.5 Parameters of droplet formation .....	16
2.2.6 Model of droplet formation .....	19
2.3 Biopolymer .....	23
2.4 Alginate .....	26
2.4.1 Alginate-particle formation .....	27
2.4.2 Alginate-particle gelation .....	28
2.5 Droplet microfluidic in encapsulation technology .....	31
Chapter 3 Experiment .....	34
3.1 Chemical and reagents .....	34
3.2 Experimental procedures .....	34
3.2.1 Hydrodynamic control of droplet formation in narrowing jet and tip streaming regime using microfluidic flow-focusing .....	34
3.2.2 Internal gelation of alginate microparticle prepared by emulsification and microfluidic method: Effect of Ca-EDTA as a calcium source .....	36
3.2.3 Fabrication of single- and multiplied-core-shell of alginate microcapsules via microfluidic flow-focusing .....	38
3.3 Fluid properties .....	39
3.4 Characterization .....	40
3.4.1 Morphology .....	40



3.4.2 %Yield .....	40
3.4.3 AFM measurement .....	40
3.4.4 Rheological properties .....	41
3.4.5 Ca content.....	41
Chapter 4 Hydrodynamic control of droplet formation in narrowing jet .....	42
and tip streaming regime using microfluidic flow-focusing .....	42
4.1 Flow regime inside the channel .....	44
4.2 Effect of fluids Interfacial tension on the droplet formation in the narrowing jet and tip streaming regime .....	48
4.3 Flow regime .....	51
4.4 Effect of flow rate ratio and viscosity ratio on the ratio of droplet size to junction size.....	54
4.5 Dimensionless correlation for droplet formation in the narrowing jet and tip streaming regimes .....	58
Chapter 5 Internal gelation of alginate microparticle prepared by emulsification and microfluidic method: Effect of Ca-EDTA as a calcium source .....	64
5.1 Mechanism of internal gelation using Ca-EDTA as a calcium source .....	66
5.2 Emulsification/internal gelation .....	68
5.2.1 Effect of emulsification speed .....	69
5.2.2 Effect of Ca-EDTA concentration .....	70
5.2.3 Effect of crosslinking time .....	75
5.2.4 Internal and external crosslink .....	76
5.3 Microfluidic/internal gelation.....	83

Chapter 6 Fabrication of single- and multiplied-core-shell of alginate microcapsules via microfluidic flow-focusing .....	87
6.1 Effect of flow rate on droplet regime.....	90
6.2 Effect of the dispersed phase flow rate of the first microfluidic chip ( $Q_1$ ).....	94
6.3 Effect of the continuous phase flow rate of the first microfluidic chip ( $Q_2$ ) .....	98
6.4 Effect of the continuous phase flow rate of the second microfluidic chip ( $Q_3$ ) ...	101
6.5 Dimensionless correlation.....	106
Chapter 7 Conclusion .....	109
REFERENCES .....	111
VITA .....	129



## LIST OF TABLES

	Page
Table 1 The common method of encapsulation.....	7
Table 2 Dimensionless parameters in droplet microfluidics .....	15
Table 3 The models for a droplet size in T-junction microfluidics.....	21
Table 4 The common method of biopolymer-based particle forming.....	24
Table 5 Physical properties of fluids at 25°C (a) density ( $\rho$ ) and viscosity ( $\mu$ ); (b) interfacial tension ( $\sigma$ ).....	39
Table 6 Fluid viscosity ratios ( $\mu_c/\mu_d$ ).....	55
Table 7 Droplet size correlation.....	62

## LIST OF FIGURES

	Page
Figure 1 Microstructure and nanostructure particle.....	6
Figure 2 The field of microfluidic liquid handing.....	11
Figure 3 The three main droplet-microfluidic geometries used .....	12
Figure 4 The droplet generation with different regime in cross-flow, co-flow and flow-focusing geometries. ....	13
Figure 5 The effect of dispersed-phase viscosity from various type of fluid with droplet size .....	16
Figure 6 Relationship between droplet size and flow rates .....	17
Figure 7 Droplet flow pattern as a function of flow rate ratio.....	18
Figure 8 The effect capillary number of continuous phase at different flow rate ratio ....	18
Figure 9 (a) a schematic illustration of the T junction microfluidics (b) an agreeable experimental and model derived results of P. Garstecki et al.'s study .....	19
Figure 10 A fitting experimental and model results of J. H. Xu et al.'s study .....	20
Figure 11 (a) a schematic illustration of the cross-junction microfluidics (b) an agreeable experimental and model derived results of J. Tan et al.'s study.....	22
Figure 12 (a) a schematic illustration of the cross-junction microfluidics (b) an agreeable predicted results and simulated results of H. Liu et al.'s study .....	22
Figure 13 (a) a schematic illustration of the microfluidics (b) an agreeable experimental and model derived results of F. Lapierre et al.'s study .....	23
Figure 14 Structure of alginate.....	26
Figure 15 Design of alginate particle.....	26
Figure 16 Method of alginate-particle formation.....	27

Figure 17 Gelling mechanism of calcium crosslinked alginate (egg-box like conformation).....	28
Figure 18 Mechanism of external gelation for bead formation.....	29
Figure 19 Mechanism of internal gelation for bead formation.....	29
Figure 20 Mechanism of inverse gelation for liquid-core capsule formation .....	30
Figure 21 Mechanism of interfacial gelation for oil-core capsule formation.....	30
Figure 22 Schematic of droplet formation of experiment. ....	35
Figure 23 Geometry of droplet microfluidic channel.....	35
Figure 24 Schematic of emulsification method for alginate microparticle. ....	36
Figure 25 Schematic of microfluidic method for alginate microparticle.....	37
Figure 26 Schematic of core-shell microcapsule formation for experiment.....	38
Figure 27 Flow regime inside the channel of 2%(w/w) alginate solution in Miglyol <sup>®</sup> 812 oil with constant dispersed phase at flow rate of (I) 14.68 $\mu\text{l}/\text{min}$ and (II) 49.33 $\mu\text{l}/\text{min}$ .....	47
Figure 28 Micrograph emulsion droplets of 2%(w/w) alginate solution in Miglyol <sup>®</sup> 812 oil with constant dispersed phase at flow rate of (I) 14.68 $\mu\text{l}/\text{min}$ and (II) 49.33 $\mu\text{l}/\text{min}$ .....	48
Figure 29 Micrograph emulsion droplets of 2%(w/w) alginate solution in Miglyol <sup>®</sup> 812 oil with Experimental images of fluid characteristics in a microfluidic channel showing the effect of interfacial tension ( $\sigma$ ) on tip streaming state at different continuous phase flow rate ( $Q_c$ ) .....	50
Figure 30 Flow regime of 2%(w/w) alginate droplets in Miglyol <sup>®</sup> 812 oil at various capillary numbers of dispersed phase ( $Ca_d$ ) and continuous phase ( $Ca_c$ ) in junction depth 100 $\mu\text{m}$ .....	53
Figure 31 Effect of flow rate ratio ( $Q_c/Q_d$ ) on droplet size ( $d_p$ ) normalized by junction size ( $j$ ).....	57

Figure 32 Correlations of droplet size ( $d_p$ ) normalized by junction size ( $j$ ) at varied capillary number of continuous phase ( $Ca_c$ ).....	59
Figure 33 Comparison of the calculated and experimental data.....	61
Figure 34 Illustration of the internal crosslink process.....	66
Figure 35 Optical micrographs of alginate particles prepared via emulsification method by 2%(w/w) sodium alginate solution crosslinked with 0.1M Ca-EDTA from the acetic acid concentration of (a) 0 %(v/v), (b) 0.005%(v/v), (c) 0.01%(v/v), (d) 0.05%(v/v), (e) 0.1%(v/v), (f) 0.5%(v/v), (g) 1%(v/v), and (h) 2%(v/v). ....	68
Figure 36 Optical images of alginate beads from samples stirred with (a) a magnetic stirrer at 400 rpm; a high-speed homogenizer at (b) 5,000 rpm; (c) 7,500 rpm; and (d) 10,000 rpm.....	70
Figure 37 Optical micrographs of alginate particles prepared by 2%(w/w) sodium alginate solution with (a) 0.1M (b) 0.2M (c) 0.3M and (d) 0.5M of Ca-EDTA. ....	71
Figure 38 AFM height images of alginate particles prepared by 2%(w/w) sodium alginate solution with (a) 0.1M (b) 0.2M (c) 0.3M and (d) 0.5M of Ca-EDTA.....	73
Figure 39 Rheological characterization of internal gelation of 2%(w/w) alginate particles (a) strain dependence when Ca-EDTA of 0.1M (b) frequency dependence at different concentration of Ca-EDTA. ....	74
Figure 40 Effect of crosslinking time on frequency dependence of $G'$ and $G''$ of 2%(w/w) alginate particle crosslinked with 0.1M Ca-EDTA at different crosslinking time. ....	76
Figure 41 SEM image of (A)-(D) alginate beads which (A1),(A2) internal gelation of Ca-EDTA of 0.1M; (B1),(B2) external gelation at 0.037M, (C1),(C2) 0.074M, and (D1),(D2) 0.185M of $CaCl_2$ ; alginate particles which (E1),(E2) internal gelation of 0.1M Ca-EDTA; (F)-(H) internal gelation of 0.1M Ca-EDTA and, then external gelation at (F1),(F2) 0.037M, (G1),(G2) 0.074M, and (H1),(H2) 0.185M of $CaCl_2$ .....	78

Figure 42 AFM height images of internal gelation of 2%(w/w) alginate particles crosslinked with 0.1M Ca-EDTA and then external gelation with CaCl <sub>2</sub> at (a) 0.037M (b) 0.074M and (c) 0.185M.....	79
Figure 43 (a) Frequency dependence of G' and G'' and (b) tan $\delta$ of internal gelation of 2%(w/w) alginate particles crosslinked with 0.1M Ca-EDTA and then external gelation with CaCl <sub>2</sub> at different concentration.....	80
Figure 44 EDX analysis of (a) internal gelation of 2%(w/w) alginate particles crosslinked with 0.1M Ca-EDTA (b) 2%(w/w) alginate particles crosslinked with 0.1M Ca-EDTA and then external gelation with 0.185M CaCl <sub>2</sub> , and %Weight of Ca on (c) internal gelation of alginate particles prepared by 2%(w/w) sodium alginate solution at different Ca-EDTA concentration (d) the 2%(w/w) sodium alginate which internal crosslink with 0.1M Ca-EDTA and then external gelation at different concentration of CaCl <sub>2</sub> .....	82
Figure 45 Optical micrographs of alginate particles prepared via microfluidic method by 2%(w/w) sodium alginate solution with (a) 0.1M (b) 0.2M (c) 0.3M and (d) 0.5M of Ca-EDTA.....	84
Figure 46 Effect of operating condition in microfluidic method; (a-c) experimental images of fluid characteristics in microfluidic channel, and (d-f) micrograph of 2%(w/w) alginate droplet in MCT oil system in a junction depth of 100 $\mu$ m. ....	86
Figure 47 Schematic of core-shell microcapsule fabrication using microfluidic flow-focusing. ....	88
Figure 48 Flow regime of MCT oil in 2%(w/w) alginate droplets at various flow rate of dispersed phase (Q <sub>1</sub> ) and continuous phase (Q <sub>2</sub> ) in first chip .....	90
Figure 49 Flow regime of (a) O/W droplets in first chip and (b) O/W/O droplets in second chip at various flow rate .....	92
Figure 50 Experimental images of fluid characteristics in a microfluidic channel at different continuous phase flow rate of second chip (Q <sub>3</sub> ).....	93

Figure 51 Experimental images of fluid characteristics in a microfluidic channel at different continuous phase flow rate of second chip ( $Q_3$ ).....	93
Figure 52 Experimental images of fluid characteristics in (A1-E1) the first microfluidic chip, (A2-E2) the second microfluidic chip, and (A3-E3) core-shell-microcapsules micrograph at constant $Q_2$ of 3.3 and $Q_3$ of 8.8 $\mu\text{l}/\text{min}$ .....	95
Figure 53 Effect of the dispersed flow rate of the first microfluidic chip ( $Q_1$ ) on core and shell diameter of microcapsules at constant $Q_2$ of 3.3 and $Q_3$ of 8.8 $\mu\text{l}/\text{min}$ . ....	95
Figure 54 Experimental images of fluid characteristic in (A1-D1) the first microfluidic chip, (A2-D2) the second microfluidic chip, and (A3-D3) core-shell-microcapsules micrograph at constant $Q_2$ of 18.8 and $Q_3$ of 86.0 $\mu\text{l}/\text{min}$ .....	97
Figure 55 Effect of dispersed flow rate of the first microfluidic chip ( $Q_1$ ) on core and shell diameter of microcapsules at constant $Q_2$ of 18.8 and $Q_3$ of 86.0 $\mu\text{l}/\text{min}$ .....	97
Figure 56 Experimental images of fluid characteristic in (A1-E1) the first microfluidic chip, (A2-E2) the second microfluidic chip, and (A3-E3) core-shell-microcapsules micrograph at constant $Q_1$ of 2.6 and $Q_3$ of 8.8 $\mu\text{l}/\text{min}$ .....	99
Figure 57 Effect of continuous flow rate of the first microfluidic chip ( $Q_2$ ) on core and shell diameter of microcapsules at constant $Q_1$ of 2.6 and $Q_3$ of 8.8 $\mu\text{l}/\text{ml}$ . ....	99
Figure 58 Experimental images of fluid characteristic in (A1-E1) the first microfluidic chip, (A2-E2) the second microfluidic chip, and (A3-E3) core-shell-microcapsules micrograph at constant $Q_1$ of 10.4 and $Q_3$ of 86.0 $\mu\text{l}/\text{min}$ .....	100
Figure 59 Effect of continuous flow rate of the first microfluidic chip ( $Q_2$ ) on core and shell diameter of microcapsules at constant $Q_1$ of 10.4 and $Q_3$ of 86.0 $\mu\text{l}/\text{min}$ . ....	101
Figure 60 Experimental images of fluid characteristic in (A1-E1) the second microfluidic chip, and (A2-E2) core-shell-microcapsules micrograph at constant $Q_1$ of 2.6 and $Q_2$ of 3.3 $\mu\text{l}/\text{min}$ .....	102
Figure 61 Effect of continuous flow rate of the second microfluidic chip ( $Q_3$ ) on core and shell diameter of microcapsules at constant $Q_1$ of 2.6 and $Q_2$ of 3.3 $\mu\text{l}/\text{min}$ . ....	102



Figure 62 Confocal laser scanning microscopy (CLSM) images of core-shell microcapsules at constant $Q_1$ of 2.6 and $Q_2$ of 3.3 $\mu\text{l}/\text{min}$ .....	103
Figure 63 Experimental images of fluid characteristic in (A1-E1) the first microfluidic chip, (A2-E2) the second microfluidic chip, and (A3-E3) core-shell-microcapsules micrograph at constant $Q_1$ of 10.4 and $Q_2$ of 18.8 $\mu\text{l}/\text{min}$ .....	104
Figure 64 Effect of continuous flow rate of the second microfluidic chip ( $Q_3$ ) on core and shell diameter of microcapsules at constant $Q_1$ of 10.4 and $Q_2$ of 18.8 $\mu\text{l}/\text{min}$ . ....	105
Figure 65 Confocal laser scanning microscopy (CLSM) images of core-shell microcapsules at constant $Q_1$ of 10.4 and $Q_2$ of 18.8 $\mu\text{l}/\text{min}$ .....	105
Figure 66 Effect of flow rate ratio ( $Q_2/Q_1$ ) on core size ( $d_{\text{core}}$ ) normalized by junction size (j) at different conditions. ....	108
Figure 67 Effect of flow rate ratio ( $Q_3/(Q_1+2Q_2)$ ) on shell size ( $d_{\text{shell}}$ ) normalized by junction size (j) at different conditions. ....	108

# Chapter 1

## Introduction

### 1.1 Background and motivation

The microfluidic technique has been applied in various fields including preparing small particles. Droplet microfluidics is an interesting tool in the encapsulation process due to its potentiality for microparticles, microcapsules, and microgels fabrication with uniform size and narrow size distribution. The monodisperse particles from droplet microfluidic present a sustained release of active ingredients compared with polydisperse particles made by a conventional method. Droplet size can also be controlled and fabricated at low energy consumption using a continuous process, resulting in reduced batch-to-batch variation. Droplet formation can be prepared by an emulsion of two immiscible fluids. Moreover, the microfluidic technique capacitates the fabrication of single, double, and higher-order multiple emulsions with a continuous process. Double emulsions are typically produced by a random shear in a two-step emulsification process resulting in poorly controlled structures. Accurate control of particle size, payloads, and thickness of particles via the microfluidic technique enables optimization of double emulsions with high uniformity and encapsulation efficiency.

The core-shell structure which is a droplet-in-droplet is precious when the active present different solubility with the carrier material. The shell which offers protection of core material can be a liquid membrane or converted to a solid shell for enhancing the performance in encapsulation application. Core-shell structure is not only able to encapsulate a hydrophobic-active ingredient but also shows a greater amount of active ingredient compared with ordinary microsphere.

Alginate, a biopolymer derived from brown seaweeds, is composed of (1-4)-linked  $\beta$ -D-mannuronic (M) and  $\alpha$ -L-guluronic acid residues (G). It is generally recognized as a safe (GRAS) material by the US Food and Drug Administration (FDA) and is a "not specific" acceptable daily intake (ADI). It is biodegradable, biocompatible, non-toxic, low cost, soluble in water, and thermally stable, resulting in one of the widely

used biomaterials for drug delivery, tissue engineering, biomedical, waste-water treatment, food, and supplement. The simplest and the most common technique to fabricate alginate particles for encapsulation applications in extrusion/external gelation, by which the alginate is extruded from a nozzle. The technique is called the dripping method. The alginate solution was extruded through a nozzle into the air phase. It became dropwise into a gelling bath containing cations such as calcium chloride ( $\text{CaCl}_2$ ), the most used ionic crosslinking agent. The cations diffuse from the outside into the internal alginate phase and form an alginate matrix, resulting in a gel-like state with the high crosslinking density of alginate reducing in the interior and the calcium at the surface. This was a limitation of external crosslinking. In addition, the dense peripheral matrix inhibits the exchange of ions between the particle core and the environment. Although the size of the bead is typically highly uniform, the main limitation of extrusion/external gelation is the large size of the alginate bead, which depends on the diameter of the nozzle extruder.

In the internal gelation, also known as *in situ* gelation, the divalent cations are released internally from the alginate phase. The alginate solution containing a calcium source would emulsify into an oil phase. The calcium remains in the solution but cannot crosslink with alginate chains. By adding acid, the detachment of the complex releases the calcium ions to react with the alginate chains. Therefore, the selection of a calcium source for internal gelation is critical. The gelation method is critical in controlling particle uniformity and crosslink density when using divalent ions. Slower gelation produces more uniform structures and greater mechanical properties. Moreover, internal gelation has an advantage in the biphasic system in the prevention of coagulation into large masses before properly hardening. Especially in the droplet microfluidic technique which needs to use immiscible fluid to fabricate droplets. The superior benefit of internal gelation is controlling the shape of particles. The spherical shape will be maintained in both microparticles and microcapsules.

Therefore, this research focused on droplet formation in droplet microfluidics. Initially, this study investigated droplet generation in a flow-focusing microfluidic device,

resulting in the production of monodisperse droplets over a wide range of fluid characteristics and operating parameters. The effects of fluid viscosity, interfacial tension, density, and flow rate were studied on droplet formation. The narrowing jet and tip streaming regimes were focused on and analyzed. The dimensionless correlation of these regimes was proposed to predict droplet size. The results show in chapter 4 with the title “Hydrodynamic control of droplet formation in narrowing jet and tip streaming regime using microfluidic flow-focusing”

Then, internal gelation of alginate crosslinking by using a water-soluble calcium-ethylenediaminetetraacetic acid (Ca-EDTA) complex was explored in chapter 5 with the title “Internal gelation of alginate microparticle prepared by emulsification and microfluidic method: Effect of Ca-EDTA as a calcium source”. The crosslinking network and particle reduction were used by two methods, including water in oil (W/O) emulsification and the microfluidic technique. The effect of emulsification speed, Ca-EDTA concentration, crosslinking time were investigated in terms of morphology, %yield, mechanical properties, rheological properties, and Ca content for considering crosslink density.

Finally, single- and multiple-core-shell microcapsules are fabricated in chapter 6. The title “Fabrication of single- and multiple-core-shell of alginate microcapsules via microfluidic flow-focusing” is presented. The oil droplets as a core are first forming and then entrap with a shell substance. The alginate with biocompatible, biodegradable, and non-toxic properties is formed as a shell via microfluidic technique and crosslinked to a solid shell. Droplet size and shell thickness over the operating parameters were studied. The resultant would show a great potential application in the field of food and pharmaceutical encapsulation.

## 1.2 Objective of this research

The main objectives of this present study are: (1) to study effect of processing parameters on droplet formation via microfluidic technique (2) to study effect of processing parameters on singled-core-shell microcapsules formation via microfluidic technique (3) to study effect of processing parameters on multiplied-core-shell microcapsules formation via microfluidic technique

## 1.3 Scope of research

### 1.3.1 Hydrodynamic control of droplet formation in narrowing jet and tip streaming regime using microfluidic flow-focusing

The pre-emulsion droplets are created from two immiscible fluids in flow-focusing devices. The flow rate ratio of fluid which is an operating parameter is controlled by the pressure pumps. A variety of fluids represent physical parameters which are density, viscosity, and interfacial tension. The scopes are shown below:

- **Droplet-microfluidic geometry:** Flow-focusing geometry with 100  $\mu\text{m}$  and 190  $\mu\text{m}$  etch depth (junction size of 105  $\mu\text{m}$  and 195  $\mu\text{m}$ ).
- **Fluid I (Oil phase):** Miglyol<sup>®</sup> 812 oil, Jojoba oil
- **Fluid II (Water phase):** 1%(w/w) alginate, 2%(w/w) alginate and 3%(w/w) alginate
- **Physical parameter:** Density, viscosity, and interfacial tension
- **Operating parameter:** Flow rate ratio

### 1.3.2 Internal gelation of alginate microparticle prepared by emulsification and microfluidic method: Effect of Ca-EDTA as a calcium source

Alginate particles are fabricated using internal gelation method. Ca source in the form of a water-soluble calcium-ethylenediaminetetraacetic acid (Ca-EDTA) complex was explored for crosslinking reaction. The crosslinking network and particle reduction were used by two methods: water in oil (W/O) emulsification and the microfluidic technique. The effect of emulsification speed, Ca-EDTA concentration, crosslinking time were investigated in terms of morphology, %yield, mechanical properties, rheological

properties, and Ca content for considering crosslink density. The optimal operating conditions in the microfluidic technique were determined to best control the size of the internal gelation-alginate particles.

### 1.3.3 Fabrication of single- and multiplied-core-shell of alginate microcapsules via microfluidic flow-focusing

Singled and multiplied-core-shell microcapsules are studied. The microcapsules are formed in a two-step process which using two flow-focusing geometry. The inner droplets are first forming then created double in the second channel. The flow rate ratio of fluid which is an operating parameter is controlled by the pressure pumps. The scopes are shown below:

- **Droplet-microfluidic geometry:** Two flow-focusing geometry
- **Core:** Active ingredient which soluble in oil phase
- **Shell:** Biopolymer such as alginate
- **Operating parameter:** Flow rate of fluid

### 1.4 Expected benefits

Expected benefits to be obtained from this research would be able to explain the effect of the physical and operating parameter, predict and control the droplet size from droplet microfluidics. The aim is also to fabricate a model of singled and multiplied-core-shell microcapsule for potential application in encapsulation.

## Chapter 2

### Theory literature review

#### 2.1 Encapsulation technology

Encapsulation is a technology that can control active agent release, improve the stability, and shelf life, and protect against external agents i.e., oxidation, UV, heat, acid, base, etc. by coating or entrapping an active ingredient with the wall material. The entrapped substances may be called the core material, active agent, actives, fill, internal phase, nucleus, or payload, and coating substances may be called the coating, membrane, shell, carrier material, wall material, external phase, or matrix. The type of encapsulation might be defined by its particle size; microencapsulation has a particle size range from 1  $\mu\text{m}$  to 1 mm and particle size under 1  $\mu\text{m}$  is nanoencapsulation. The various structure of microparticles and nanoparticles shown in Figure 1.

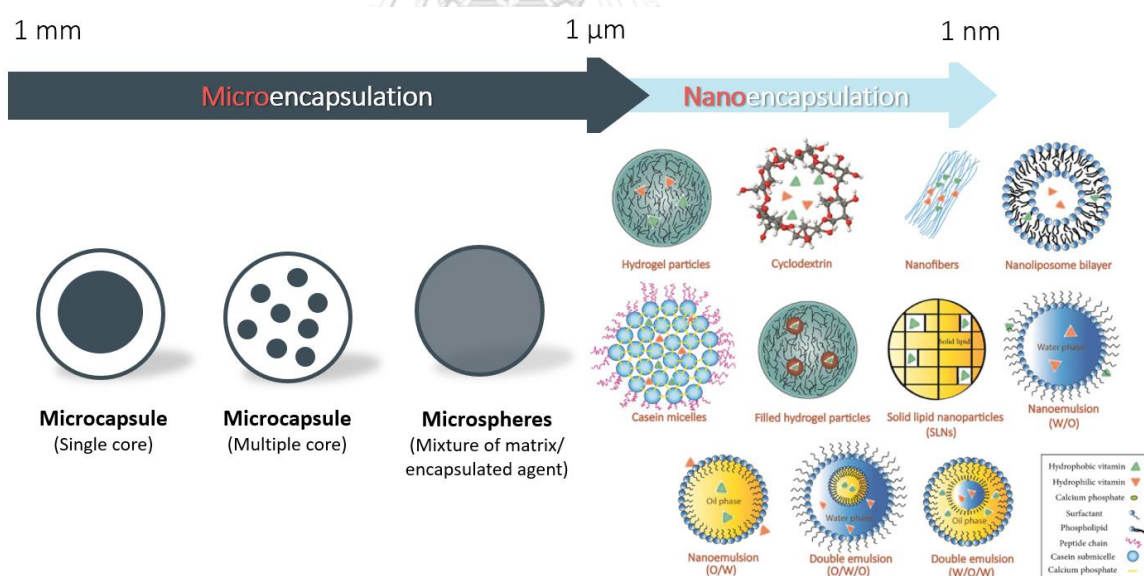


Figure 1 Microstructure and nanostructure particle.

A variety of encapsulation techniques are used. Table 1 show the method of encapsulation.

**Table 1** The common method of encapsulation [1]

Method	Process step	Structure	% Loading
Spray-drying	<ol style="list-style-type: none"> <li>1. Disperse or dissolve active in coating solution</li> <li>2. Atomize</li> <li>3. Dehydrate</li> </ol>	Matrix	5-50%
Fluid bed coating	<ol style="list-style-type: none"> <li>1. Fluidize active powder</li> <li>2. Spray coating</li> <li>3. Dehydrate or cool</li> </ol>	Coating	5-50%
Spray-chilling/ cooling	<ol style="list-style-type: none"> <li>1. Disperse or dissolve active in heated lipid solution</li> <li>2. Atomize</li> <li>3. Cool</li> </ol>	Matrix	10-20%
Melt injection	<ol style="list-style-type: none"> <li>1. Melt the coating</li> <li>2. Disperse or dissolve active in the coating</li> <li>3. Extrude through filter</li> <li>4. Cooling and dehydrating</li> </ol>	Matrix	5-20%
Melt extrusion	<ol style="list-style-type: none"> <li>1. Melt the coating</li> <li>2. Disperse or dissolve active in the coating</li> <li>3. Extrude with twin-screw extruder</li> </ol>	Matrix	5-40%
Emulsification	<ol style="list-style-type: none"> <li>1. Dissolve active and emulsifiers in water or oil phase</li> <li>2. Mix oil and water phases under shear</li> </ol>	Matrix	1-100%



**Table 1** The common method of encapsulation (cont.) [1]

Method	Process step	Structure	% Loading
Preparation of emulsions with multilayers	<ol style="list-style-type: none"> <li>1. Prepare O/W emulsions with lipophilic active in oil phase and ionic emulsifiers</li> <li>2. Mix with aqueous solution containing oppositely charged polyelectrolytes</li> <li>3. Remove excess of free polyelectrolytes (option)</li> <li>4. Repeat steps 2 and 3</li> </ol>	Capsule	1–90%
Coacervation	<ol style="list-style-type: none"> <li>1. Prepare O/W emulsions with lipophilic active in oil phase</li> <li>2. Mix under turbulent conditions</li> <li>3. Induce three immiscible phases</li> <li>4. Cool</li> <li>5. Crosslink (optionally)</li> </ol>	Capsule	40-90%
Preparation of microspheres via dropping	<ol style="list-style-type: none"> <li>1. Dissolve or disperse active in forming solution</li> <li>2. Drop into gelling bath</li> </ol>	Matrix	20-50%
Preparation of microspheres via emulsification	<ol style="list-style-type: none"> <li>1. Emulsify water with biopolymer in oil phase</li> <li>2. Add gelling agent under shear</li> </ol>	Matrix	20-50%

**Table 1** The common method of encapsulation (cont.) [1]

Method	Process step	Structure	% Loading
Co-extrusion	<ol style="list-style-type: none"> <li>1. Dissolve or disperse active in oil</li> <li>2. Prepare aqueous or fat coating</li> <li>3. Use a concentric nozzle, and press the oil phase through the inner nozzle and the water phase through the outer one</li> <li>4. Drop into gelling or cooling bath</li> </ol>	Capsule	70-90%
Inclusion complexation	<ol style="list-style-type: none"> <li>1. Mix carrier, active and water together</li> <li>2. Incubate and dry if necessary</li> </ol>	Molecular inclusion	5-15%
Liposome entrapment	<ol style="list-style-type: none"> <li>1. Disperse lipid molecules in water, with active agent in lipid or water phase</li> <li>2. Reduce size by high shear or extrusion</li> <li>3. Remove free active (option)</li> </ol>	Various	5-50%
Encapsulation by rapid expansion of supercritical fluid (RESS)	<ol style="list-style-type: none"> <li>1. Create a dispersion of active and dissolved or swollen shell material in supercritical fluid</li> <li>2. Release the fluid to precipitate the shell onto the active</li> </ol>	Matrix	20-50%
Freeze- or vacuum drying	<ol style="list-style-type: none"> <li>1. Dissolve or disperse active agent and carrier material in water</li> <li>2. Freeze the sample</li> <li>3. Drying under low pressure</li> <li>4. Grinding (option)</li> </ol>	Matrix	Various

## 2.2 Microfluidic technique

Microfluidics is the science that deals with a small ( $10^{-9}$ - $10^{-18}$  liters) volume fluid inside a micrometer-sized channel called a 'microfluidic device' or microfluidic chip'. Microfluidic devices have microchannels ranging from submicron to millimeters. It can be fabricated from a range of materials using different methods. The microfluidic system firstly focused on analytical chemistry, but recently developed in many areas such as chemistry, engineering, biotechnology, biochemistry, physics, and nanotechnology. The type of microfluidics is classified into continuous-flow microfluidics and digital microfluidics as shown in Figure 2.

Continuous-flow microfluidics enables to manipulation of the continuous flow of liquid through micro-channels devices by using external pressure pumps. Mixing and separation are the two main tasks of continuous-flow microfluidics. Mixing in microfluidics presents a controllable and rapid mixing. According to the laminar flow of fluid, mixing generally is occurred by molecular diffusion. Some biological processes such as protein folding and enzyme reactions that need initiators have used this technique in their reaction. The separation of particles can procure by an external force such as hydrodynamic, electrophoretic, dielectrophoretic, magnetophoretic, acoustic, and inertial forces. In terms of analytical chemistry and biological applications, separation in microfluidics is useful. The low Reynolds number leads to the controllable fluid. The high surface-to-volume ratio in microfluidics also reduces the required sample.

Droplet microfluidic is one kind of digital microfluidics that is perhaps called emulsion science. This allows to generate and control of uniform, reproducible droplets over the experiments' parameters. There are numerous benefits such as minimum reagent requirement, fast response rate, and low energy consumption. Another development in digital microfluidics is liquid marble which is a small droplet encapsulated by a hydrophobic coating. Due to a floating particle on a liquid surface, liquid marble has shown potential in biological applications, especially in cell culture. Moreover, microreactor is also used because of convenient transportation.[2]

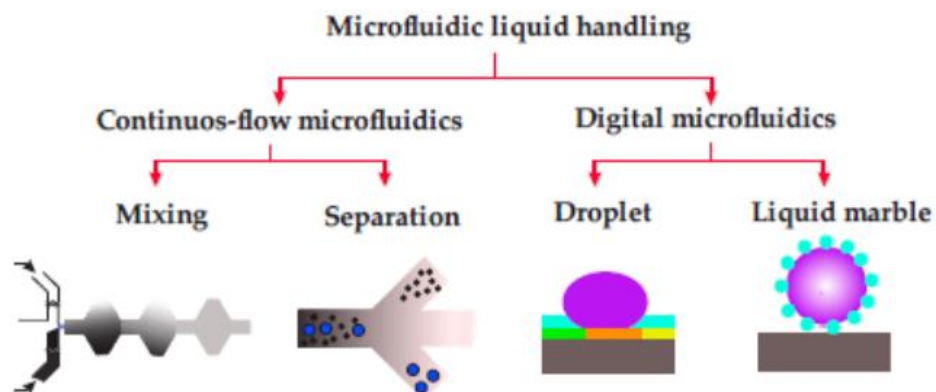


Figure 2 The field of microfluidic liquid handling.

### 2.2.1 Droplet microfluidics

Droplet microfluidics is a technology for synthesizing a uniform stream of droplets or bubbles. Droplet formation is the result of an emulsion created using two immiscible fluids which can be liquid/liquid or gas/liquid systems. The droplet phase is identified as a dispersed phase while a continuous phase is a medium phase. The small volume of fluid leads to low Reynolds number flow, in which fluid flow is laminar and controllable. Microfluidic systems can fabricate droplets with uniform particle size, narrow size distribution, desirable properties, and tunable features such as droplet size, structure, and surface. Moreover, they enable continuous online synthesis which can reduce the batch-to-batch variations.

### 2.2.2 Droplet-microfluidic geometry

The geometry of the microfluidic channel plays an important role in droplet generation. Three types of common geometry are co-flow, cross-flow, and flow-focusing devices as shown in Figure 3. Co-flow geometry demonstrates the parallel streams of the dispersed and continuous phase fluids. The uniformity of droplet size in co-flow geometry depends on the flow regime which reveals high monodisperse with the coefficient of variation or  $CV < 3\%$  in the dripping regime [3] and polydisperse in jetting regime [4]. The cross-flow geometry refers to the channel in which two immiscible fluids

meet at an angle from  $0^\circ$  to  $180^\circ$ . Due to its simplicity, this geometry is widely used [5, 6]. The monodisperse with  $CV < 2\%$  water in oil droplets was generated in a simple T-junction which has an angle of  $90^\circ$  [7]. In addition, another angle was studied for droplet producing, for instance, Y-junction [8], K-junction [9, 10], and V junction [11, 12]. Flow-focusing geometry focuses on the elongating flow after passing through a junction which can generate smaller droplets. Two categories of flow-focusing configuration are sorted, one is 3D axisymmetric, and another is quasi-2D planar. In comparison, 3D axisymmetric can produce monodisperse droplet ( $CV < 5\%$ ) with higher throughputs [13]. Both co-flow and flow-focusing geometries produce droplets with smaller dimensions than the dispersed phase channel, with flow-focusing geometry generating a narrower stream than co-flow. The droplet size is smaller than the orifice diameter to reduce the chance of clogging [14].

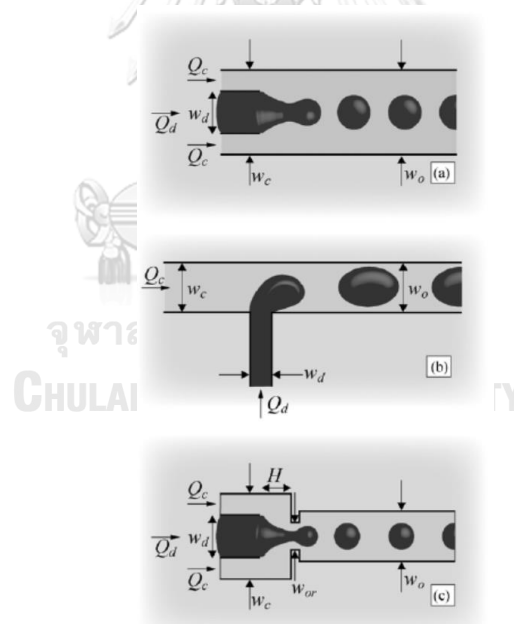


**Figure 3** The three main droplet-microfluidic geometries used.

(a) Co-flow (b) Cross-flow (in T-junction) (c) Flow focusing [15].

### 2.2.3 Droplet generation

Passive droplet generation which occurs by two immiscible fluids is controlled by providing a fluid flow rate leading to the formation of droplets in one of five regimes:

squeezing, dripping, jetting, tip streaming, and tip-multi-breaking (Figure 4) [16]. The squeezing regime initiates at a low continuous phase ( $Ca_c < 10^{-2}$  in T-junction [17-19]). Due to the formation being confined by channel geometry, squeezing is often called a 'geometry-controlled' regime. When the continuous phase capillary number ( $Ca_c$ ) increased, the regime transforms from squeezing to dripping. The breakup of immiscible fluid occurs at the nozzle, orifice, or junction in the dripping regime [19]. A smaller size than the channel dimension is obtained due to the dispersed phase break up before the growing droplet hampers a channel. The jetting regime appears to increase either continuous flow rate or dispersed flow rate [4]. Droplets are generated in the tip streaming regime when the dispersed phase is forced into steady a conical shape or cone-jet structure and onwards break into small droplets. The droplet size in this regime can be small as submicrometer-scale and monodisperse. However, tip-multi-breaking will be displayed since the dispersed cone structure is unsteady.

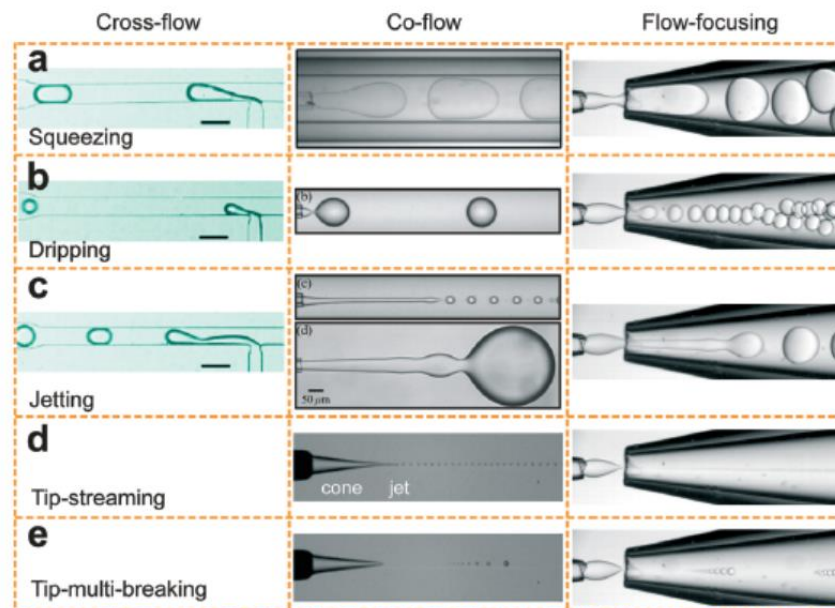


**Figure 4** The droplet generation with different regime in cross-flow, co-flow and flow-focusing geometries. (a) Squeezing regime (b) Dripping regime (c) Jetting regime (d) Tip streaming regime (e) Tip-multi-breaking regime [16].

#### 2.2.4 Dimensionless number

Droplet formation in microfluidics utilizes two immiscible fluid which is dispersed and continuous phase flow. The physical parameters which are the common fluid properties are the viscosities,  $\mu_d$  and  $\mu_c$ , the densities,  $\rho_d$  and  $\rho_c$ , and the interfacial tension,  $\sigma$ . The subscripts 'd' and 'c' refer to dispersed and continuous phase fluid, respectively. The fluid flow rate,  $Q_d$ , and  $Q_c$ , which are driven by pressure input,  $P_d$  and  $P_c$ , are classed as the operating parameter. Four key forces reveal the droplet generation: inertial force, viscous force, gravity, and capillary force. Thus, several dimensionless numbers are developed to study. Dimensionless parameters in droplet microfluidics are shown in Table 2.



Table 2 Dimensionless parameters in droplet microfluidics

Symbol	Dimensionless	Formula	Physical meaning
Re	Reynold number	$Re = \frac{\rho v D}{\mu}$	$\frac{\text{Inertial force}}{\text{Viscous force}}$
Ca	Capillary number	$Ca = \frac{\mu v}{\sigma}$	$\frac{\text{Viscous force}}{\text{Interfacial force}}$
We	Weber number	$We = \frac{\rho v^2 L}{\sigma}$	$\frac{\text{Inertial force}}{\text{Interfacial force}}$
Bo	Bond number	$Bo = \frac{\Delta \rho g L^2}{\sigma}$	$\frac{\text{Buoyancy}}{\text{Interfacial force}}$
$\lambda$	Viscosity ratio	$\lambda = \frac{\mu_d}{\mu_c} \text{ or } \frac{\mu_c}{\mu_d}$	$\frac{\text{Dispersed viscosity}}{\text{Continuous viscosity}}$ or $\frac{\text{Continuous viscosity}}{\text{Dispersed viscosity}}$
$\varphi, Q$	Flow rate ratio	$\varphi, Q = \frac{Q_c}{Q_d} \text{ or } \frac{Q_d}{Q_c}$	$\frac{\text{Continuous flow}}{\text{Dispersed flow}}$ or $\frac{\text{Dispersed flow}}{\text{Continuous flow}}$



### 2.2.5 Parameters of droplet formation

Physical parameters such as viscosity and interfacial tension influence droplet generation. The microdroplet size is inversely proportional to the viscosity of the dispersed (Figure 5). I. Kobayashi et al. [20] confirmed that viscosity affected droplet size, not the chemical nature of the fluid used. In terms of interfacial tension, large energy is needed with large tension. The small droplet was found when the interfacial tension of the dispersed phase was low [21].

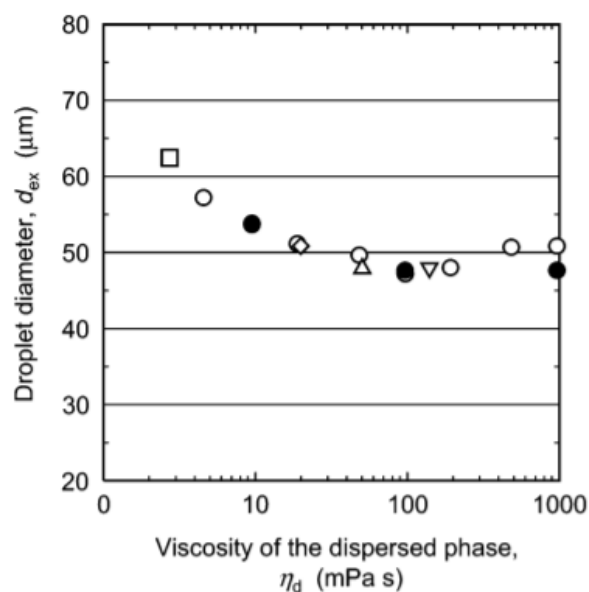


Figure 5 The effect of dispersed-phase viscosity from various type of fluid with droplet size [20].

The fundamental operating parameter in droplet microfluidics is the flow rate of two immiscible fluid which is dispersed and continuous phase. K.S. Huang et. al. [22] studied the relationship between flow rate and droplet size in a T-junction microchannel. For keeping a continuous phase (oil flow) constant, the droplet size increased with the dispersed phase (water flow) as shown in Figure 6. In the case of fixing the dispersed phase, the droplet size was decreased with the continuous phase. The same tendency was observed in other studied [23-26].

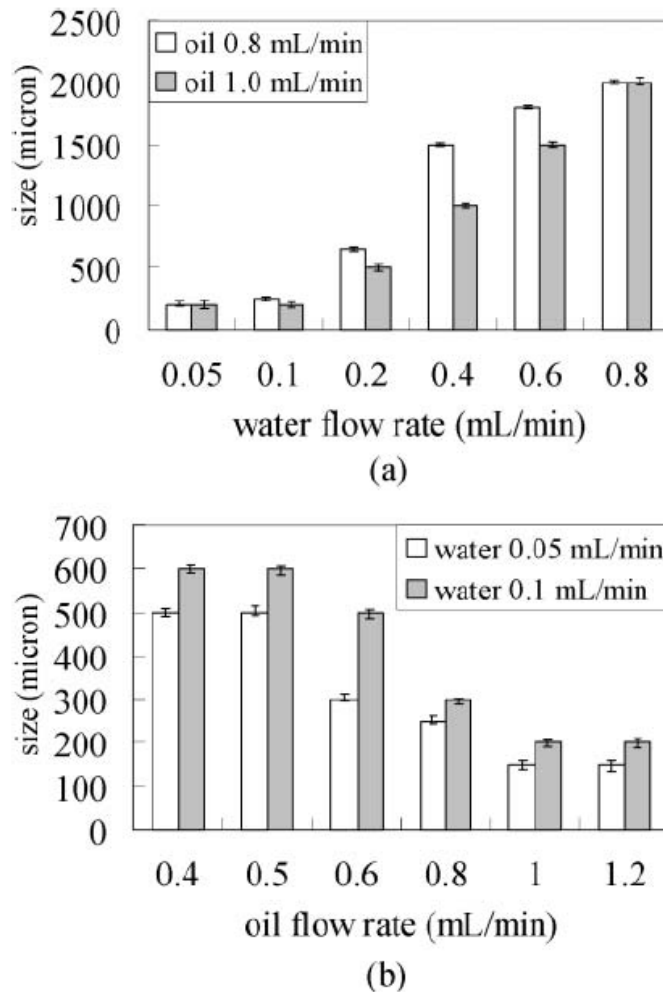


Figure 6 Relationship between droplet size and flow rates:

(a) fixed dispersed phase (water) flow rate (b) fixed continuous phase (oil) flow rate [22].

The ratio of flow rate ratio,  $Q$ , as dimensionless number is defined.

$$Q = \frac{Q_c}{Q_d} \text{ or } \frac{Q_d}{Q_c}$$

where  $Q_d$  and  $Q_c$  is the fluid flow rate of dispersed and continuous phase flow rate, respectively. The small droplet size was obtained with the larger  $Q = \frac{Q_c}{Q_d}$  [27]. Moreover, the influence of flow rate ratio on flow regime was studied by H. Liu et al. [28]. They defined the flow rate ratio as  $Q = \frac{Q_d}{Q_c}$  which showed three flow patterns: droplet

generation at cross-junction (DCJ), downstream (DC), and parallel flow (PF). At low  $Q$ , droplet formation was in the squeezing regime. When  $Q$  was increased, droplets are formed downstream and eventually reached to parallel stream as presented in Figure 7.

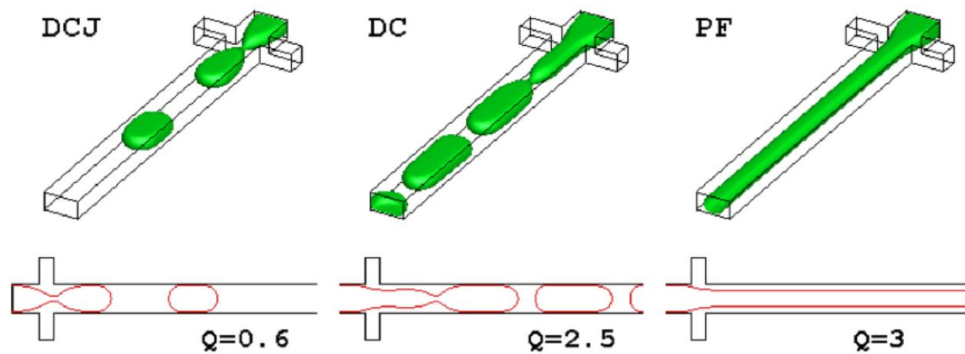


Figure 7 Droplet flow pattern as a function of flow rate ratio ,  $Q = \frac{Q_d}{Q_c}$  [28].

Capillary number,  $Ca$ , also plays an important role in droplet size and flow regime. The droplet size decreased with an increased capillary number of the continuous phase (see Figure 8). The transition from squeezing to dripping regimes identify at the critical capillary point,  $Ca_c$ , at all  $Q$ . However, at a low viscosity ratio,  $Ca_c$  was not found in the squeezing-to-dripping transition [29] due to the droplet formation downstream.

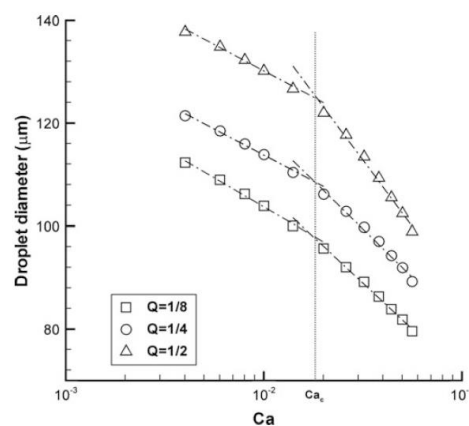


Figure 8 The effect capillary number of continuous phase at different flow rate ratio [30].

### 2.2.6 Model of droplet formation

P. Garstecki et al. [18] first proposed a simple scale law (Eq.(1)) for droplet size in T-junction microfluidics. The size of droplets or bubbled singly depended on the flow ratio. They showed the agreeable results of their experimental data and the model in Figure 9.

$$\frac{L}{w_c} = 1 + \alpha Q \quad (1) [18]$$

where  $L$  is the length of the immiscible slug,  $w_c$  is the width of the channel,  $Q$  is the flow ratio between dispersed and continuous phase, and  $\alpha$  is a constant value that rely on the geometry of the T-junction.

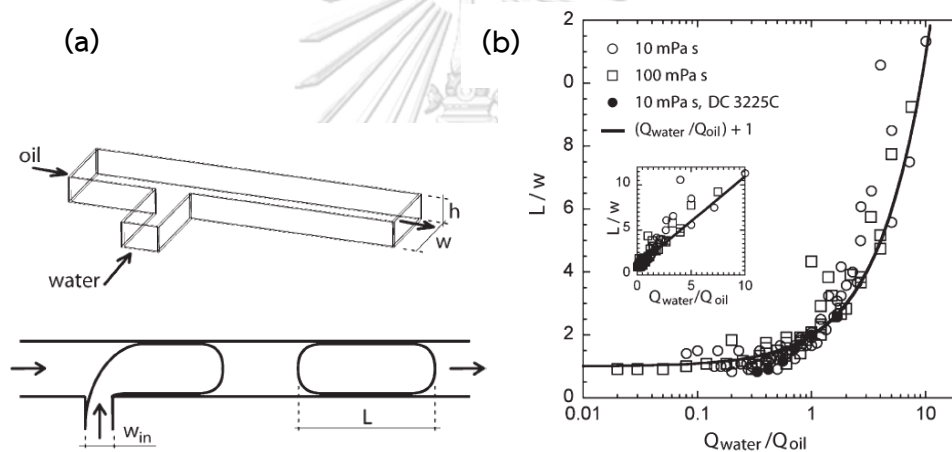


Figure 9 (a) a schematic illustration of the T junction microfluidics (b) an agreeable experimental and model derived results of P. Garstecki et al.'s study[18].

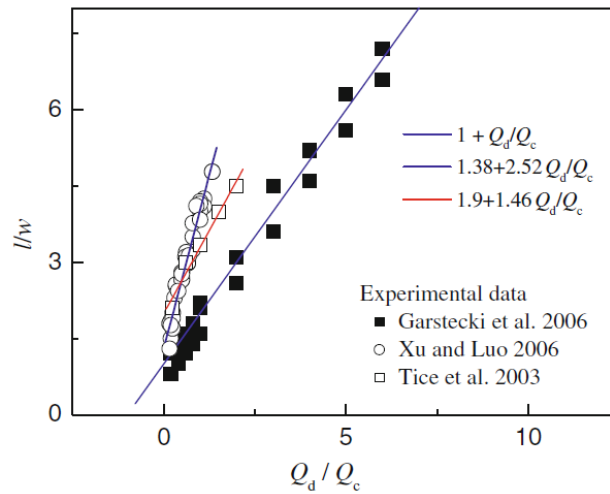


Figure 10 A fitting experimental and model results of J. H. Xu et al.'s study [31].

J. H. Xu et al. [31] compared the experimental results in T-junction microfluidics with P. Garstecki et al. [18], J. H. Xu et al. [7, 32, 33] and J. D. Tice et al. [34]. They suggested that there was a parameter relevant to the growth length which made the equation as

$$\frac{L}{w_c} = \varepsilon + \omega Q \quad (2) [31]$$

where  $\varepsilon$  and  $\omega$  are fitting parameters which mainly affected by the different geometry. However, the capillary number was conducted in the pattern flow. The models of droplet size as a function of the capillary number in T-junction microfluidics were numerous studied as shown in Table 3.

**Table 3** The models for a droplet size in T-junction microfluidics

Capillary number	Model	Author
$10^{-4} < Ca < 0.002$	$\frac{L}{w} = 1 + Q$	P. Garstecki et al. [18]
	$\frac{L}{w} = 1.38 + 2.52Q$	J. H. Xu et al. [35]
	$\frac{L}{w} = 1.9 + 1.45Q$	J. D. Tice et al. [34]
$0.002 < Ca < 0.01$	$\frac{L}{w} = 0.75Q^{1/3} \cdot \left(\frac{1}{Ca}\right)^{1/5}$	J. H. Xu et al. [35]
$0.01 < Ca < 0.2$	$\frac{L}{w} = \left(\frac{1}{Ca}\right) \cdot \left(\frac{w \cdot h - 0.785d^2}{w} \cdot h\right)$	J. H. Xu et al. [31]
	$\frac{L}{w} = 1.42Ca^{-0.11}$	T. Fu et al. [36]
$Ca > 0.2$	$\frac{L}{w} = \sigma / \mu_c V_c$	T. Thorsen et al. [5]

In flow-focusing microfluidics, model in Eq.(3) and mechanism of droplet formation was originally studied by J. Tan et al. [37].

$$\frac{L}{w_c} = k \left(\frac{Q_c}{Q_d}\right)^\alpha Ca^\beta \quad (3) [37]$$

where  $k$ ,  $\alpha$  and  $\beta$  are constant values which were 1.59, -0.20, and -0.20, respectively, in a cross-junction microfluidic device with a 100mm × 20mm × 5mm configuration.

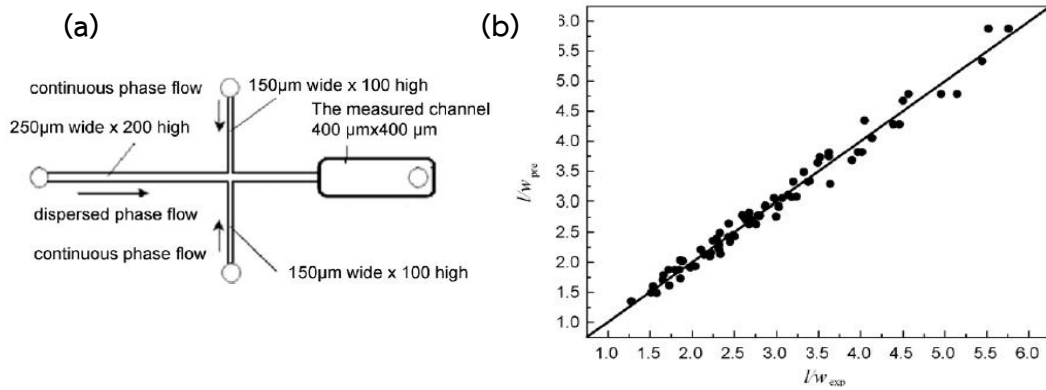


Figure 11 (a) a schematic illustration of the cross-junction microfluidics (b) an agreeable experimental and model derived results of J. Tan et al.'s study [37].

Howsoever, H. Liu et al. [28] numerical simulated the droplet breakup in cross-junction which indicated influential capillary number on scaling law shown in Eq.(4).

$$\frac{L}{w_c} = (\varepsilon + \omega Q) Ca^m \quad (4) [28]$$

where  $\varepsilon$ ,  $\omega$ , and  $m$  are the fitting parameters mainly depending on the channel geometry. The various geometrical channel in Figure 12(a) resulted in  $\varepsilon=0.551$ ,  $\omega=0.277$ , and  $m=-0.292$ . While tailor-made microfluidics (Figure 13(a)) by F. Lapierre et al. showed the results of  $\varepsilon=0.2$ ,  $\omega=0.68$ , and  $m=-0.2$  [38].

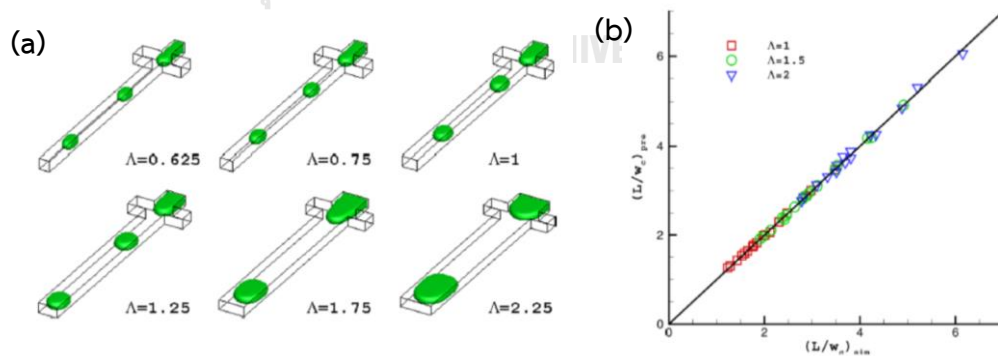


Figure 12 (a) a schematic illustration of the cross-junction microfluidics (b) an agreeable predicted results and simulated results of H. Liu et al.'s study [28].

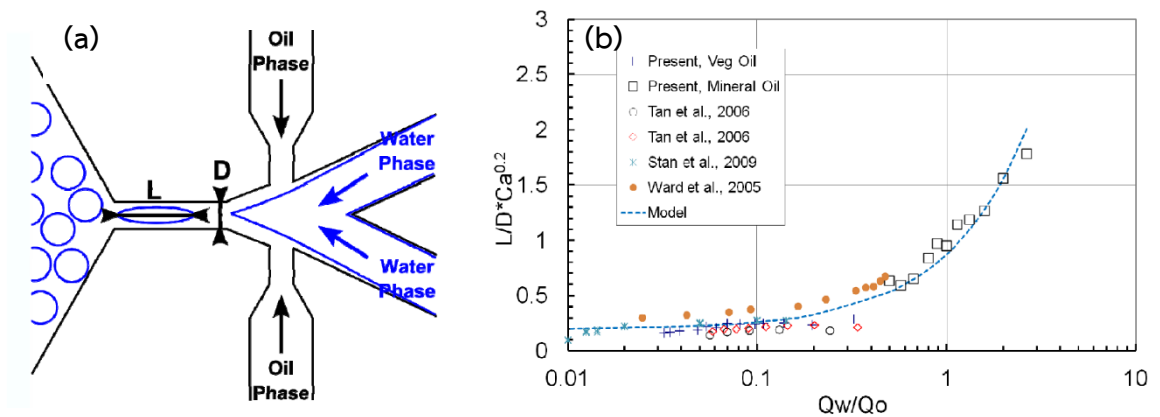


Figure 13 (a) a schematic illustration of the microfluidics (b) an agreeable experimental and model derived results of F. Lapierre et al.'s study [38].

### 2.3 Biopolymer

Biopolymers are polymeric biomolecules produced by living organisms. There are two main types of biopolymers used to fabricate particles in terms of the encapsulation process: protein and polysaccharides. The selection of biopolymer depends on a functional requirement for the final particle such as a target of active ingredient release. Molecular, physicochemical, and electrostatic characteristics affect the optical, rheological, and stability of particles. The chemical and molecular differences such as structure, the degree of branching, molecular weight, and electrical charge also have an effect on the functional properties of polysaccharide-biopolymers such as solubility, thickening, and gelling mechanism, water holding capacity, digestibility, and surface activity [39].

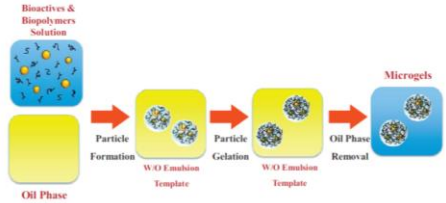
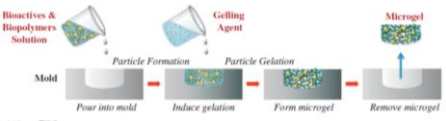
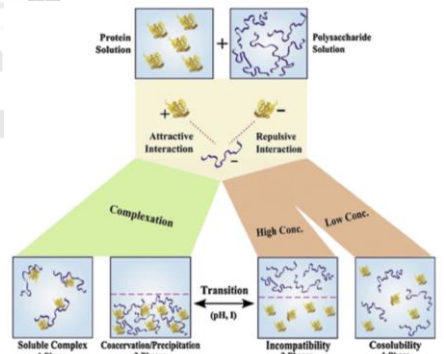
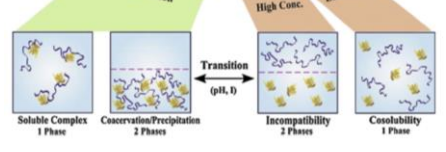
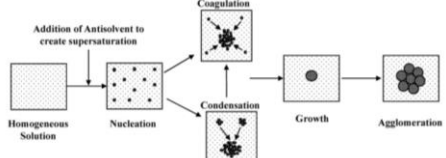
The biopolymer-based microparticle fabrication usually has two steps: particle formation and particle gelation. In the first step, the hydrophilic actives are usually directly dissolved with biopolymer in the aqueous phase, whereas lipid droplets or vehicles are produced before in the case of hydrophobic actives. In the second step, the mixture of biopolymers and active agents is formed by environmental conditions to cross-link the biopolymer chain. The common forming method is brief in Table 4.



Table 4 The common method of biopolymer-based particle forming [39-41]

Method		Schematic
Injection	<p><b>Simple extrusion</b></p> <ul style="list-style-type: none"> <li>- The mixture was injected into the gas phase and then formed by temperature changing or by the gelling solution. The particles have a spherical shape due to the relative surface tension between solution-air is high.</li> </ul>	
	<p><b>Atomization</b></p> <ul style="list-style-type: none"> <li>- The dehydrated particles are produced by spray drying or spray chilling. The biopolymers are cross-linked when reconstituted in water.</li> </ul>	
	<p><b>Microfluidics</b></p> <ul style="list-style-type: none"> <li>- The biopolymers and active ingredients are injected into a channel to form particles, and then cross-link in the environmental condition.</li> </ul>	
	<p><b>High-pressure microfluidization</b></p> <ul style="list-style-type: none"> <li>- The battle of a mixture stream into a cross-link agent stream at high velocity produces particles.</li> </ul>	

Table 4 The common method of biopolymer-based particle forming (Cont.)

Method	Schematic
<p><b>Templating</b></p> <p><b>Emulsion-based</b></p> <ul style="list-style-type: none"> <li>- The mixture is emulsified a water-in-oil emulsion by a homogenizer.</li> <li>The cross-linking is formed inside the water droplet by changing the system in proper conditions.</li> </ul>	
<p><b>Lithographic</b></p> <ul style="list-style-type: none"> <li>- The mixture is filled into a mold, and then cross-linked in the alter environmental condition.</li> </ul>	
<p><b>Phase separation</b></p> <p><b>Electrostatic complexation</b></p> <ul style="list-style-type: none"> <li>- The particle formation occurs from electrostatic attraction between two oppositely charged biopolymers.</li> </ul>	
<p><b>Thermodynamic incompatibility</b></p> <ul style="list-style-type: none"> <li>- The particle formation occurs from repulsion interaction between biopolymers.</li> </ul>	
<p><b>Antisolvent precipitation</b></p> <p>The particles are formed based on the solubility in different solvent.</p>	

## 2.4 Alginate

Alginate is a hydrophilic biopolymer derived from brown seaweeds. Alginate is an anionic polysaccharide consisting of a linear copolymer of (1–4)-linked  $\beta$ -D-mannuronic (M) and  $\alpha$ -L-guluronic acid (G) residues. Due to its great properties such as biodegradable, biocompatible, low cost, and non-toxic, alginate is widely used in many applications. Alginate has been used for encapsulating numerous active ingredients both hydrophilic and hydrophobic substances. The classification of alginate particles is shown in Figure 15. The alginate particles with a dispersing of active compounds in the polymer matrix are defined as 'beads'. 'Capsules' are the particles comprised of the polymer which holds a liquid core containing the active ingredient. The 'microparticles' refer to beads with smaller particle sizes. Multiple layers of polymers are classified as 'multi-membrane'.

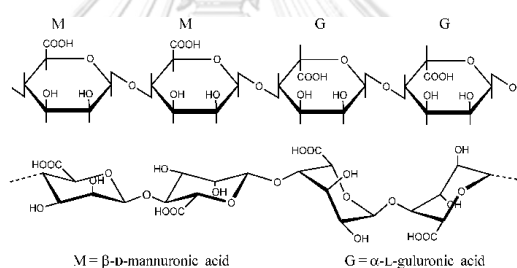


Figure 14 Structure of alginate.

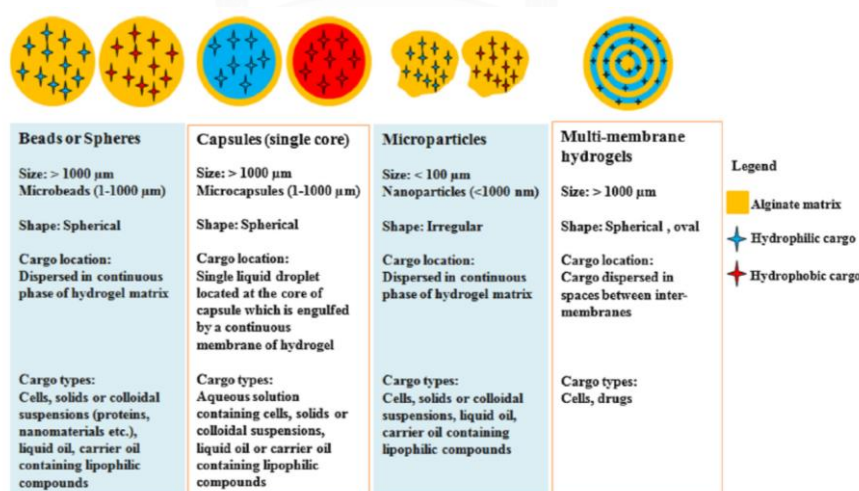


Figure 15 Design of alginate particle.

### 2.4.1 Alginate-particle formation

The particle formation of alginate is assorted to three main methods (see Figure 16). The liquid-air methods which generated droplets using a nozzle system are generally used. The particles have a spherical shape due to the relative surface tension between solution-air is high. The dripping, jetting, and atomization method depends on the volumetric flow rate of the alginate solution extruded from the nozzle. In terms of the liquid-liquid method, the droplets are formed by two immiscible fluids which could be water-in-oil emulsions prior to gelling. Alginate particles are also produced without high energy input in the self-assembly method [42].

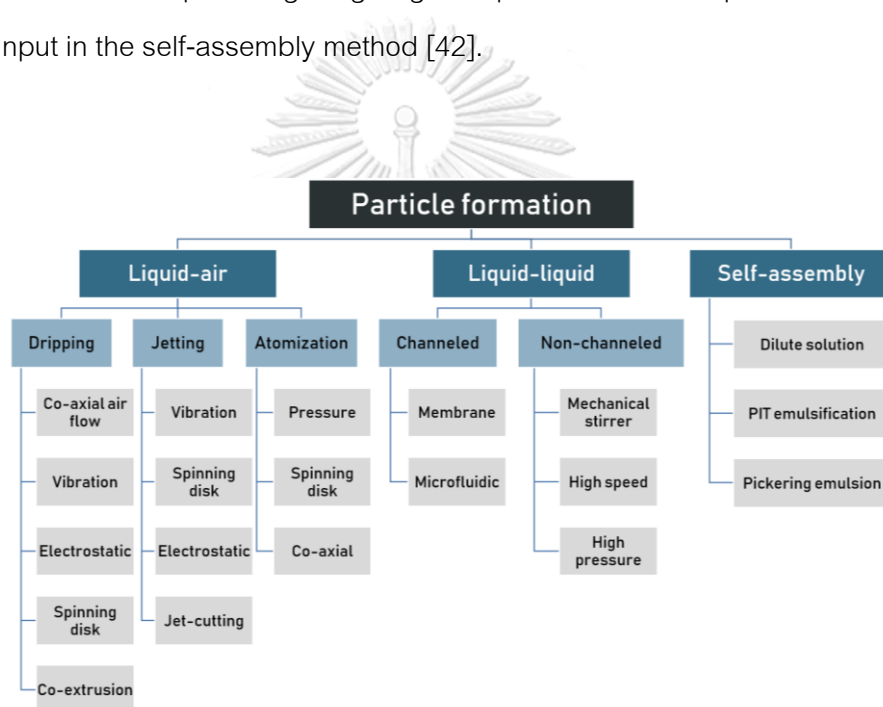
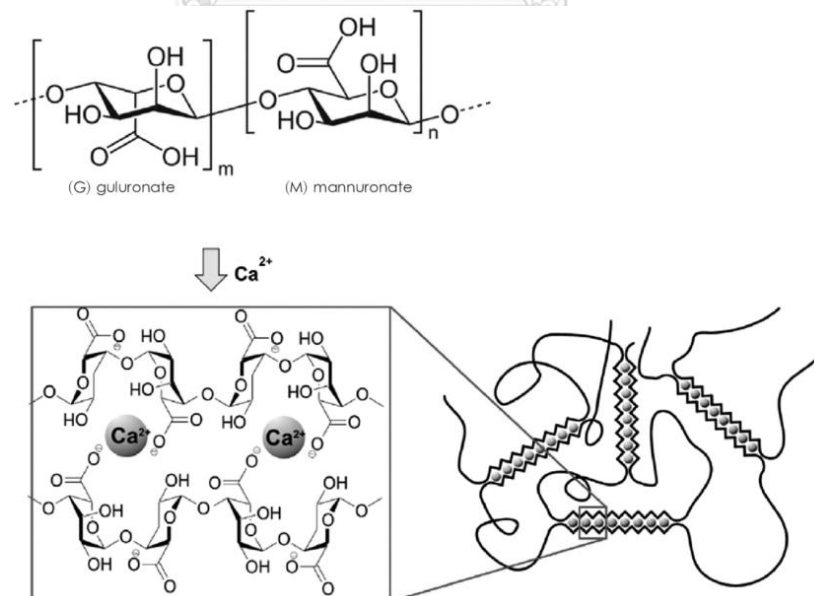


Figure 16 Method of alginate-particle formation.

### 2.4.2 Alginate-particle gelation

The alginate polymer chain is simply cross-linked with divalent cations. The cross-linking process occurs by the incorporation of divalent cations into the structure of guluronate blocks, forming an 'egg-box' structure (Figure 17). Calcium ( $\text{Ca}^{2+}$ ) is the most generally used cation for ionotropic gelation thanks to its non-toxic property. A variety of calcium salt can be used in alginate gelation. Calcium chloride ( $\text{CaCl}_2$ ) is a readily soluble calcium salt which commonly used whereas insoluble calcium salt like calcium carbonate ( $\text{CaCO}_3$ ) can also be used when need to slow or control the cross-linking [42]. Gelatin mechanisms: external, internal, inverse, and interfacial gelation are shown in Figure 18-21. In the external gelation, the  $\text{Ca}^{2+}$  ions are introduced externally into the discrete alginate droplets. The alginate solution is normally dropped into a gelling bath. However, the cross-linking which occurred inside the alginate droplet is internal gelation. The released  $\text{Ca}^{2+}$  ions are internally cross-linked with the alginate polymer chains. In contrast to external gelation, the solution containing  $\text{Ca}^{2+}$  ions are dropped into an alginate bath in inverse gelation. In the case of interfacial gelation, cross-linking starts assembling at the interface of the droplet.



**Figure 17** Gelling mechanism of calcium crosslinked alginate (egg-box like conformation).

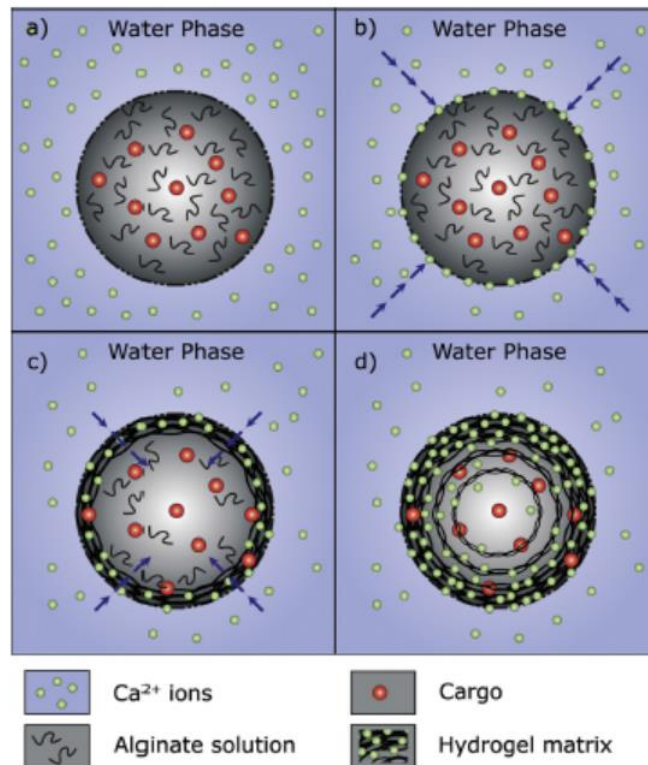


Figure 18 Mechanism of external gelation for bead formation :

(a) alginate droplet in contact with calcium solution, (b) inward diffusion of calcium ions, (c) inward gelation of droplet, and (d) completed gelation [42].

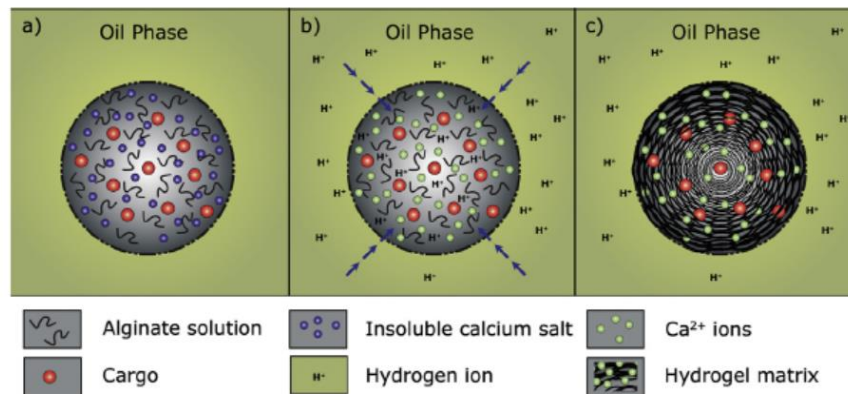


Figure 19 Mechanism of internal gelation for bead formation :

(a) dispersion of alginate droplet in oil, (b) addition of acid to dissolve the calcium salt, and (c) localized gelation of droplet [42].



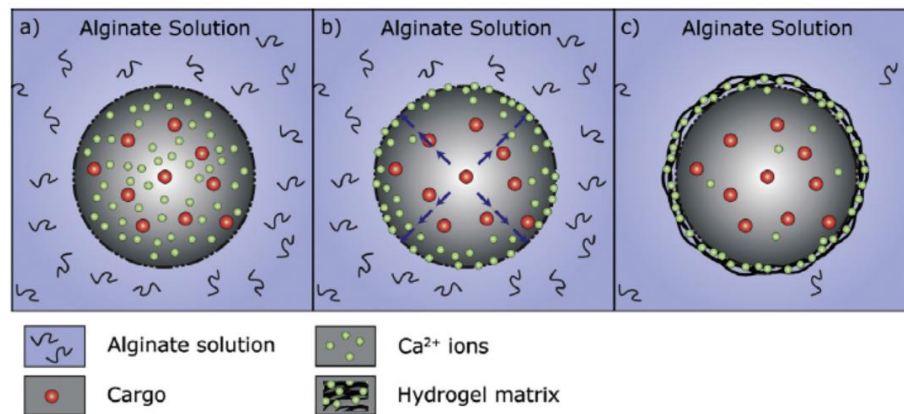


Figure 20 Mechanism of inverse gelation for liquid-core capsule formation :

- (a) droplet containing calcium ions in contact with alginate solution,  
 (b) outward diffusion of calcium ions, and (c) gelation at droplet interface [42].

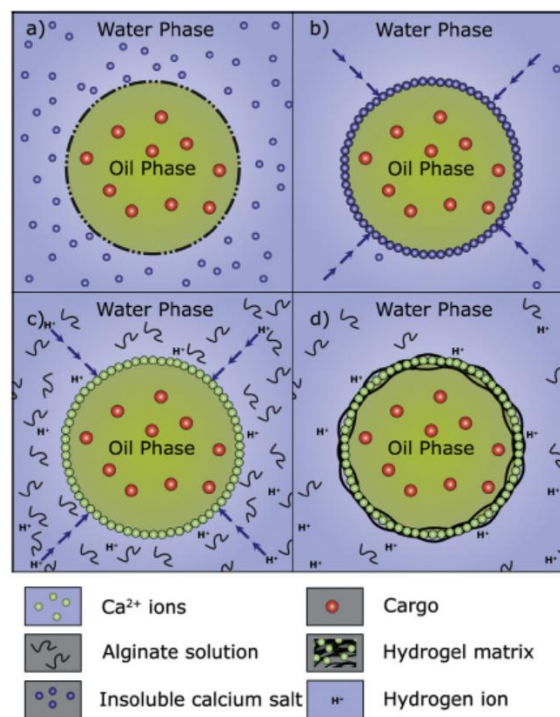


Figure 21 Mechanism of interfacial gelation for oil-core capsule formation :

- (a) oil droplet emulsified in a dispersion of  $\text{CaCO}_3$ , (b) self-assembly of  $\text{CaCO}_3$   
 at the interface, (c) addition of the alginate solution followed by acid to dissolve  $\text{CaCO}_3$ ,  
 and (d) gelation at the droplet interface [42].

## 2.5 Droplet microfluidic in encapsulation technology

Over the past three decades, a few microfluidic approaches have been developed and widely applied for encapsulation technology. It is an alternative technique to prepare emulsions and microparticles. The reason of interesting is its ability to produce monodisperse droplets with narrow size distribution and the controllable system to precise the size of the droplet. Particle size and size distribution play an important role in controlling drug release. Monodisperse particles show a slower drug release than polydisperse particles with a similar average size. The preparation procedure of particles for encapsulation is based on the combination of droplet microfluidic and droplet-to-particle technology. The single droplets, double emulsions, and multiple emulsions are first generated in the microfluidic device, in which the droplet phase consists of a polymer, natural polymer, or inorganic substance along with the payload ingredient. The liquid droplet phase can be solidified by different methods such as evaporation, polymerization, and reaction. Then, the microparticles are formed with encapsulation of any active compound [43, 44].

The O/W emulsion is usually used as a template for microparticles which composes of hydrophobic materials. Many active compounds especially drugs are encapsulated into a polymeric particle-matrix such as poly(lactic-co-glycolic acid) (PLGA), polylactide (PLA), poly- $\epsilon$ -caprolactone, and hydroxypropyl methylcellulose acetate succinate (HPMCAS) [24, 45, 46]. These polymeric particles are typically dissolved in a volatile solvent which can evaporate after the emulsion is formed. The final microparticle size is controlled by the emulsion size and how much the droplet shrinks during solvent removal. Compared with the conventional method, the model drug, bupivacaine, in PLGA microparticles prepared from the microfluidic technique showed a slower release profile [46]. Moreover, the model drug, sorafenib(SFN) and celecoxib, which were encapsulated into the hollow acetylated dextran (AcDX) and HPMCAS microparticles using a microfluidic technique also showed a slower release



rate of payloads [24]. In addition, two lipophilic active molecules,  $\beta$ -carotene and  $\gamma$ -oryzanol were generated as O/W emulsions in microfluidic with uniform droplet size and low coefficient variation and had good stability for 4 months [47].

The W/O emulsion is also used as a template for encapsulating the hydrophilic materials which are efficient for encapsulating bioactive water-soluble agents such as peptides, proteins, antibodies, and living cells. The hydrophilic polymers such as alginate [48], chitosan [49], and poly(N-isopropylacrylamide) [50] were used. The model drug, iopamidol, was studied in different morphology of sodium alginate microgel. Monodisperse microparticles with narrow size distribution have been prepared based on a W/O emulsion template in different microfluidic devices, including T-junction [51, 52] and cross junction [53]. Moreover, chitosan microparticles were also fabricated based on a W/O emulsion template [54-56]. The properties of chitosan microparticles can be controlled by encapsulating different substances into the initial chitosan solution.

Double emulsions are an interesting template when the payloads are present in different solubility. The W/O/W double emulsion template was used for the drug model, doxorubicin (DOZ), and paclitaxel (PTX) which were loaded as the inner aqueous core in the lipid shell by using the microfluidic technique [57]. The uniform microcapsules can be prepared in microfluidic devices based on a double emulsion template through different kinds of solidification methods. Oil core poly(L-Lactic acid) (PLLA) microcapsules were successfully prepared in the microfluidic technique using evaporation [58]. PLA microcapsules with a shell thickness of a few nanometers were generated based on a W/O/W double emulsion template and evaporation-induced solidification [59]. Moreover, polymersomes such as poly(ethylene-glycol)-b-poly(lactic acid) (PEG-b-PLA) and also liposomes could be prepared in a microfluidic device using a W/O/W double emulsion template [60]. For encapsulation of hydrophobic substance, oil core in alginate [61], chitosan [62], and gelatin [63] microcapsules were fabricated

based on the O/W/O double emulsions template. The hollow microgel could be also produced by a microfluidic technique using the O/W/O emulsion template [64].

With the advantage of microfluidics, a wide variety of encapsulated particles with controlled size, structure, and composition have been fabricated, including single emulsion, double emulsion, microparticles, and microcapsules. The scalability, low cost, and reproducibility of microfluidic strategies make them an excellent process for encapsulation technology.



## Chapter 3

### Experiment

#### 3.1 Chemical and reagents

Sodium alginate (Sigma-Aldrich, USA) was dissolved in distilled water at concentrations of 1, 2, and 3% (w/w). The oil phase was jojoba oil and Miglyol<sup>®</sup>812 oil (Sasol Germany GmbH, Germany). Span<sup>®</sup>80 was purchased from Croda International (United Kingdom). Ca-EDTA and Coumarin 6 were purchased from Sigma-Aldrich, USA. Medium-chain triglyceride (MCT) oil was obtained from Wilmar International, Singapore. Calcium chloride dihydrate and Rhodamine 6G were provided by Merck, Germany. Acetic acid was obtained from Carlo Erba, Italy. Alpha-mangostin was purchased from Hansea chemical biotech, China. Water used for all experiments was obtained from a MilliQ Plus system (Millipore, Schwalbach, Germany).

#### 3.2 Experimental procedures

Experimental works would be separated into 3 sections.

##### 3.2.1 Hydrodynamic control of droplet formation in narrowing jet and tip streaming regime using microfluidic flow-focusing

In this section, the experimental setup was composed of two streams as the continuous phase and the dispersed phase (Figure 22). The fluids were pumped through a Teflon tube to the flow-focusing geometry of the Droplet Junction Chip. Two-size junctions with 100 and 190  $\mu\text{m}$  etch depth, junction size (j) of 105 and 195  $\mu\text{m}$ , and channel size (c) of 300 and 390  $\mu\text{m}$  were used. Various concentrations of sodium alginate solution (1, 2, and 3% (w/w)) were used as the dispersed phase, whereas jojoba oil or Miglyol<sup>®</sup>812 oil was used as the continuous phase. The surfactant Span<sup>®</sup>80 was added for stabilization. The flow rate of the dispersed and continuous phases varied from 10 to 250  $\mu\text{l}/\text{min}$  and 1 to 140  $\mu\text{l}/\text{min}$  respectively. The fluid flow was allowed to reach a steady regime and the process was captured by a high-speed camera (Dolomite, UK). A stereo microscope (model SMZ745T, Nikon, Japan) connected with microscopy software (Pixelink Capture Program, USA) was set above the microfluidic chip to observe fluid characteristics inside the channel. Droplets were collected and

immediately observed by an optical microscope (model IX71, Olympus, Japan). Emulsion droplet size was measured, with the average value obtained from at least 100 droplets at different positions using ImageJ software (National Institute of Mental Health, USA).

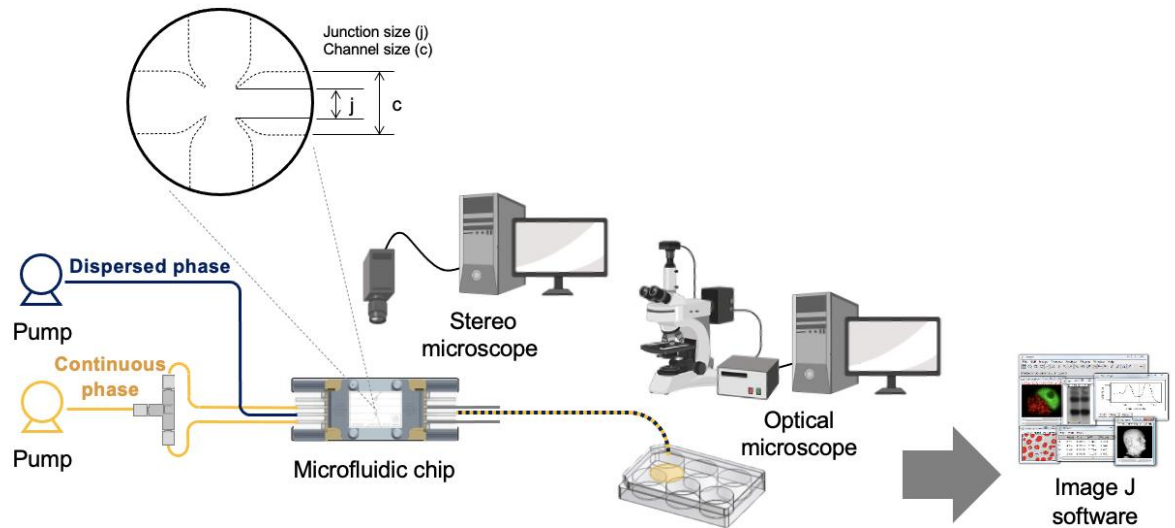


Figure 22 Schematic of droplet formation of experiment.

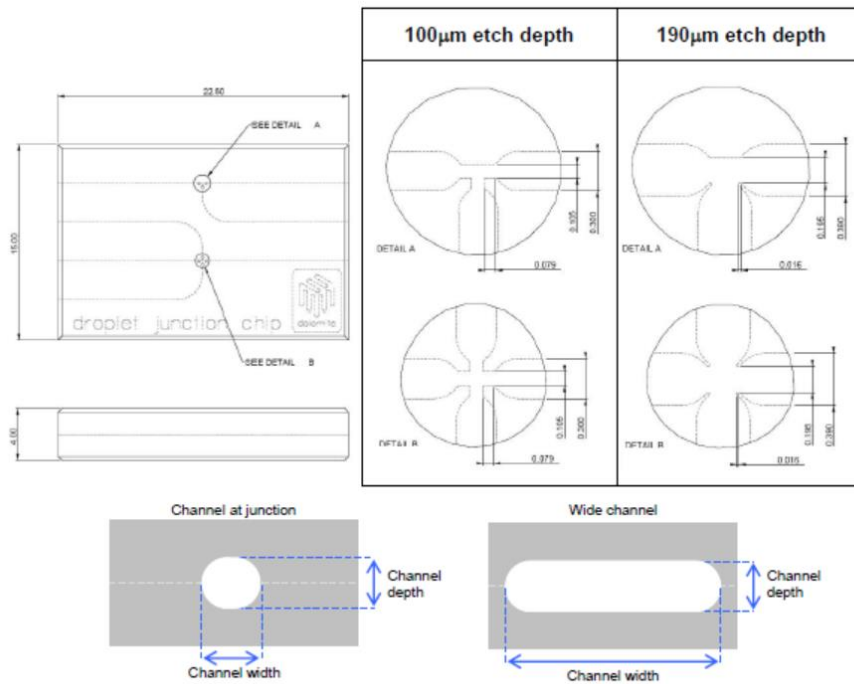


Figure 23 Geometry of droplet microfluidic channel.

### 3.2.2 Internal gelation of alginate microparticle prepared by emulsification and microfluidic method: Effect of Ca-EDTA as a calcium source

Alginate microparticles were prepared by emulsification/internal gelation and microfluidic/internal gelation technique. Calcium-ethylenediaminetetraacetic acid (Ca-EDTA) was used as a calcium source, which could release  $\text{Ca}^{2+}$  ions to crosslink with the alginate chain by adding acid. The schematic of the experiment setup of the emulsification method is shown in Figure 24. Water in oil emulsion of Ca-EDTA mixed with sodium alginate solution in oil phase was prepared. The emulsification and gelation steps were performed using a magnetic stirrer (RCT basic, digital, IKA, Germany) and a high-speed homogenizer (T25 digital, IKA, Germany). Various concentration Ca-EDTA (0.1, 0.2, 0.3 and 0.5 M) was dissolved in 2%(w/w) sodium alginate. The sodium alginate with Ca-EDTA solution was mixed with MCT oil, which was used as a medium phase to emulsify at 400 rpm of the magnetic stirrer, followed by 5,000, 7,500, and 10,000 rpm of the high-speed homogenizer. The acetic acid was added to form the alginate particles while stirring at 400 rpm. The crosslinking was investigated at 1, 3, 5, and 10min. After stirring, the samples of alginate particles were washed and collected with water until no oil was left by centrifugation at 2,500 g, 25°C for 10 min and then redispersed with water for further analysis.

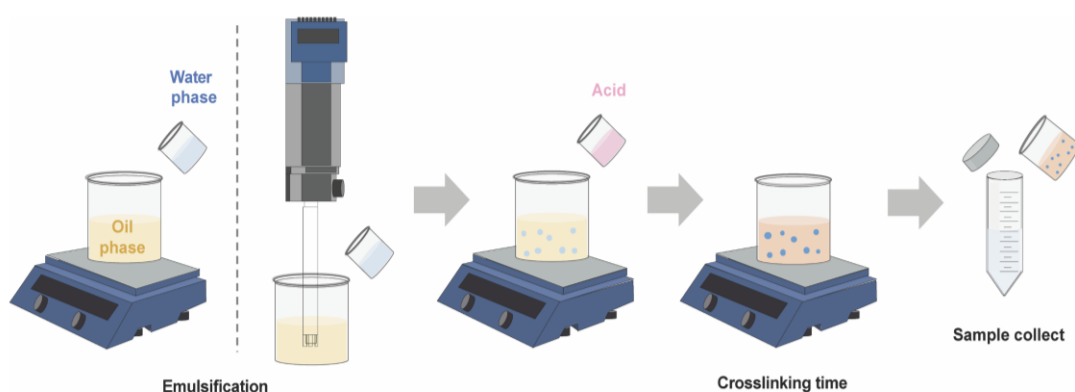


Figure 24 Schematic of emulsification method for alginate microparticle.

Figure 25 shows the experimental setup of the microfluidic technique was composed of two streams of the continuous phase and dispersed phase. The fluids were pumped through the 100  $\mu\text{m}$  etch depth flow-focusing geometry of the Droplet Junction Chip. The 2%(w/w) sodium alginate solution with Ca-EDTA was used as the dispersed phase, whereas MCT oil with 1%(v/v) acetic acid was used as the continuous phase. A stereo microscope connected with microscopy software was set above the microfluidic chip to observe the fluid characteristics inside a channel. Droplets were collected with MCT oil while stirring. After droplet collection, the samples were washed with water as well as the emulsification method.

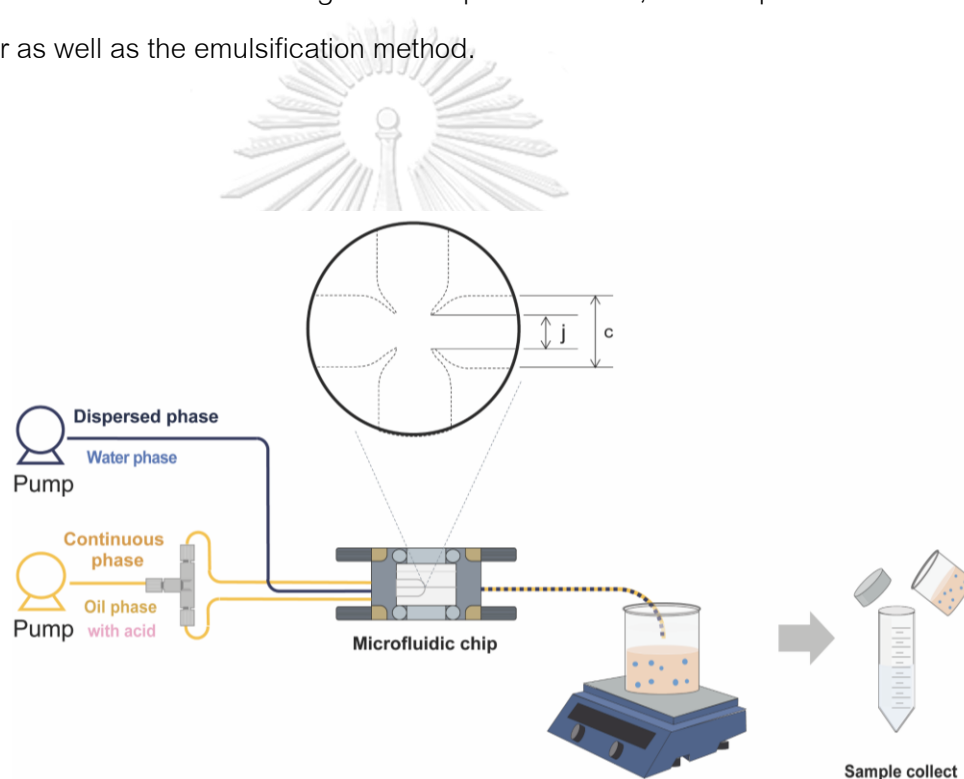


Figure 25 Schematic of microfluidic method for alginate microparticle.

### 3.2.3 Fabrication of single- and multiplied-core-shell of alginate microcapsules via microfluidic flow-focusing

The two flow-focusing channels are set for core-shell microcapsule as shown in Figure 26. The dispersed phase contained any active ingredient in the hydrophobic part which would be the core of the final particle. The continuous phase which would be a shell of the final particle was alginate solution mixed with the crosslinking agent of Ca-EDTA. The oil in water emulsion from the first chip was the dispersed phase of the second chip. The continuous phase of the second chip was an oil phase containing any acid for crosslinking. The single and multiplied-core-shell microcapsules are studied.

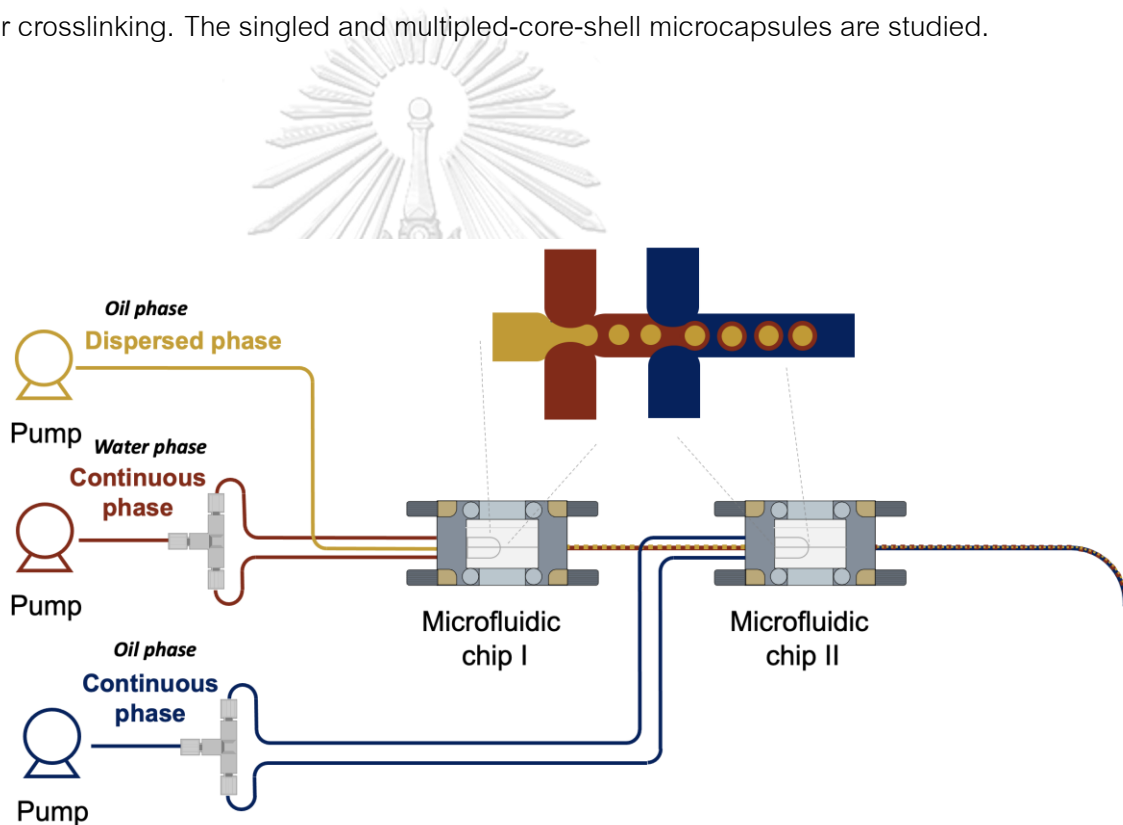


Figure 26 Schematic of core-shell microcapsule formation for experiment.

### 3.3 Fluid properties

The physical properties of the experimental fluids are shown in Table 5. The viscosity ( $\mu$ ) of each phase was measured using a viscometer with an LV2-spindle (model DV2T Brookfield, USA). The pendant drop method was employed to measure the interfacial tensions ( $\sigma$ ) between two immiscible liquids. Liquid density ( $\rho$ ) was determined using a modified pycnometer method. Since the volume of investigated fluid was small, we assumed that the fluid properties remained constant through the channel. For convenience, MIG and JJB mean Miglyol<sup>®</sup> 812 oil and jojoba oil, and the 1, 2, and 3% (w/w) of sodium alginate solution were labeled as 1%A, 2%A, and 3%A respectively.

**Table 5** Physical properties of fluids at 25°C (a) density ( $\rho$ ) and viscosity ( $\mu$ ); (b) interfacial tension ( $\sigma$ )

(a)

Fluid	$\rho$ (kg/m <sup>3</sup> )	$\mu$ (mPa·s)
1%(w/w) Sodium alginate solution	1007	26.94 ± 0.27
2%(w/w) Sodium alginate solution	1008	67.00 ± 0.67
3%(w/w) Sodium alginate solution	1012	148.09 ± 1.48
Miglyol <sup>®</sup> 812 oil	945	38.13 ± 0.38
Jojoba oil	865	46.50 ± 0.47

(b)

Oil phase	Aqueous phase Sodium alginate solution	$\sigma$ (mN/m)
Miglyol <sup>®</sup> 812 oil with 2%(w/w) Span <sup>®</sup> 80	1%	14.11 ± 0.68
	2%	13.42 ± 0.53
	3%	6.29 ± 0.85
Jojoba oil with 2%(w/w) Span <sup>®</sup> 80	1%	9.30 ± 2.52
	2%	2.56 ± 1.27
	3%	0.65 ± 0.18



### 3.4 Characterization

#### 3.4.1 Morphology

The morphology of alginate hydrogels was observed by an optical microscope (model IX71, Olympus, Japan). The dried alginate particles were examined by Emission Scanning Electron Microscope, E-SEM (S-3400N, Hitachi, Japan) operating at 15 kV. The alginate beads and particles were air-dried overnight and coated with gold using a sputter coater (E-1010, Hitachi, Japan) for 60 s.

#### 3.4.2 %Yield

%Yield determination was carried out using the dry weight of the alginate particles ( $W_p$ ) and initial weight ( $W_i$ ). After collecting and redispersing with water, the alginate particles were air-dried on filter paper (Whatman™ No.1) for 24 h at room temperature. The initial weight was counted from alginate and crosslinking agent at each factor. %Yield was calculated using the following formula:

$$\%Yield = \frac{W_p}{W_i} \times 100$$

#### 3.4.3 AFM measurement

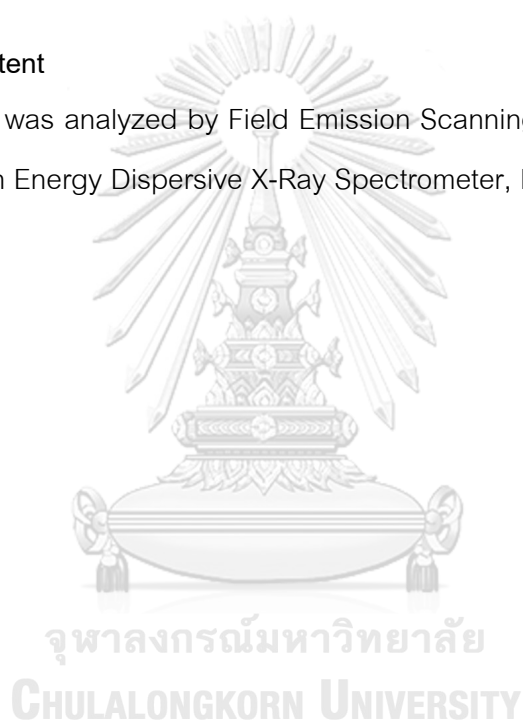
Surface images of alginate microparticles were acquired with a NanoWizard® 3 Bioscience Atomic Force Microscope, AFM (JPK BioAFM, Bruker Nano GmbH, Germany) used in quantitative imaging (QI™) mode. The parameters were set to a Z-length of 2,500 nm and a setpoint of 5 nN for the measurement. Size scan was 5 x 5 μm. The OLTESPA probe (OPUS by MikroMasch, Germany) having a tip radius <7 nm, cantilever force constant of 2 N/m, and resonance frequency of 70 kHz was used. The alginate particles were dropped onto the aminosilane-coated glass slide. The measurements were carried out in water. Polynomial line fit with second order was applied to the AFM height images to subtract surface curvature. The Roughness values (Ra) and apparent Young's modulus ( $E_{app}$ ) was determined using JPK Data Processing software (version spm-6.1.49). The values were calculated based on 5 images at different particles and are reported as mean ± standard deviation.

#### 3.4.4 Rheological properties

Rheological properties of samples were measured using the Modular Advances Rheometer System (HAAKE™ MARS™, Thermo Scientific, USA) equipped with 35 mm diameter plate geometry. The rheology test was performed at room temperature (25°C). In the dynamic measurement, the strain varied from 0.1% to 1000% while keeping the frequency of 1 Hz for strain sweep. In frequency sweep, the frequency range up to 100 Hz was investigated. All measurements were conducted in triplicate.

#### 3.4.5 Ca content

Ca content was analyzed by Field Emission Scanning Electron Microscope, FE-SEM equipped with Energy Dispersive X-Ray Spectrometer, EDX (Versa 3D, FEI, Japan) operating at 10 kV.



## Chapter 4

### Hydrodynamic control of droplet formation in narrowing jet and tip streaming regime using microfluidic flow-focusing

Highly monodisperse droplet production has attracted attention in numerous fields including chemical synthesis [65, 66], cell biology [67, 68], drug delivery and pharmaceuticals [46, 69-71], and food and food supplements [72, 73]. Compared with conventional methods such as mechanical stirrer, high-shear rotor-stator, extrusion, and membrane emulsification, the microfluidic technique provides a droplet with a narrower size distribution. Droplet size can also be controlled and fabricated at low energy consumption using a continuous process, resulting in reduced batch-to-batch variation. Droplet formation can be prepared by an emulsion of two immiscible fluids. A droplet phase is identified as a 'dispersed phase', whereas a 'continuous phase' is identified as a medium phase. Droplets can be generated with various hydrodynamics and characteristics by varying channel geometry. Cross-flow, co-flow, and flow-focusing geometries are the three main types of microfluidic channels. T-junction, which is the cross-flow geometry at 90°, is frequently used due to its simplicity. Flow patterns, flow regimes, and scaling laws have been examined in several models and experimental studies [7, 18, 36, 74-79]. A co-flow setup was developed to produce droplets in a parallel stream by inserting microcapillaries into a channel, while two streams of fluid flowed either in parallel or opposite directions in flow-focusing geometry. The streams of fluid were then forced through a junction to form droplets. Both co-flow and flow-focusing geometries produce droplets with smaller dimensions than the dispersed phase channel, with flow-focusing geometry generating a narrower stream than co-flow. The droplet size is smaller than the orifice diameter to reduce the chance of clogging [14].

Fluid behavior is analyzed by dimensionless numbers including flow rate ratio ( $Q_c/Q_d$ ) and viscosity ratio ( $\mu_c/\mu_d$ ) of a continuous phase to a dispersed phase. With no external force, inertial, viscous, gravity and interfacial forces are dominant for droplet

generation. Thus, several dimensionless numbers have been developed to study fluid behavior. The Reynolds number ( $Re$ ) indicates the relative effect of inertial to viscous force. The  $Re$  typically presents as  $Re \ll 1$  in microfluidic flow, which shows a predominant viscosity over the inertial force. The inertial force plays the least important role in liquid-liquid droplet generation, while the interfacial tension plays a key role. The capillary number ( $Ca$ ) describes the relative effect of viscous force on interfacial force. The Weber number ( $We$ ) represents the relative inertial effect to interfacial force. The Bond number ( $Bo$ ) is defined as the relative buoyancy and surface tension. This is usually negligible in liquid-liquid droplets due to the small difference in densities between the two phases. [15, 16].

The flow-focusing device consists of the main channel and two side channels, in which the two immiscible fluids meet at an intersection. The flow regimes of squeezing and dripping provide monodisperse droplets. The squeezing regime occurs at a low  $Ca$  and flow rate ratio [80]. The squeezing mechanism is conducted by the flow of the continuous phase force to the dispersed phase that then pinches off to form droplets [81-83]. The flow rate of two-phase fluids is the key to the break-up process [84]. In the dripping regime, the viscosity of the fluids is critical to controlling the size distribution of droplets [85]. Interfacial tension was simulated to analyze droplet generation [86]. Liu and Zhang used squeezing and dripping regimes to study the influence of operating parameters such as  $Ca$  and channel geometry. They proposed a scaling model using the three-dimensional lattice Boltzmann model [28]. The increasing flow rate of either phase or both phases caused a transition from dripping to the jetting regime [4, 87-90]. Many studies have analyzed squeezing and dripping regimes but there are no systematic studies on the jetting regime, especially the narrowing jet and tip streaming regimes. This may be due to a lack of stability that is difficult to control. However, tiny uniform droplets that are smaller than the channel size could be created. A submicron emulsion with a narrow size distribution could be generated as a continuous process for 48 h under the tip streaming regime in flow-focusing [90]. The tip streaming regime

occurred at an extremely low dispersed-to-continuous velocity ratio in co-flow geometry [91]. Moreover, high throughput products can be collected at a high flow rate.

Hence, this study investigated droplet generation in a flow-focusing microfluidic device, resulting in the production of monodisperse droplets over a wide range of fluid characteristics and operating parameters. First, the effects of fluid viscosity, interfacial surface tension, density, and flow rate were studied on droplet formation. Second, the narrowing jet and tip streaming regimes were focused on and analyzed. Finally, a dimensionless correlation of these regimes was proposed to predict droplet size.

#### 4.1 Flow regime inside the channel

Water in oil (W/O) emulsion was produced in a junction with 100  $\mu\text{m}$  etch depth. The 2%(w/w) alginate solution and Miglyol<sup>®</sup>812 oil with 2%(w/w) Span<sup>®</sup>80 were used as the dispersed and continuous phases, respectively. The flow rate of the dispersed phase ( $Q_d$ ) and continuous phase ( $Q_c$ ) were controlled. At constant  $Q_d$  of 14.68  $\mu\text{l}/\text{min}$ , five regimes of fluids were observed when increasing  $Q_c$  from 2.25 to 11.08  $\mu\text{l}/\text{min}$ , as shown in Figure 27-(l). The ratio of emulsion droplet size to microfluidic junction size decreased along with the flow rate ratio of the continuous phase to the dispersed phase. Figure 27(a) shows the co-flow regime, in which the dispersed phase fluid was driven in the same direction as the continuous phase fluid. Droplets could not be generated in this regime. When the flow rate of the continuous phase was increased, the dispersed fluid was deformed to the squeezing regime (Figure 27(b)). The droplet size in this regime was larger than the junction size of the microfluidic chip. A uniform droplet size was restricted by the junction size known as “geometry-controlled” [89, 92, 93]. Monodisperse droplets smaller than the junction dimension were found in the dripping regime (Figure 27(d)). The viscous force of the continuous fluid over the interfacial tension effect broke up in the dispersed fluid, occurring near the junction [94]. This phenomenon found in the dripping regime was also reported by Fu et al. [36] when forming uniform particles in a microfluidic T-junction. Several studies [7, 24, 46, 48] reported highly monodisperse microparticle production in the dripping regime. The fluid

was partly broken up, as shown in Figure 27(c) by the squeezing-dripping transition regime, where polydisperse droplets were incurred due to an unstable force balance. Finally, Figure 27(e) shows the reverse regime which arose from the high flow rate range of the continuous phase, with droplets not found in this regime.

Microscopic photos of W/O emulsion droplets were observed in a junction depth of 100  $\mu\text{m}$ , as shown in Figure 28. Monodisperse emulsion droplets are shown in Figure 28(b) and (d) for the squeezing and dripping regimes respectively. Emulsion droplets from the dripping regime were  $62.07 \pm 5.43 \mu\text{m}$ , smaller than droplets from the squeezing regime at  $254.06 \pm 4.56 \mu\text{m}$ . Polydisperse emulsion droplets were found in the squeezing-dripping transition (Figure 28(c)) with emulsion size  $130.16 \pm 49.74 \mu\text{m}$ , while emulsion droplets were not observed in the co-flow and high flow rate ratio regimes, as shown in Figure 28(a) and (e).

When keeping  $Q_d$  constant at 49.33  $\mu\text{l}/\text{min}$ , Figure 27-(II) displays the flow regime in a different way with a long jet. The co-flow regime (Figure 27(f)) was mostly originated. When increasing  $Q_c$ , the fluid thread ejected from the dispersed channel and became polydisperse droplets due to Rayleigh-Plateau instability. This unstable fluid characteristic is known as the “jetting-transition” or “widening jet” regime (Figure 27(g)) [4]. The size of  $174.84 \pm 28.59 \mu\text{m}$  was indicated when  $Q_c/Q_d$  was 1.05. An unsteady thread was resulted by an imbalance force of the two-phase flow. This regime showed polydisperse emulsion droplets of larger size than the junction size (Figure 28(g)).

Regimes which produced smaller uniform droplets than channel size were investigated in this study and high yields of monodisperse droplets were obtained. The “narrowing jet” regime (Figure 27(h)) occurred when the viscous force of the continuous phase predominated over the capillary force. At  $Q_c/Q_d$  of 1.56, the emulsion size was  $97.64 \pm 8.33 \mu\text{m}$  which approximately the range of the junction size found in this regime. The emulsion droplets are shown in Figure 28(h). A very thin jet was dragged and broken up into tiny and uniform droplets as in the tip streaming regime (Figure 27(i)). The droplets were produced from a balance between the shear force of both phases to provide a cone-jet structure. The dispersed fluid became a conical shape resembling

the Taylor cone of electrically conductive liquid in electro spraying. This phenomenon was based on hydrodynamics, not on electrical force. Tip streaming generated smaller droplets compared with the narrowing jet regime. Figure 28(i) shows monodisperse and smallest size of emulsion droplets at  $41.47 \pm 3.62 \mu\text{m}$ , presented at  $Q_c/Q_d$  of 2.09. However, the higher forces from the continuous phase compared with the dispersed phase caused a reversed regime in the channel when the flow rate ratio increased, as shown in Figure 27(j) and emulsion droplets were not observed.



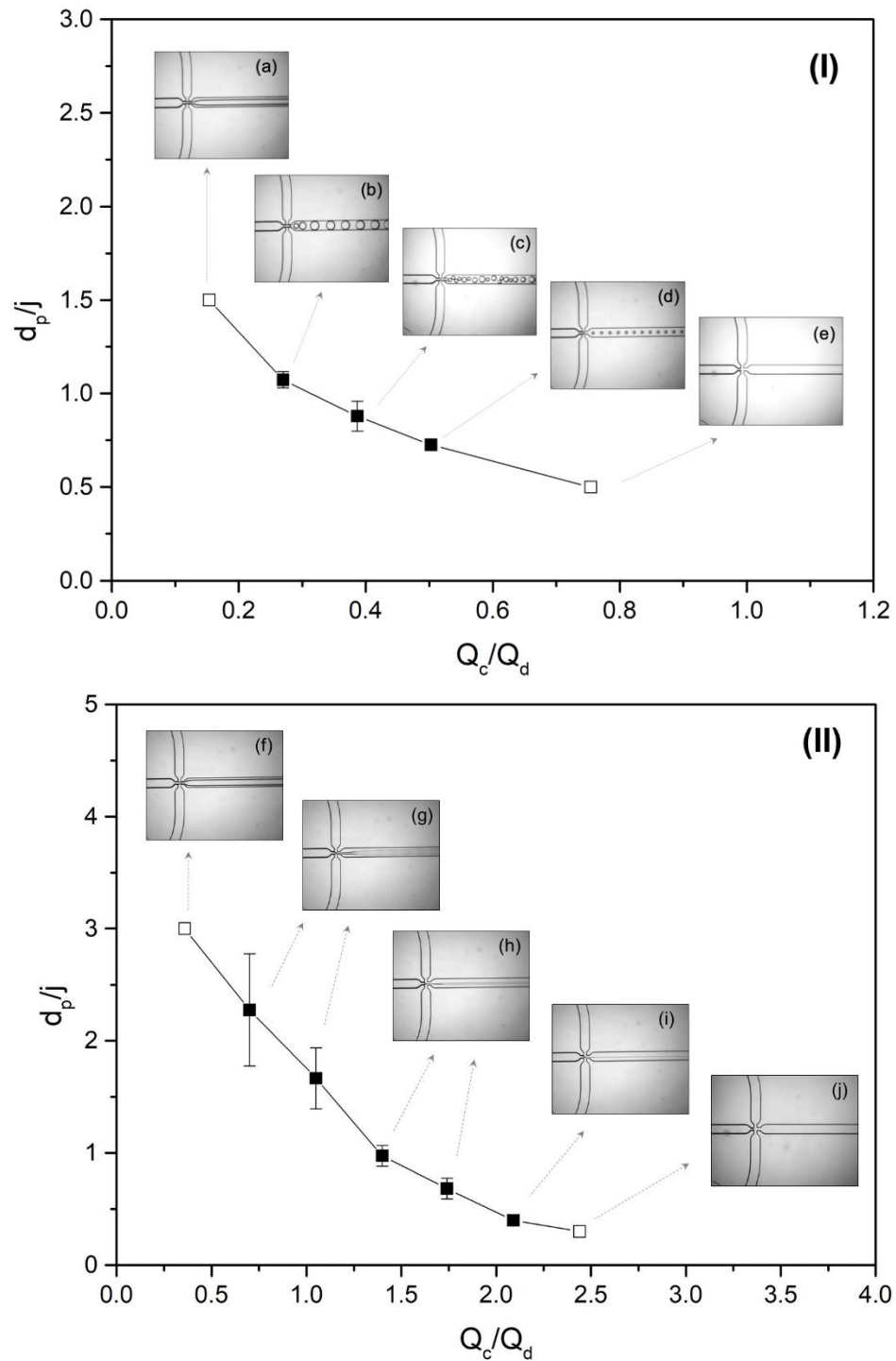
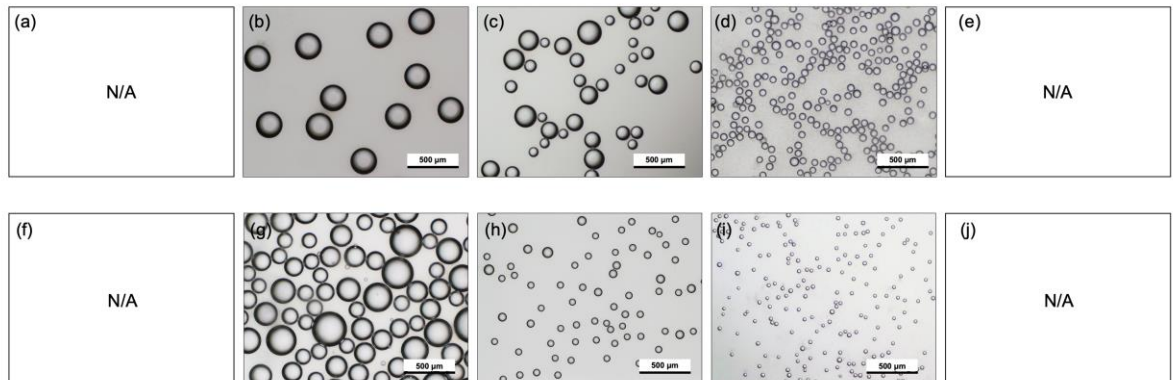


Figure 27 Flow regime inside the channel of 2%(w/w) alginate solution in Miglyol® 812 oil with constant dispersed phase at flow rate of (I) 14.68  $\mu\text{l}/\text{min}$  and (II) 49.33  $\mu\text{l}/\text{min}$  (a) Co-flow; (b) Squeezing; (c) Squeezing-dripping transition; (d) Dripping; (e) Reverse; (f) Co-flow; (g) Widening jet; (h) Narrowing jet; (i) Tip streaming; (j) Reverse).





**Figure 28** Micrograph emulsion droplets of 2%(w/w) alginate solution in Miglyol<sup>®</sup> 812 oil with constant dispersed phase at flow rate of (I) 14.68  $\mu\text{l}/\text{min}$  and (II) 49.33  $\mu\text{l}/\text{min}$  (a) Co-flow; (b) Squeezing; (c) Squeezing-dripping transition; (d) Dripping; (e) Reverse; (f) Co-flow; (g) Widening jet; (h) Narrowing jet; (i) Tip streaming; (j) Reverse) in a junction depth of 100  $\mu\text{m}$ .

#### 4.2 Effect of fluids Interfacial tension on the droplet formation in the narrowing jet and tip streaming regime

In microfluidics, droplet creation is created when the interfacial tension between two phases is deformed. Surfactants are commonly used to reduce the liquid surface tension or interfacial tension of a two-phase system. Because of mass transport, an addition of surfactants reduces the time of droplet creation. During the squeezing and dripping regimes, in which droplet production mainly depends on shear force and interfacial tension, droplet size is varied by the concentration of surfactant. Droplet size decreased with reduction of interfacial tension because the shear force easily broke the interfacial tension [95]. However, a small amount of surfactant encouraged the tip streaming effect. Surfactant also plays a key role in the tip streaming regime. The surfactant molecules, which often dissolve in the continuous phase, are diffused into the interface when two phases meet at the junction. Adsorption and desorption occur until they reach equilibrium. The flow of continuous fluid drives the surfactant molecules to form a steady cone-jet structure. So, the steady tip streaming effect is affected by both fluid properties and the fluid flow rate.

Figure 29 shows the effects of interfacial tension at a high flow rate in microfluidics. The presence of the surfactant impacted thread stability, especially at low  $Q_c/Q_d$ . However, at high  $Q_c/Q_d$ , a stable with a slender thread was found either with or without surfactant. The stable region produced uniform droplets (Figure 29(c,e,f,g,h,i)), while polydisperse droplets were investigated in the unsteady region (Figure 29(a,b,d)). To verify the shape of thread to the polydispersity of droplets, the coefficients of variation (CV) of emulsions droplets were determined. The widening jet regime (Figure 29(a,b,d)) displays the formation of polydisperse droplets of larger size compared with the junction size. The CV of droplets from Figure 29(a), 27(b), and 27(d) were 16.85, 13.13, and 11.72, respectively. While droplets similar to the junction size were found in the narrowing jet and tip streaming (Figure 29(c,e,f,g,h,i)). When they reached a balance, tiny droplets with uniform size were obtained. Droplet size was influenced by the flow rate ratio of both phases when increasing  $Q_c/Q_d$  resulted in a smaller droplet size. The CV of droplets from Figure 29(c), 29(e), 29(f), 29(g), 29(h), and 29(i) were 9.04, 9.51, 9.97, 8.89, 7.92, and 9.81, respectively. Results verified the monodispersity since the CV was smaller than 10%, as the standard criterion for monodispersity [96-98].

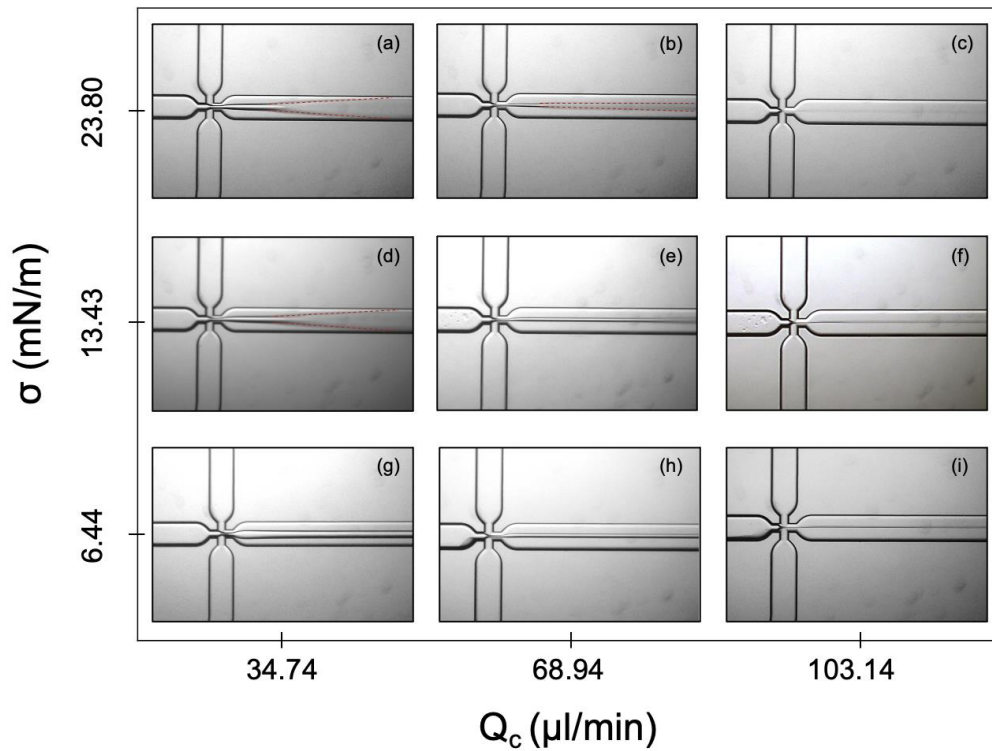


Figure 29 Micrograph emulsion droplets of 2%(w/w) alginate solution in Miglyol<sup>®</sup> 812 oil with Experimental images of fluid characteristics in a microfluidic channel showing the effect of interfacial tension ( $\sigma$ ) on tip streaming state at different continuous phase flow rate ( $Q_c$ ) (2%(w/w) alginate droplets in Miglyol<sup>®</sup> 812 oil system at dispersed phase flow rate of 49.33  $\mu\text{l}/\text{min}$  in a junction depth of 100  $\mu\text{m}$ ).

((a)-(c)  $\sigma = 23.80$  mN/m which  $Q_c$  of (a) 34.74, (b) 68.94, and (c) 103.14  $\mu\text{l}/\text{min}$ ,

(d)-(f)  $\sigma = 13.43$  mN/m which  $Q_c$  of (d) 34.74, (e) 68.94, and (f) 103.14  $\mu\text{l}/\text{min}$ ,

and (g)-(i)  $\sigma = 6.44$  mN/m which  $Q_c$  of (g) 34.74, (h) 68.94, and (i) 103.14  $\mu\text{l}/\text{min}$ ).

Since a larger production will be obtained, the production of droplet streams at the high flow process is very challenging. The tip streaming regime was generated in the flow-focusing device when operated within the parametric range. When the two streams met at the microfluidic junction, the viscous force of the continuous phase acted to deform the interface, while deformation was resisted by interfacial tension. Molecules of the surfactant diffused to the fluid interface and were carried by the fluid flow towards the pole. Accumulation of surfactant molecules at the pole caused overwhelming adsorption on the interface over desorption. As a result of these molecular motions, interfacial tension at the pole reduced near to zero. Surface curvature increased to maintain the stress balance at the interface. At high curvature, the viscous forces dragged a thread from the tip that then broke into droplets due to the Rayleigh breakup mechanism [89]. So, the formation of monodisperse droplets relied on the balance of two-phase effects from both fluid properties and fluid force. However, backward flow was excessive. Thus, droplet formation in the tip streaming regime depended on both fluid properties and flow rate.

#### 4.3 Flow regime

The capillary number ( $Ca$ ) describes the relative effect of viscous forces to interfacial tension forces affecting droplet formation and is defined as:

$$Ca = \frac{\mu v}{\sigma} \quad (5)$$

where  $\mu$  is the viscosity of the fluid (mPa·s);  $v$  is the velocity of the fluid (m/s) and  $\sigma$  is the interfacial tension between the dispersed and continuous phases (mN/m).  $Ca$  of the continuous phase ( $Ca_c$ ) is frequently used to investigate droplet production because the balance of shear stress and interfacial tension. The  $Ca_c$  value was determined using the viscosity and velocity of the continuous phase. The squeezing regime which generated geometry-controlled droplets occurred at low capillary number. Increasing  $Ca_c$  caused a dripping regime where the interfacial tension was broken by the viscous

force [16]. Figure 30 shows the flow regime of 2%(w/w) alginate droplets in Miglyol<sup>®</sup> 812 oil for various  $Ca$  of continuous and dispersed phases. Co-flow, squeezing, transition, dripping and reverse regimes were found when  $Ca_d$  was lower than 0.031. The green circle and light blue square represent the squeezing and dripping zones where monodisperse droplets were generated. However, these two zones were not found when  $Ca_d$  was higher than 0.031, where four regimes of co-flow, jetting, tip streaming and reverse were observed. The dark blue diamond symbol shows the tip streaming regime. Comparing with the dripping regime, a larger area of tip streaming production was found. Moreover, higher yields of monodisperse and smaller droplets than junction size were produced via tip streaming due to the higher dispersed flow rate.



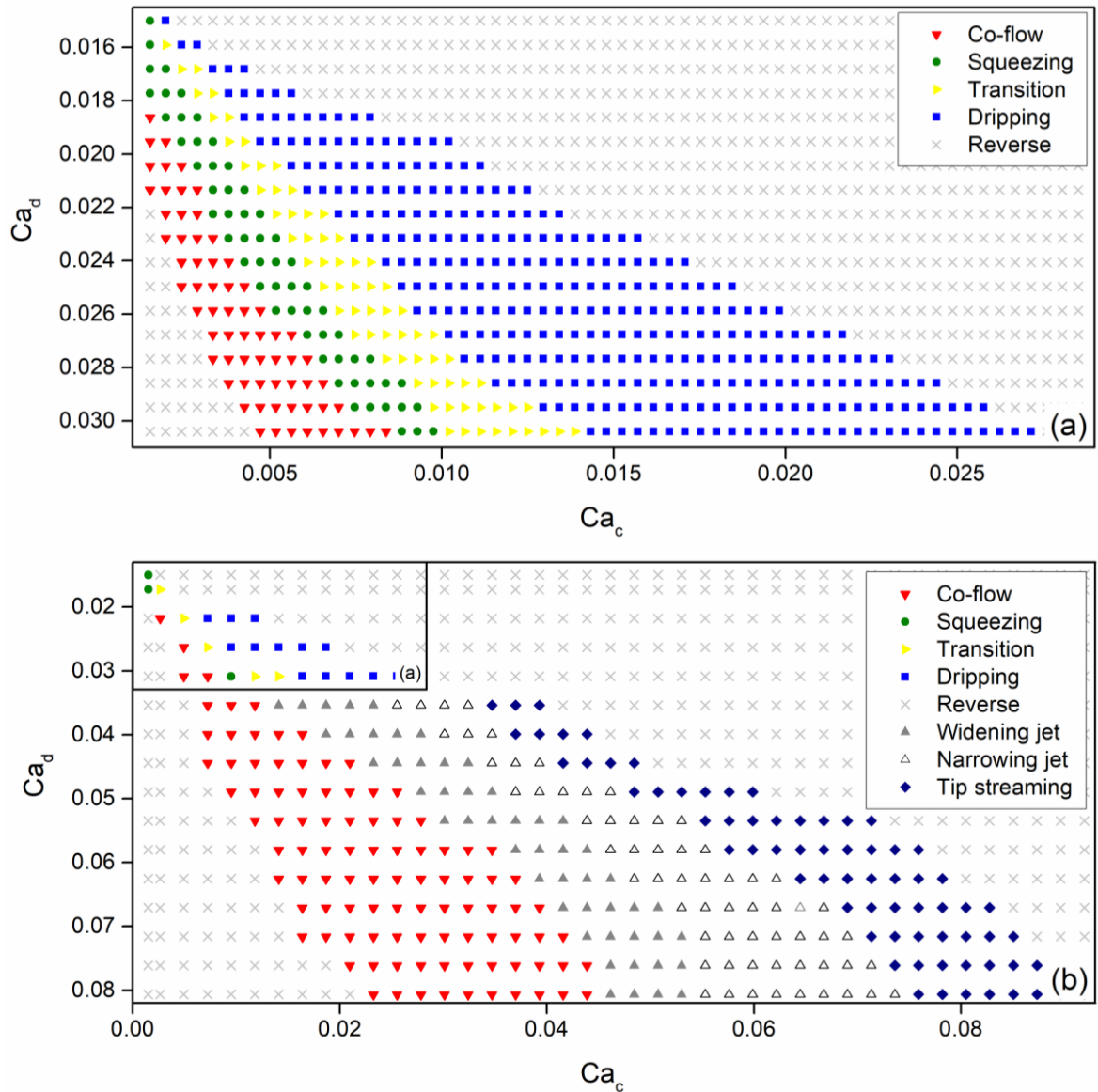


Figure 30 Flow regime of 2%(w/w) alginate droplets in Miglyol® 812 oil at various capillary numbers of dispersed phase ( $Ca_d$ ) and continuous phase ( $Ca_c$ ) in junction depth 100  $\mu\text{m}$  (a)  $Ca_c$  of  $Ca_c$  at 0.0015 - 0.0285 and  $Ca_d$  at 0.015 - 0.038 and (b) flow regimes at  $Ca_c$  and  $Ca_d$  up to 0.0896 and 0.0807 respectively.

The transition between different regimes occurred by changing dispersed and/or continuous phase capillary numbers. The turning point from the squeezing to the dripping regime was characterized by a critical capillary number of the continuous phase ( $Ca_{crit}$ ) [99]. A larger  $Ca_{crit}$  indicated a higher fluid viscosity.  $Ca_{crit}$  values of 0.001 to 0.005 and 0.002 to 0.015 were explored in water-MIG and 2%Al-MIG systems respectively. Figure 30(a) shows the turning point to a dripping regime in the 2%Al-MIG system. A larger viscosity of the dispersed phase stabilized the interface, while  $Ca_{crit}$  tended to increase with decreasing viscosity ratio ( $\mu_c/\mu_d$ ). Concurring with the literature,  $Ca_{crit}$  was reported as a transition point between values of 0.002 to 0.01 [100] and 0.01 to 0.1 [101] in the T-junction device and  $Ca_{crit} \geq 0.01$  in the flow-focusing device [88].

In the 2%Al-MIG system, when  $Ca_d$  was higher than 0.031, the flow-regime pattern changed. As mentioned earlier, jetting and tip streaming were found instead of squeezing and dripping regimes. A turning point to the tip streaming regime that produced monodisperse emulsion droplets also occurred at  $Ca_c > Ca_{crit}$ . From  $Ca_d$  of 0.031 to 0.081, a turning point to the tip streaming regime was shown at  $Ca_c$  values from 0.037 to 0.076. However, in the water-MIG system (not shown), the flow regime pattern changed when  $Ca_d$  was higher than 0.128. A turning point to the tip streaming regime occurred at  $Ca_c$  of 0.015 to 0.046, with  $Ca_d$  of 0.128 to 0.535.

#### 4.4 Effect of flow rate ratio and viscosity ratio on the ratio of droplet size to junction size

Flow rates of the dispersed and continuous phases were controlled. Droplet size ( $d_p$ ), averaged from a minimum of 100 droplets, was normalized by junction size ( $j$ ). Flow rate ratio ( $Q_c/Q_d$ ) (0.11 to 8.34) of Miglyol<sup>®</sup> 812 oil and jojoba oil and three concentrations of alginate solution (1, 2 and 3%(w/w)) in an aqueous phase were studied. Figure 31 shows the relationship between flow rate ratio ( $Q_c/Q_d$ ) and the proportion of droplet size and junction size ( $d_p/j$ ). Figure 31(a) shows results under  $Ca_d$  of 0.031 in the system of 2%(w/w) alginate solution and Miglyol<sup>®</sup> 812 oil in junction depth of 100  $\mu\text{m}$ , in which all droplets were in a squeezing-dripping transition and a dripping regime. Increase in the flow rate ratio resulted in decrease in droplet size, concurring with a previous study [22].

Droplet size decreased with increasing continuous phase flow rate when the dispersed phase flow rate was kept constant. By contrast, when keeping the continuous phase flow rate constant, increase in the dispersed phase flow led to increased droplet size. At high flow rates of the continuous phase, the high shear force interrupted the dispersed phase, resulting in breaking up into smaller droplets.

Likewise, continuous phase resistance occurred at a higher flow rate of the dispersed phase ( $Ca_d$  higher than 0.031), as shown in Figure 31(b). The bars in Figure 31 represent droplet size distribution. Narrow size distribution was found at low  $d_p/j$ , especially under 1. Results revealed that uniform and smaller droplet sizes were obtained at dripping, narrowing jet and tip streaming regimes compared with the junction size. The transition regime contained larger droplet size than the junction droplets.

**Table 6** Fluid viscosity ratios ( $\mu_c/\mu_d$ )

Aqueous phase	Oil phase	$\mu_c/\mu_d$
Sodium alginate solution	Miglyol <sup>®</sup> 812 oil	1.42
	Jojoba oil	1.73
2%	Miglyol <sup>®</sup> 812 oil	0.57
	Jojoba oil	0.69
3%	Miglyol <sup>®</sup> 812 oil	0.26
	Jojoba oil	0.31



The graph also indicates the trend of viscosity ratio ( $\mu_c/\mu_d$ ) observed from various concentrations of sodium alginate solution and the two types of oil (Table 6). The blue zone in Figure 31 represents  $\mu_c/\mu_d$  of 3%(w/w) sodium alginate droplets with Miglyol<sup>®</sup> 812 oil and jojoba oil. This showed the lowest  $\mu_c/\mu_d$  for monodisperse droplet production ( $d_p/j < 1$ ) at high  $Q_c/Q_d$ . Higher viscosities of the dispersed fluid (lower  $\mu_c/\mu_d$ ) showed higher flow rate of the continuous phase to maintain droplet size due to liquid flow resistance. By contrast, higher viscosity of the continuous phase (higher  $\mu_c/\mu_d$ ) exerted a larger shear force on the dispersed phase and a lower flow rate was needed for droplet production. Droplet size increased with decreasing  $\mu_c/\mu_d$  (i.e., high  $\mu_d$  or low  $\mu_c$ ) when keeping  $Q_c/Q_d$  constant. Low  $\mu_c$  value reduced the shear force in droplet production. This pronounced effect of viscosity was found in every phase.



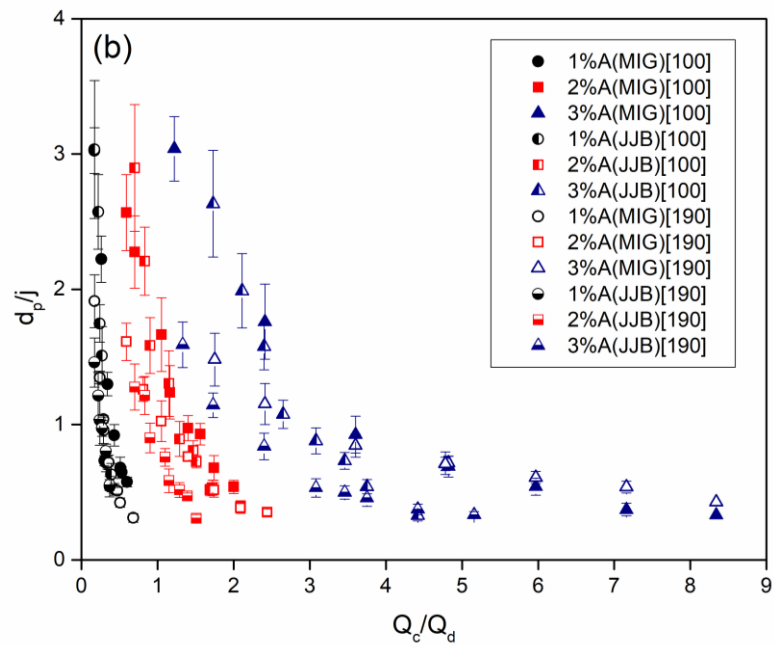
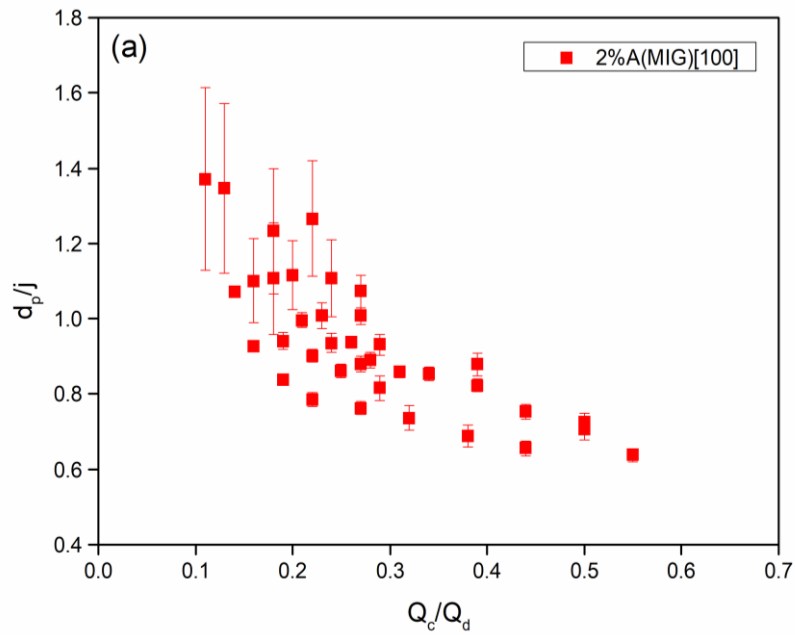
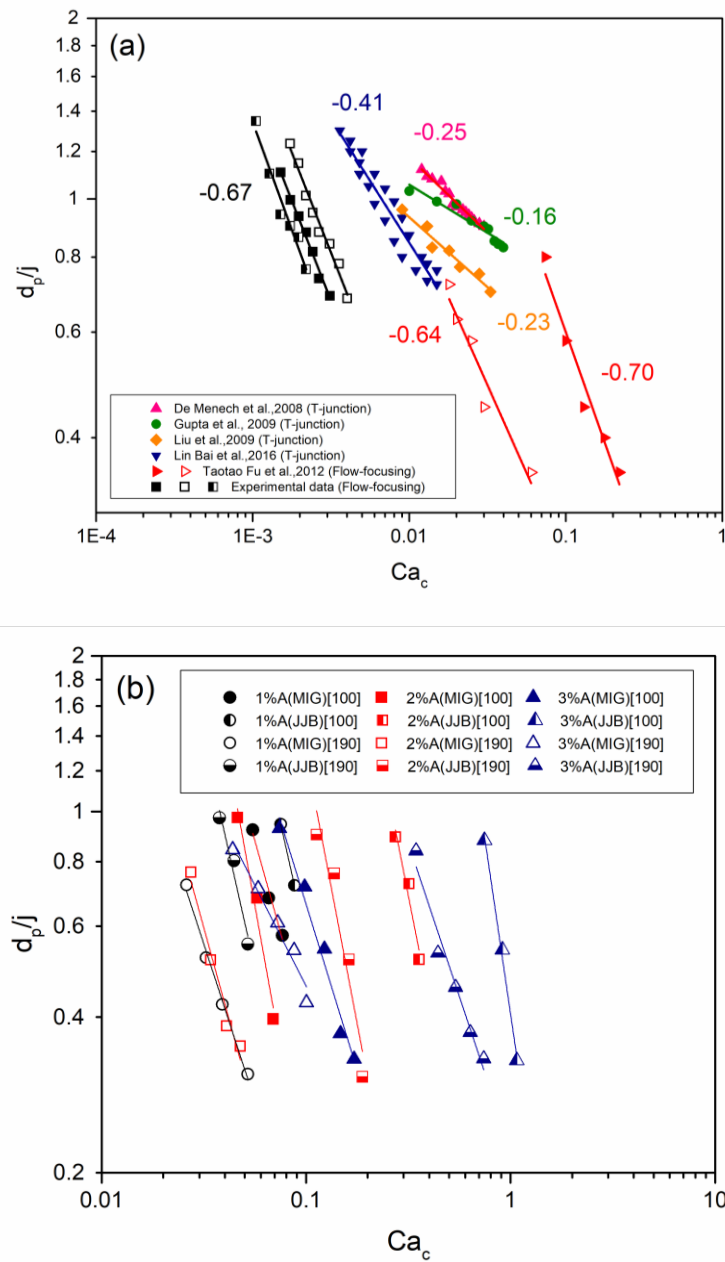


Figure 31 Effect of flow rate ratio ( $Q_c/Q_d$ ) on droplet size ( $d_p$ ) normalized by junction size ( $j$ ) (a) when  $Ca_d$  was lower than 0.031 and (b) when  $Ca_d$  was higher than 0.031 at different conditions. Legends refer to dispersed phase (continuous phase)[junction size].

#### 4.5 Dimensionless correlation for droplet formation in the narrowing jet and tip streaming regimes

The capillary number of the continuous phase ( $Ca_c$ ) that defines viscosity and velocity is an extensive parameter that correlates droplet size in the dripping regime due to the dominance of shear force [16]. Fitting of the experimental results and literature data in the power law relationship is shown in Figure 32(a). The scaling power of  $Ca_c$  was observed from -0.10 to -0.40 in T-junction [30, 94, 101, 102] and -0.64 to -0.70 in flow-focusing [103]. Our experimental results, whereby droplets formed in a flow-focusing device, showed the power law of -0.67. Three sets of results with different systems showed the same power law correlation. The negative power was reported due to droplet size decreasing with the increasing capillary number of the continuous phase. The capillary number was increased due to the increase of the continuous phase flow rate. The high shear force of the continuous phase interrupted the dispersed phase, resulting in breaking up into smaller droplets. However, different zones of the fitting curve were re-done since different fluid viscosities were used in similar microfluidic geometry. Moreover, different values were investigated because of the different fluid properties.

Figure 32(b) shows the fitting relationship in the narrowing jet and tip streaming regimes presented at  $Ca > Ca_{crit}$ . Results showed that  $d_p/j$  was lower than 1, indicating smaller emulsion droplets than the junction size. All systems showed the same trend in which droplet diameter decreased when  $Ca_c$  increased. The scaling power of  $Ca_c$  was from -1.10 to -1.80 depending on the kind of fluid. For the 2%Al-MIG system in 100  $\mu\text{m}$  junction depth, scaling powers were -0.67 for the dripping regime and -1.35 for the tip streaming regime. However, droplet creation in the tip streaming regime occurred from the effect of viscous forces on interfacial tension forces and from the effects of both fluid properties and fluid force.



**Figure 32** Correlations of droplet size ( $d_p$ ) normalized by junction size ( $j$ ) at varied capillary number of continuous phase ( $Ca_c$ ) for (a) dripping and (b) narrowing jet and tip streaming. (For interpretation of the references in this figure legend, please refer to the web version of the article).

The tip streaming regime was attractive due to smaller size droplets with high production yield. However, the narrowing jet regime was also remarkable because of droplet size distribution. Coefficients of variation (CV) of tip streaming at  $Q_c/Q_d$  of 2.09 and narrowing jet at  $Q_c/Q_d$  of 1.56 were 8.73 and 8.53 respectively. Both showed monodisperse emulsion size smaller than junction size. Thus, we focused on the correlation of these two regimes. The viscous force and interfacial tension, represented by the capillary number, are dominant in curve creation, while the flow balance between two phases is also crucial in stretching and leads to thread formation. As previously discussed, viscosity is a liquid property that influences the force balance in droplet generation.  $Q_c/Q_d$ ,  $\mu_c/\mu_d$  and  $Ca_c$  are used to express the dimensionless droplet size to junction size. From the experimental results, the droplet size ( $d_p$ ) normalized by the junction size ( $j$ ), was expressed in terms of the dimensionless numbers  $Q_c/Q_d$ ,  $\mu_c/\mu_d$  and  $Ca_c$  when a smaller emulsion droplet than the junction size ( $d_p/j$  under 1) was formed by the narrowing jet and tip streaming regimes.

$$\frac{d_p}{j} = 0.53 \left( \frac{Q_c}{Q_d} \right)^{-1.19} \left( \frac{\mu_c}{\mu_d} \right)^{-1.56} (Ca_c)^{-0.03} \quad (6)$$

Figure 33 shows the droplet size ( $d_p$ ) normalized by junction size ( $j$ ) as predicted by the correlation fit, with 12 experiments providing over 100 data points of the two sizes of microfluidic channels. The operation condition was performed at the dispersed phase flow rate in the range  $7 < Q_d < 315$   $\mu\text{l}/\text{min}$ . The continuous phase flow rate in the range  $15 < Q_c < 137$   $\mu\text{l}/\text{min}$  covered  $Q_c/Q_d$  in the range 0.17 to 8.34. Viscosity and interfacial tension between both phases varied from 26.94 to 148.00  $\text{mPa}\cdot\text{s}$  and 0.65 to 14.11  $\text{mN}/\text{m}$  respectively. Model performance with the sum square error (SSE) of 1.09 and root mean square error (RMSE) of 0.138 was evaluated. Errors lower than  $\pm 10\%$  were found. Because of the tip streaming and narrowing jet regimes, a smaller emulsion size than the junction size was formed ( $d_p/j < 1$ ). Over this point, the droplets merged into larger droplet sizes.

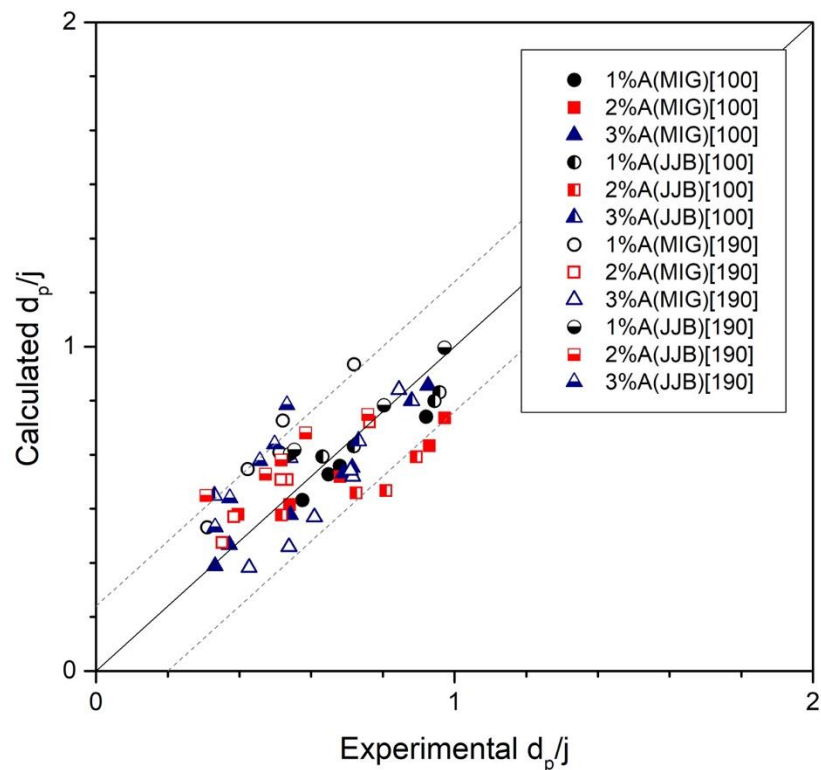


Figure 33 Comparison of the calculated and experimental data.

Legends in the graph refer to dispersed phase (continuous phase)[junction size].

Droplet generation in the microchannel depends on various parameters. Correlation of droplet size was reported in the squeezing regime, as shown in Table 7 since it was an initial regime. Correlation was indicated in terms of the dispersed phase length ( $L$ ) in the squeezing regime because of larger droplet size than the geometry size. However, the droplet size was used because of smaller droplet size than geometry size in the dripping and tip streaming regimes. The correlation of droplet size in the narrowing jet and tip streaming regimes considered all parameters that affected the production of droplets in microfluidic flow-focusing proposed in this study. This correlation can be used to predict and control droplet generation at high production rates as well as droplet size prediction.

Table 7 Droplet size correlation

Flow regime	Channel geometry	Correlation	Reference
Squeezing	Cross-flow (T-junction)	$\frac{L}{w_c} = 1 + Q$	[18]
	Cross-flow (T-junction)	$\frac{L}{w_c} = \varepsilon + \omega Q$	[100]
	Flow- focusing	$\frac{L}{w_c} = k \left( \frac{Q_d}{Q_c} \right)^\alpha Ca^\beta$	[37]
	Flow- focusing	$\frac{L}{w_c} = (\varepsilon + \omega Q) Ca^m$	[18, 28]
	Cross-flow (T-junction)	$\frac{L}{w_c} = k \left( \frac{Q_d}{Q_c \sin\theta + \lambda \cot\theta} \right)^\alpha Ca^\beta$	[51]
	Cross-flow (T-junction)	$\frac{L}{w_c} = 0.92 \left( \frac{Q_c}{Q_d} \right)^{-0.22} Ca_c^{-0.36} El^{0.08}$	[78]
	Flow- focusing	$\frac{L}{w_c} = \frac{\varepsilon(e^{\cos\theta})^n + \omega Q}{(2\sin\theta) + \lambda \omega \cot\theta} Ca^m$	[104]
	Flow- focusing	$\frac{L}{w_c} = 0.211 Q^{0.35} Ca_c^{-0.4}$	[105]
	Flow- focusing	$\frac{L}{w_c} = \varepsilon + \omega Q^a Ca_c^b$	[106]
Dripping	Co-flow	$\frac{d_p}{d_{1i}} = 0.234 K \cdot Ca_c^{-0.312} Ca_d^{0.187} Re_d^{-0.203}$	[107]
	Cross-flow (T-junction)	$\frac{d_p}{d_i} = 0.23 \cdot \mu_c^{0.21} \nu^{-0.31} \sigma^{0.31}$	[101]

Table 7 Droplet size correlation (Cont.)

Flow regime	Channel geometry	Correlation	Reference
Tip streaming	Co-flow	$\frac{d_d}{D} \propto \left(\frac{d_j}{D}\right) k^{1/3} = 1.25k^{1/3} \left[\frac{Q_i}{v_0 D^2}\right]^{1/2}$	[108]
Jetting	Flow-focusing	$\frac{d_p}{j} = 3.1 \left(\frac{Q_d}{Q_c}\right)^{1/2}$	[109]
Narrowing jet and tip streaming	Flow-focusing	$\frac{d_p}{j} = 0.53 \left(\frac{Q_c}{Q_d}\right)^{-1.19} \left(\frac{\mu_c}{\mu_d}\right)^{-1.56} (Ca_c)^{-0.03}$	This study





## Chapter 5

### Internal gelation of alginate microparticle prepared by emulsification and microfluidic method: Effect of Ca-EDTA as a calcium source

Alginate, a biopolymer derived from brown seaweeds, is composed of (1-4)-linked  $\beta$ -D-mannuronic (M) and  $\alpha$ -L-guluronic acid residues (G). It is generally recognized as a safe (GRAS) material by the US Food and Drug Administration (FDA) [110] and is a "not specific" acceptable daily intake (ADI). It is biodegradable, biocompatible, non-toxic, relatively low cost, soluble in water, and thermally stable, resulting in one of the widely used biomaterials for drug delivery [111, 112], tissue engineering [113], biomedical [114, 115] waste-water treatment [116-118], food and supplement [119-123]. Its three-dimensional network, in which cations are interacting with carbonyl groups of guluronate moieties, could generate an alginate matrix. The gelation mechanism is called the "egg-box" model, which is ionotropic gelation causing the formation of a strong thermostable material. The binding relevance for cations increases in the following order:  $Mg^{2+} \ll Mn^{2+} < Zn^{2+} < Ni^{2+} < Co^{2+} < Ca^{2+} < Sr^{2+} < Ba^{2+} < Cd^{2+} < Cu^{2+} < Pb^{2+}$ , with a higher relevance resulting in a stronger gel [124-126]. However, calcium is the most commonly used gelation agent due to its nontoxicity and low cost. Moreover, the use of Ca is acceptable for food and pharmaceutical applications.

The simplest and the most commonly used technique to fabricate alginate particles for encapsulation applications is extrusion/external gelation, by which the alginate is extruded from a nozzle. The technique is called the dripping method. The alginate solution was extruded through a nozzle into the air phase. It became dropwise into a gelling bath containing cations such as calcium chloride ( $CaCl_2$ ), the most used ionic crosslinking agent. The gelation of alginate is highly dependent on the concentration of the crosslinker agent. It increases entrapment efficiency and decreases active ingredient release with increasing  $CaCl_2$  [127, 128]. The alginate beads prepared by external gelation usually are larger than 1,000  $\mu m$  [42] with an inhomogeneous

structure [129]. The cations diffuse from the outside into the internal alginate phase and form an alginate matrix, resulting in a gel-like state with the high crosslinking density of alginate reducing in the interior and the calcium at the surface [130-133]. This was a limitation of external crosslinking. In addition, the dense peripheral matrix inhibits the exchange of ions between the particle core and the environment [134]. Although the size of bead is typically highly uniform, the main limitation of extrusion/external gelation is the large size of alginate bead, which depends on the diameter of the nozzle extruder.

In the internal gelation, also known as *in situ* gelation, the divalent cations are released internally from the alginate phase. The alginate solution containing a calcium source would emulsify into an oil phase. The calcium remains in solution but cannot crosslink with alginate chains. By adding acid, the detachment of the complex releases the calcium ions to react with the alginate chains. Therefore, the selection of a calcium source for internal gelation is critical. It was reported that calcium carbonate ( $\text{CaCO}_3$ ) could provide the alginate beads with more spherical, stable, and uniform than calcium salt from oxalate, tartrate, phosphate and citrate [135]. However, mechanical and rheological properties were dependent on  $\text{CaCO}_3$  concentration. A high concentration of  $\text{CaCO}_3$  made alginate gel stiffer and denser than a low concentration [136]. In terms of morphology, size and size distribution of alginate particles, emulsification/internal gelation from  $\text{CaCO}_3$  was better than  $\text{CaCl}_2$  in emulsification/external gelation [137]. However, the suspension of  $\text{CaCO}_3$  in sodium alginate solution might obstruct the emulsification, producing particles with a board size distribution [138].

The gelation method is critical in controlling particle uniformity and crosslink density when using divalent ions. Slower gelation produces more uniform structures and greater mechanical properties. Moreover, internal gelation has an advantage in biphasic system in prevention of coagulation into large masses before properly hardening. Especially in the droplet microfluidic technique which needs to use immiscible fluid to fabricate droplet. The superior benefit of internal gelation is controlling the shape of particle. The spherical shape will be maintained in both microparticles and microcapsules.

Here, we explore deeply for the first time the water-soluble calcium-ethylenediaminetetraacetic acid (Ca-EDTA) complex as  $\text{Ca}^{2+}$  source for crosslinking reaction via internal gelation. Production of alginate microparticles was achieved by two methods: water in oil (W/O) emulsification and the microfluidic technique. The effect of emulsification speed, Ca-EDTA concentration, crosslinking time were investigated in terms of morphology, %yield, mechanical properties, rheological properties, and final Ca content from EDX analysis for considering crosslink density. Moreover, the optimal operating conditions in the microfluidic technique were determined to achieve best size control of the internal gelation-alginate particles.

### 5.1 Mechanism of internal gelation using Ca-EDTA as a calcium source

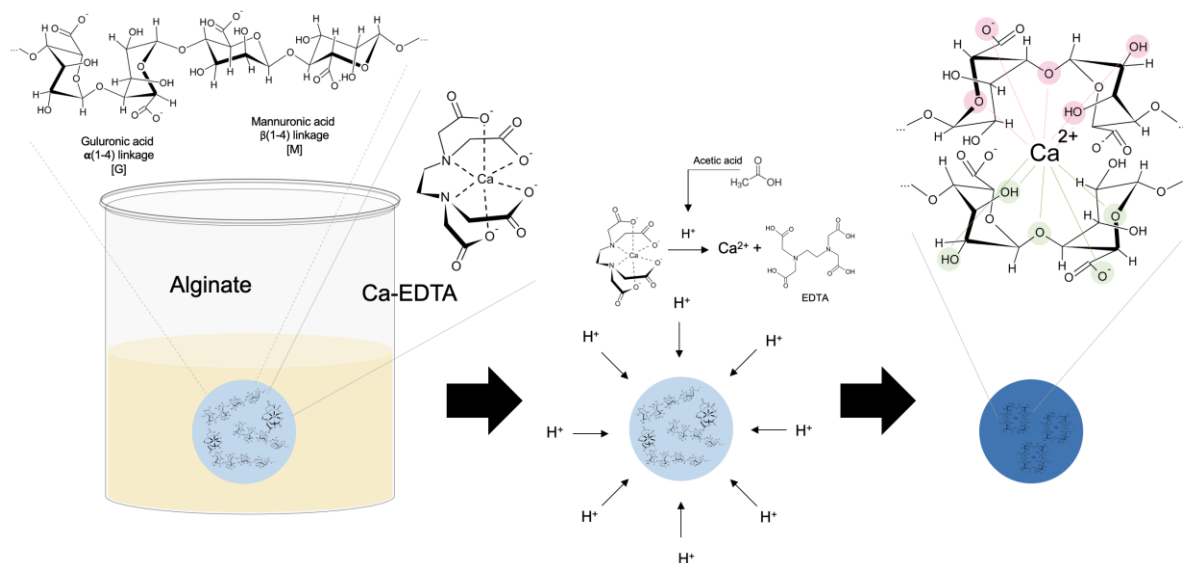


Figure 34 Illustration of the internal crosslink process.

The alginate particles were prepared by internal gelation which could control the gelation by slowly releasing  $\text{Ca}^{2+}$ . Internal gelation was interested due to the crosslinking being initiated and occurring inside the alginate droplet which overcome the problem of clumping encountered in external gelation. Moreover, the gelation enabled the design of

the crosslink density. We used the Ca source in the form of a water-soluble calcium-ethylenediaminetetraacetic acid (Ca-EDTA) complex. With the chelation of  $\text{Ca}^{2+}$  with EDTA, the ions remained in the solution but inaccessible to the alginate chains. The superior advantage of Ca-EDTA is soluble calcium with water, which can well mix with sodium alginate solution. In contrast,  $\text{CaCO}_3$ , the most popular calcium source, has low solubility and can hinder emulsification [138]. The dissolution of calcium source caused a heterogeneous distribution of  $\text{Ca}^{2+}$  inside particles, resulting in the broad size distribution of resulting particles.

The homogenous solution could provide a uniform gel structure. The  $\text{Ca}^{2+}$  reacted with alginate chains in a highly controlled way forming alginate gel with excellent structure. Figure 34 shows the schematic illustration of internal crosslink using Ca-EDTA as a calcium source. The Ca-EDTA was completely dissolved in sodium alginate solution. The droplets of sodium alginate solution with Ca-EDTA were emulsified as a water in oil emulsion. The emulsification and microfluidic technique were used to form the W/O emulsion droplets. Without hydrogen ion ( $\text{H}^+$ ), the Ca-EDTA complex was highly stable. Therefore, the calcium remained complexed in the solution and could not crosslink with alginate chains. The  $\text{Ca}^{2+}$  was released by manipulating the content of  $\text{H}^+$  by the addition of acetic acid. In the emulsification method, the acetic acid was added after the W/O emulsification ended (Figure 24), whereas it was added to oil phase in the process of reducing particle size in the microfluidic technique (Figure 25). Hydrogen ion diffused to the water dispersed phase and encountered the calcium complex. The  $\text{Ca}^{2+}$  was released immediately and alginate gel *in situ* formed a homogeneous gel network. However, the  $\text{H}^+$  also competed with  $\text{Ca}^{2+}$  to interact with the alginate chains. Thus, manipulating acetic content in the medium phase was the key factor in the internal gelation method [130, 132]. The experiment observed that the alginate particles were formed at an acetic acid concentration over of 0.05%(v/v) (the concentration of acid was calculated based on total volume of W/O emulsion). This result indicates that at a concentration higher than 0.05%(v/v), the  $\text{Ca}^{2+}$  tended to discharge and crosslink with the alginate chain. Finally, the alginate particles were formed via ionotropic gelation. The

particles size was varied due to the preparation method and the conditions that were used (Figure 35).

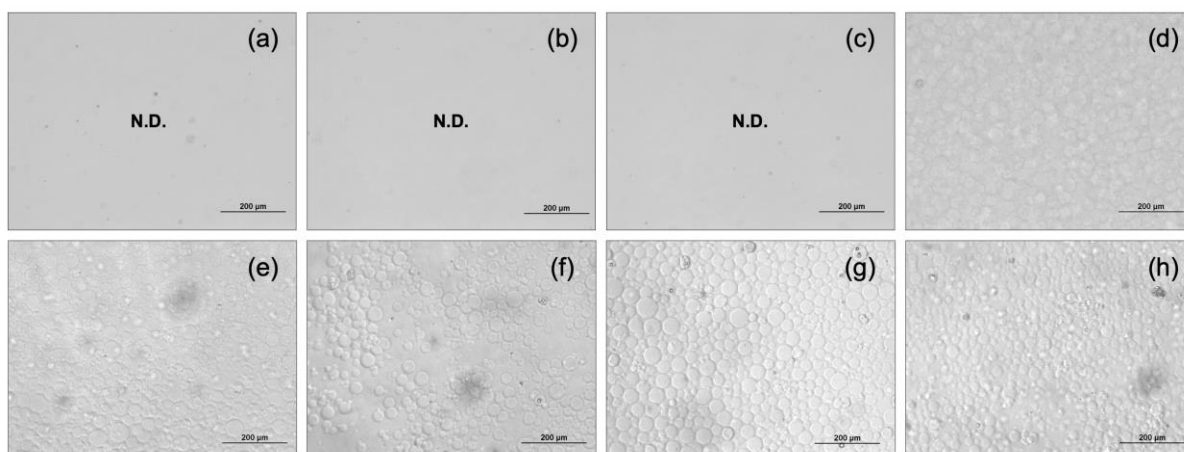


**Figure 35** Optical micrographs of alginate particles prepared via emulsification method by 2%(w/w) sodium alginate solution crosslinked with 0.1M Ca-EDTA from the acetic acid concentration of (a) 0 %(v/v), (b) 0.005%(v/v), (c) 0.01%(v/v), (d) 0.05%(v/v), (e) 0.1%(v/v), (f) 0.5%(v/v), (g) 1%(v/v), and (h) 2%(v/v).

## 5.2 Emulsification/internal gelation

The alginate particles were prepared by the emulsification gelation method. First, the water-soluble calcium complex was dissolved in an alginate solution. Then, the water in oil emulsion was emulsified via the shear force of the high-speed homogenizer. Subsequently, acetic acid was added into the emulsion to the final concentration of 1%(v/v), which induced the release of  $\text{Ca}^{2+}$  from Ca-EDTA, while stirring at 400 rpm. The release of  $\text{Ca}^{2+}$  ions lead to crosslinking of the alginate polymer chains. The samples were collected by centrifugal force instead of the gravity force to reduce the coalescence of the particles at the interface between oil and water phase.

### 5.2.1 Effect of emulsification speed

The effect of emulsification speed was studied in 2%(w/w) sodium alginate with 0.1M Ca-EDTA in MCT oil. The sodium alginate with Ca-EDTA solution in MCT oil was emulsified at 400 rpm of the magnetic stirrer and at 5,000, 7,500 and 10,000 rpm of the high-speed homogenizer for 5 min. Figure 36(a) shows the optical image of alginate particles. Their size varied from 300 to 800  $\mu\text{m}$  when the magnetic stirrer at 400 rpm was used. The size of alginate particles was further reduced to  $39.97 \pm 11.51 \mu\text{m}$  when the high-speed homogenizer at 5,000 rpm was used (Figure 36(b)) due to the higher shear force reducing the emulsion droplet. The average particle size of alginate was  $42.26 \pm 11.46$  and  $52.70 \pm 17.96 \mu\text{m}$  at a high-speed homogenizer of 7,500 and 10,000 rpm, respectively. However, at the shear force higher than 5,000 rpm no size reduction of alginate particles was found (Figure 36(c) and 36(d)). In general, the high-speed homogenizer produced smaller particles because more energy was provided for dispersion. However, the size of alginate particles using internal gelation was not inversely proportional with energy input when the agitation was over 5,000 rpm. In addition, the oil droplets in alginate particles were indicated due to the chaotic mixing through mechanical stirrer. However, the average particles agreed with the work by Ahmed et al., 2013 when used the magnetic stirrer, which studied the stirrer speed from 200, 400 and 600 rpm in internal gelation of  $\text{CaCO}_3$ . They found that the stirring speed was the most important parameter to control the particle size. The particles were reduced to average size of 100 to 160  $\mu\text{m}$  when the high stirring speed of 600 rpm was used [139]. The alginate particles of  $103.2 \pm 3.5$  was obtained at speed of 800 rpm [140]. M. Alnaief et al., 2011 used a higher stirrer speed of 1,400 rpm to decrease the alginate particles size to  $75 \pm 10 \mu\text{m}$  [141]. However, in this work, the smaller alginate particles without oil droplets were produced by using high-speed homogenizer at 5,000 rpm. So, this speed was set to consider other parameters in next chapter.

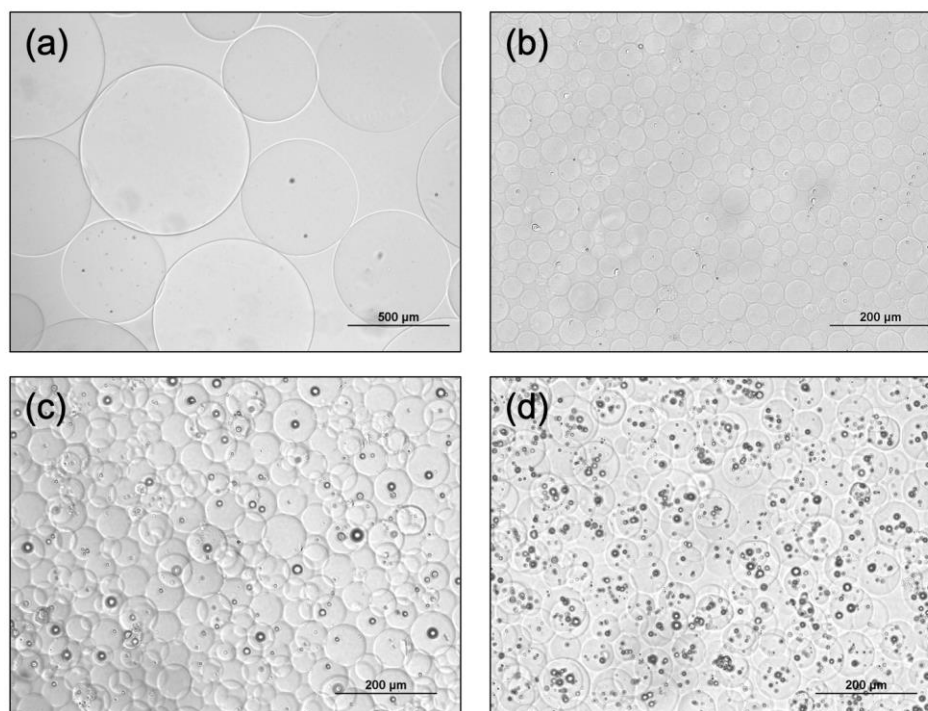


**Figure 36** Optical images of alginate beads from samples stirred with (a) a magnetic stirrer at 400 rpm; a high-speed homogenizer at (b) 5,000 rpm; (c) 7,500 rpm; and (d) 10,000 rpm.

### 5.2.2 Effect of Ca-EDTA concentration

The water in oil emulsion was prepared by using MCT oil as the medium phase. The 0.1, 0.2, 0.3, and 0.5M of Ca-EDTA mixed with 2%(w/w) sodium alginate solution were studied (Figure 37). The crosslinking time was fixed at 5 min at a magnetic stirrer speed of 400 rpm. The isolated particles were found when the Ca-EDTA concentration of 0.1M was used (Figure 37a). A higher concentration of Ca-EDTA increased the aggregate particle formation due to the higher divalent ions to crosslink with alginate chains. Higher concentrations of Ca-EDTA lead to increased aggregation of particles. Particles at 0.2M of Ca-EDTA were partially lumped together, as presented in Figure 37(b). Finally, the particles were strongly agglomerated at 0.3 and 0.5M of Ca-EDTA (Figure 37(c) and (d)). The high  $\text{Ca}^{2+}$  content tends to coagulate the aggregate particles before proper gelation.

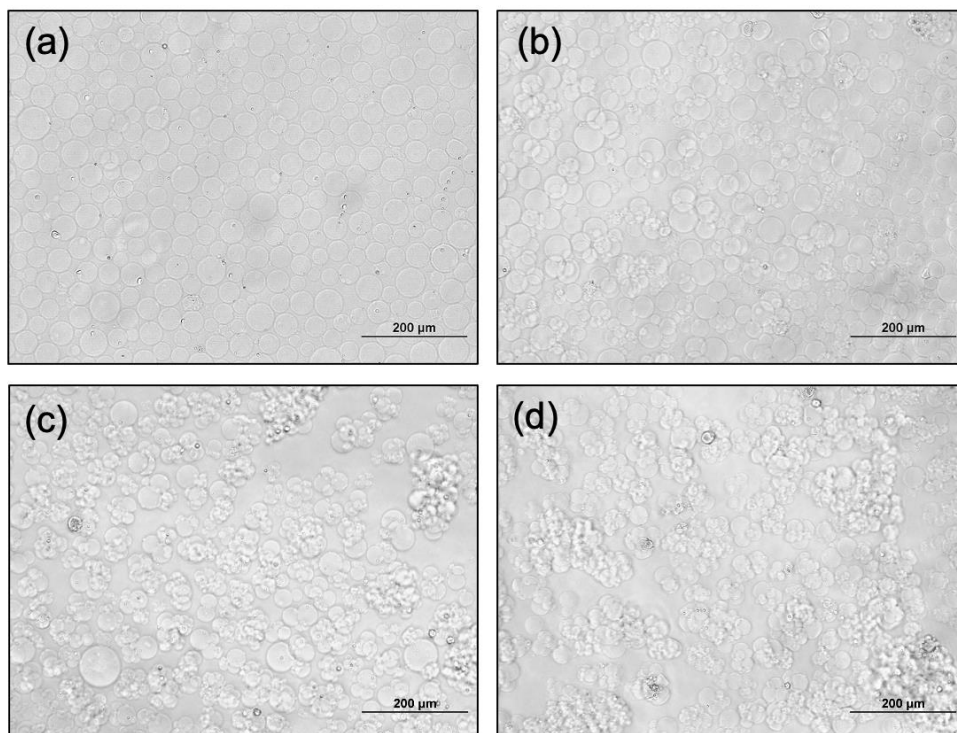


**Figure 37** Optical micrographs of alginate particles prepared by 2%(w/w) sodium alginate solution with (a) 0.1M (b) 0.2M (c) 0.3M and (d) 0.5M of Ca-EDTA.

The crosslink density of internal alginate particles was investigated through the mechanical and rheological properties. The effect of changing Ca-EDTA concentration on surface morphology was investigated by AFM measurement. AFM height images (recorded in QI™ mode) for Ca-EDTA concentration from 0.1M, 0.2M, 0.3M, and 0.5M are shown in Figure 38(a)-(d), respectively. The average size of surface structures, which may be correlated with the pore size network decreased with increasing Ca-EDTA concentration. At the same time, the increase of Ca-EDTA concentration led to lower surface roughness with calculated roughness values of  $R_a = 157 \pm 28$  nm for 0.1M,  $R_a = 100 \pm 22$  nm for 0.2M,  $R_a = 85 \pm 8$  nm for 0.3M, and  $66 \pm 23$  nm for 0.5M, respectively. As the images were recorded in QI™ mode, a force vs. distance curve was taken in every pixel of each image. The AFM manufacturer software was used to fit all the force-distance curves using a Sneddon model for indentation with a pyramidal tip, to obtain an



apparent Young's modulus ( $E_{app}$ ). As the mechanical response of the alginate particles in indentation is not fully elastic, the modulus obtained by this fit procedure cannot be taken as Young's modulus and we therefore call it apparent Young's modulus. Increasing Ca-EDTA concentration increased  $E_{app}$ . The  $E_{app}$  values were calculated as averages of all pixels from 5 images recorded for different particles. The  $E_{app}$  of  $3.4 \pm 0.5$  kPa,  $31.0 \pm 2.3$  kPa, and  $111 \pm 24$  kPa were obtained for 0.1M, 0.2M, and 0.3M Ca-EDTA concentration, respectively. At 0.5M Ca-EDTA, we observed large variation of  $E_{app}$ , with an average  $E_{app}$  of  $74 \pm 30$  kPa for isolated particles and values of up to 2.2 MPa for particle agglomerates. Although the higher  $E_{app}$  showed a higher crosslink density, the large distribution of  $E_{app}$  was gained due to the aggregated particles at 0.3M (Figure 37(c)) and 0.5M (Figure 37(d)) Ca-EDTA concentration.

The mechanical properties of alginate particles were also investigated through rheological measurements. The experiments were carried out in both strain and frequency sweep mode. Storage modulus ( $G'$ ) and loss modulus ( $G''$ ) represent the elasticity and viscosity of the materials, respectively. Figure 39(a) presents the strain dependence at the frequency of 1 Hz of the  $G'$ ,  $G''$ , and phase angle delta, for internal gelation of alginate particle at Ca-EDTA concentration of 0.1M.  $G'$  was constant from %strain of 0.1 to 90 and decreased after 100 %. At low strain amplitude,  $G'$  was independent of strain amplitude, which showed that the particle structure was entirely reversible. The results represented that the deformation of particles could occur at high strain (over 100 %strain). It can be noted that, under the strain of 90%, the deformation of the network structure was completely reversible. However, over 90% of strain, the deformation was no longer reversible. All samples showed the same results, which indicated all these samples behaved like viscoelastic materials at high strain. The rotational speed dependence of  $G'$  and  $G''$  was plotted at various Ca-EDTA concentrations (Figure 39(b)). All samples revealed larger  $G'$  than  $G''$ , which indicated that these samples showed elastic behavior predominated over their viscous behavior for lower strain and all frequencies studied. Increasing Ca-EDTA concentration increased the  $G'$  at all frequency up to 100 Hz while  $G''$  was hardly influenced, which

showed an increase in rigidity of the material. An increase in Ca-EDTA resulted in higher stiffness because higher concentration of  $\text{Ca}^{2+}$  allowed more rapid ion diffusion. This encouraged the formation of alginate matrix and generated a dense and rigid structure of alginate particles. This agrees with a previous study which used  $\text{Ca}^{2+}$  from carbonate source [142, 143].

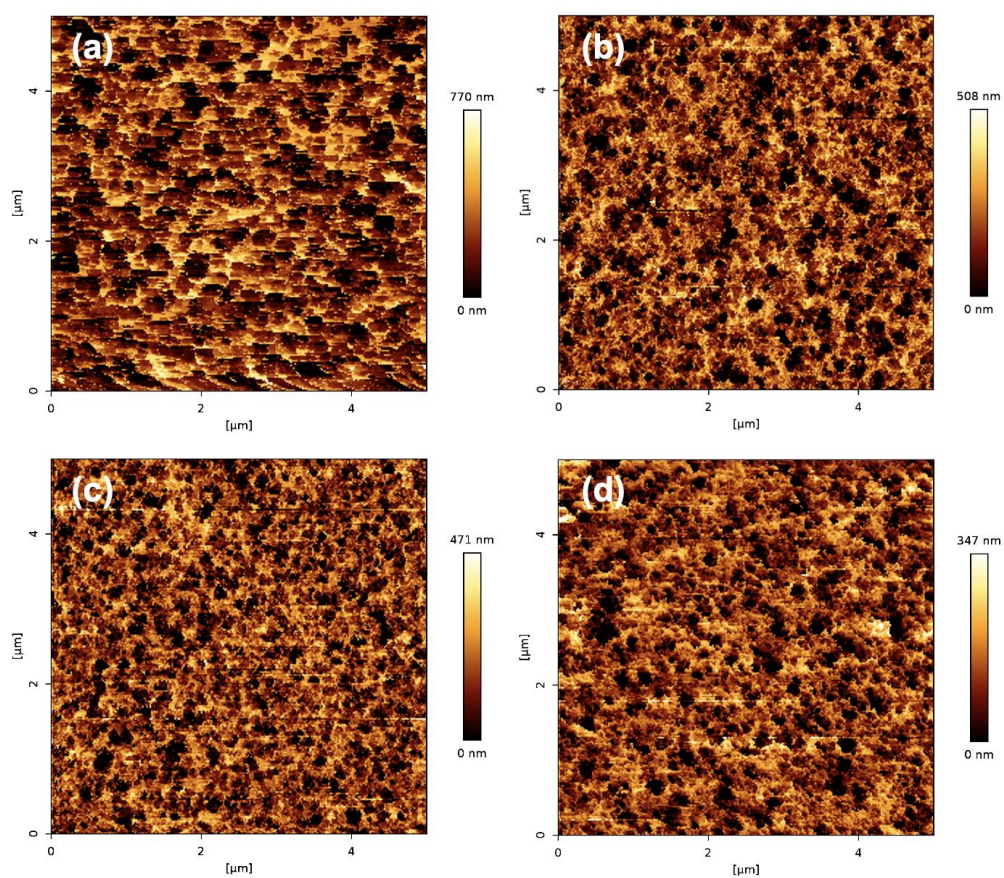


**Figure 38** AFM height images of alginate particles prepared by 2% (w/w) sodium alginate solution with (a) 0.1 M (b) 0.2 M (c) 0.3 M and (d) 0.5 M of Ca-EDTA.

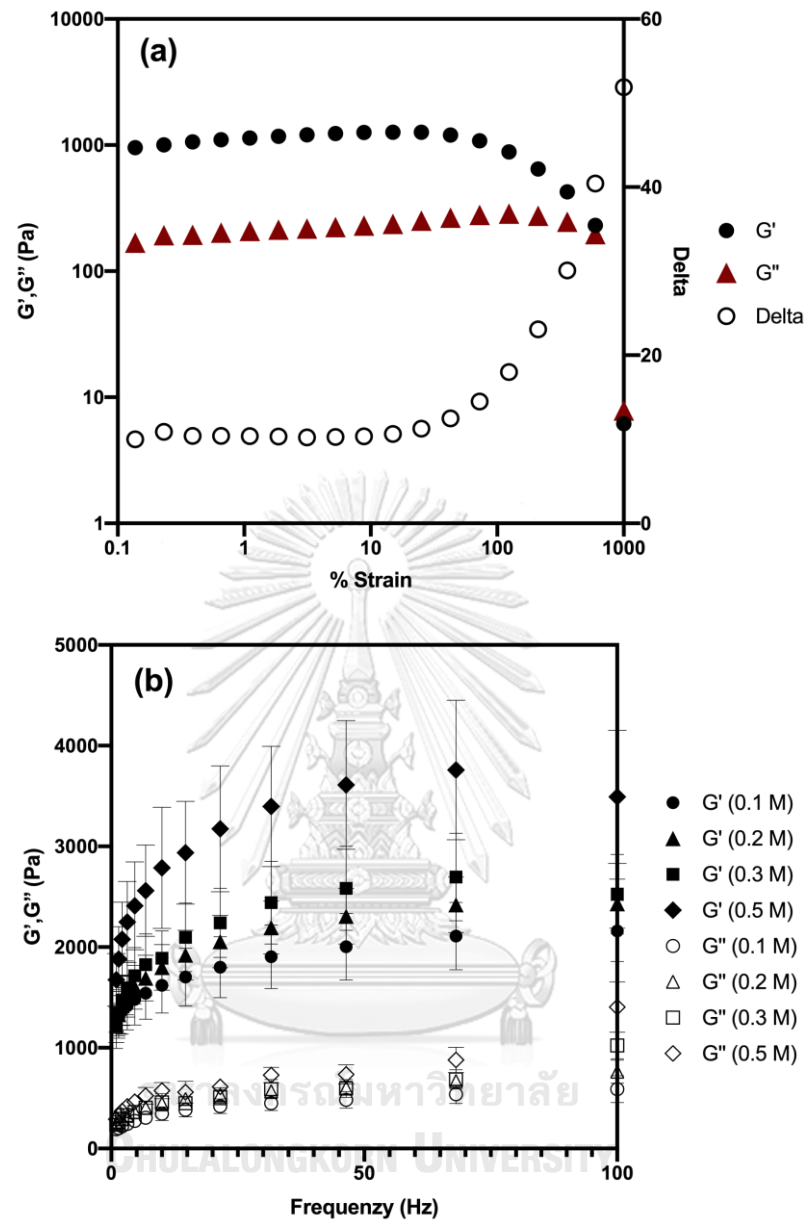


Figure 39 Rheological characterization of internal gelation of 2%(w/w) alginate particles

(a) strain dependence when Ca-EDTA of 0.1M

(b) frequency dependence at different concentration of Ca-EDTA.

### 5.2.3 Effect of crosslinking time

Internal gelation of alginate with Ca-EDTA particles were prepared. After collected samples and redispersed with water, the alginate particles were air-dried on filter paper for 24 h at room temperature. %Yield was carried out via the ratio of dry weight of the alginate particles ( $W_p$ ) and initial weight ( $W_i$ ). The %yield of internal gelation of 2%(w/w) alginate particles crosslinked with 0.1M Ca-EDTA was studied at the optimum concentration in different crosslinking times. %Yield of  $76.62 \pm 1.23$ ,  $75.75 \pm 2.47$ ,  $74.13 \pm 1.05$ , and  $66.46 \pm 3.29$  was obtained for crosslinking time of 1, 3, 5, and 10 min, respectively. The results showed that the %yield tended to decrease with increasing crosslinking time. High crosslinking time caused particles to lump together around the beaker rim due to the aggregation of crosslinked particles. This could be explained by the expansion of crosslinking reaction between  $\text{Ca}^{2+}$  and the  $\text{COO}^-$  of alginate chains as the crosslink time increased. The crosslinking time did not significantly influence on the morphology but more on rheological properties. The frequency dependence of internal gelation of 2%(w/w) alginate particles crosslinked with 0.1M Ca-EDTA at different crosslinking time is shown in Figure 40. The  $G''$  had almost the same value from crosslinking time from 1 to 10 min while  $G'$  increased with increasing crosslinking time from 1 to 5 min, then decreased at the crosslinking time of 10 min. As mentioned earlier, a larger shear modulus indicated denser particles. The highest shear modulus appeared at crosslinking time of 5 min, which meant the most rigid particles were generated at that time. From the results, the optimum crosslinking time was 5 min when the alginate particles had the most rigid structure and still got a high %yield. The optimum crosslinking time was significantly lower than that of alginate beads prepared via external gelation with the optimum crosslinking time of 110 min [144]. The lower time needed might be due to the preparation method and the size of alginate particles.

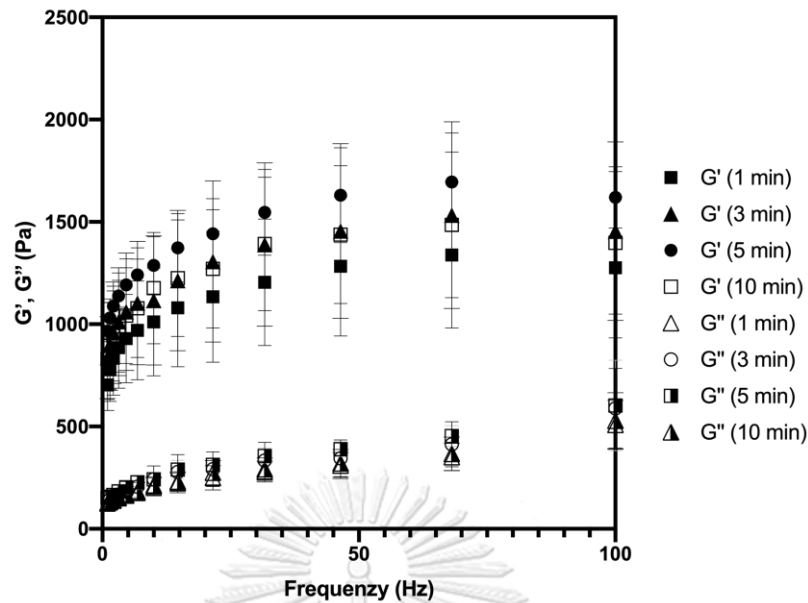
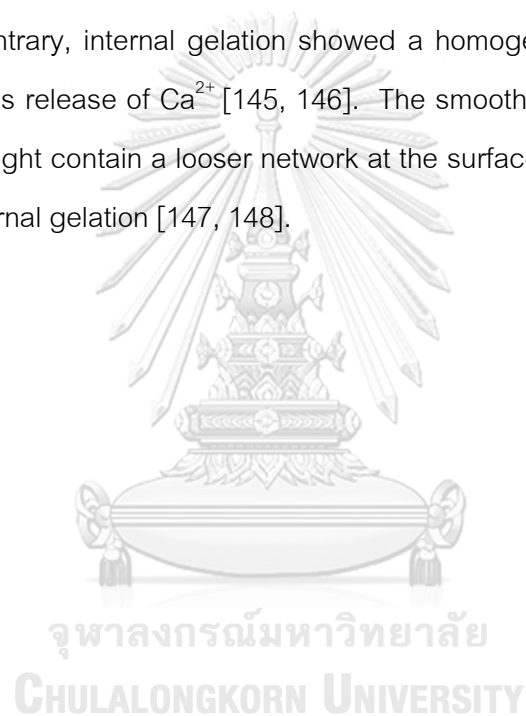


Figure 40 Effect of crosslinking time on frequency dependence of  $G'$  and  $G''$  of 2%(w/w) alginate particle crosslinked with 0.1M Ca-EDTA at different crosslinking time.

#### 5.2.4 Internal and external crosslink

The dripping method has been widely used due to the simple equipment required for bead production. Although the size of the beads depended on the nozzle, most of the beads produced had the size in millimeter scale. SEM was used to investigate the physical morphology and surface structure of alginate beads and particles. Figure 41(A1-D1) displays the SEM images at the original magnification of 75k from dripping method, which indicated that the original alginate beads had the average size of 2 mm. All beads were air-dried for overnight and coated with gold using a sputter coater. After drying, the beads reduced to average size of 500  $\mu\text{m}$ . The surface morphology of all beads was examined at magnification of 10,000x to show more details, as shown in Figure 41(A2-D2). The beads of 2%(w/w) sodium alginate with 0.1M of Ca-EDTA were dripped in MCT oil containing 1%(v/v) acetic acid with the crosslinking time of 5 min. The morphology of this internal gelation bead was shown in Figure 41(A1) illustrating a smooth and clear surface feature as shown in Figure 41(A2) due to the crosslinks interacted from the internal. Compared with the bead generated from the

external gelation, which used 2%(w/w) alginate solution dripped to 0.037M  $\text{CaCl}_2$  solution, a rough of surface morphology was indicated in Figure 41(B1) and (B2). The roughness was caused from the rapid crosslinking of  $\text{Ca}^{2+}$  from  $\text{CaCl}_2$  at the interface. Increasing of  $\text{CaCl}_2$  concentration to 0.074M and 0.185M increased the roughness at the surface of the beads as presented in Figure 41(C1) and (D1), respectively. The surface morphology of beads was obviously craggy as shown in Figure 41(C2) and (D2) because the crosslinks of external gelation started at periphery of the bead which exhibited inhomogeneous structure.  $\text{Ca}^{2+}$  was also higher at the surface than in the center. On the contrary, internal gelation showed a homogeneous structure due to its more homogeneous release of  $\text{Ca}^{2+}$  [145, 146]. The smooth surface morphology of the internal gelation might contain a looser network at the surface than that under the rough surface of the external gelation [147, 148].



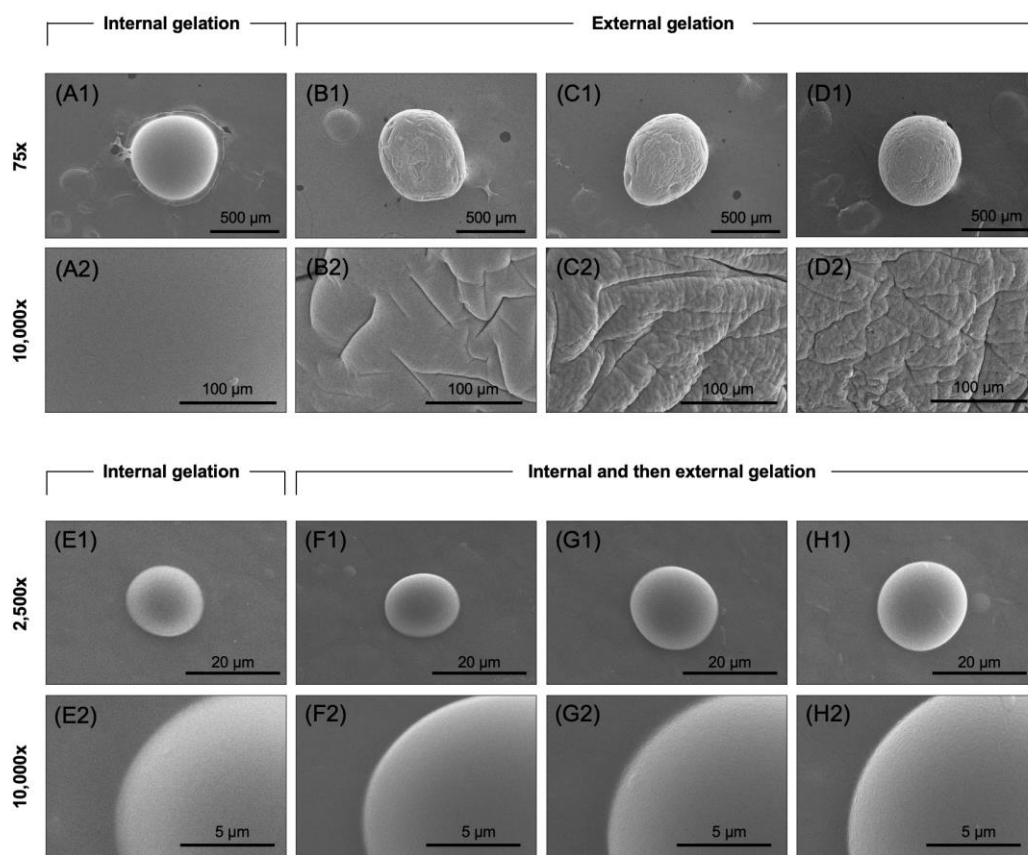


**Figure 41** SEM image of (A)-(D) alginate beads which (A1),(A2) internal gelation of Ca-EDTA of 0.1M; (B1),(B2) external gelation at 0.037M, (C1),(C2) 0.074M, and (D1),(D2) 0.185M of CaCl<sub>2</sub>; alginate particles which (E1),(E2) internal gelation of 0.1M Ca-EDTA; (F)-(H) internal gelation of 0.1M Ca-EDTA and, then external gelation at (F1),(F2) 0.037M, (G1),(G2) 0.074M, and (H1),(H2) 0.185M of CaCl<sub>2</sub>.

The internal gelation via emulsification method reduced the alginate particles size to  $39.97 \pm 11.51 \mu\text{m}$  when using 5,000 rpm speed of the homogenizer. The 2%(w/w) sodium alginate which internal crosslink with 0.1M Ca-EDTA showed the least aggregation between the particles was used as the control particles. The morphology was investigated by SEM as shown in Figure 41(E1). The smooth and clear surface morphology (Figure 41(E2)) also found even if the different size of particles was prepared. Figure 41(F1-H1) show morphologies of the internal gelation, which prepared first at the above conditions followed by an external gelation with different concentration



of  $\text{CaCl}_2$  solution for 60 min and washed with water. The control particles dispersed in water were used at 1:1 ratio with  $\text{CaCl}_2$  solution at 0.037M, 0.074M and 0.185M. The particles displayed edges more clearly with increasing  $\text{CaCl}_2$  concentration. The roughness on the surface of particles was apparent when using  $\text{CaCl}_2$  at 0.074M (Figure 41(G2)) and 0.185M (Figure 41(H2)).

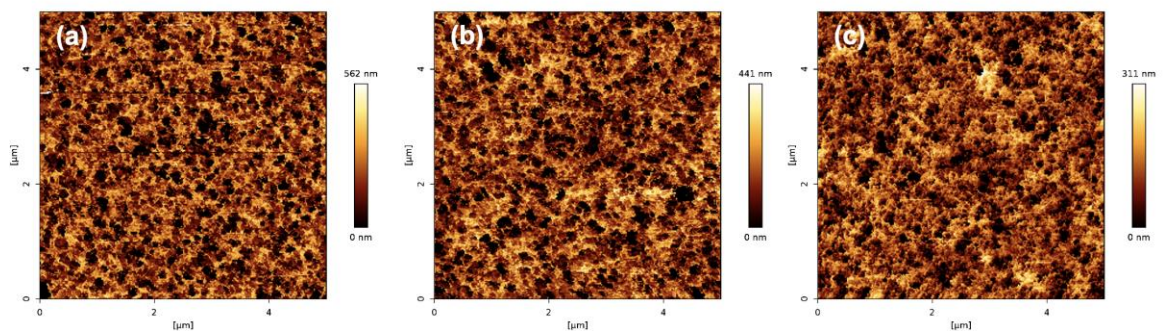


**Figure 42** AFM height images of internal gelation of 2%(w/w) alginate particles crosslinked with 0.1M Ca-EDTA and then external gelation with  $\text{CaCl}_2$  at (a) 0.037M (b) 0.074M and (c) 0.185M.

Although the surface morphology from SEM was not significant, the AFM height image showed a drastically different. Figure 42 presents the AFM height images of internal gelation of 2%(w/w) alginate particles crosslinked with 0.1M Ca-EDTA and then external gelation with  $\text{CaCl}_2$  at different concentration. Compared to only internal gelation with 0.1M Ca-EDTA (Figure 38(a)), the pore size of crosslinking network decreased when had an external crosslink with  $\text{CaCl}_2$  (Figure 43(a-c)). The mean roughness values of  $R_a = 156.74 \pm 28.25$  nm for only internal gelation with 0.1M Ca-EDTA and decrease to  $101.31 \pm 10.62$  nm for internal and then external gelation with 0.037M  $\text{CaCl}_2$ ,  $83.63 \pm 6.84$  nm for 0.074M  $\text{CaCl}_2$ , and  $63.10 \pm 6.10$  nm for 0.185M  $\text{CaCl}_2$  were obtained. The  $E_{app}$  also increased with an increasing of calcium concentration for double gelation. The internal gelation with 0.1M Ca-EDTA had the  $E_{app}$  of  $3.4 \pm 0.5$  kPa as mentioned earlier. The  $E_{app}$  increased to  $53 \pm 10$  kPa for external gelation with 0.037M



CaCl<sub>2</sub>, 66 ± 15 kPa for 0.074M CaCl<sub>2</sub>, and 75 ± 24 kPa for 0.185M CaCl<sub>2</sub>. The results indicated the high crosslink density was obtained by increasing calcium concentration.

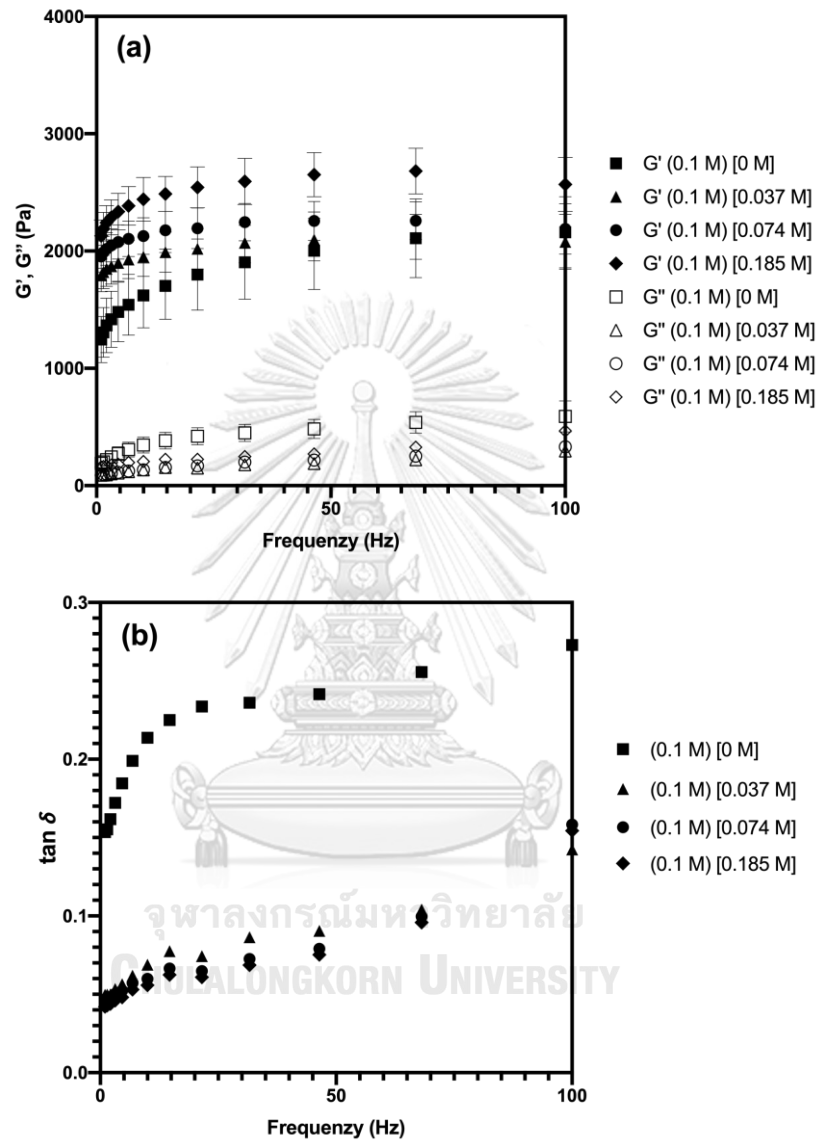
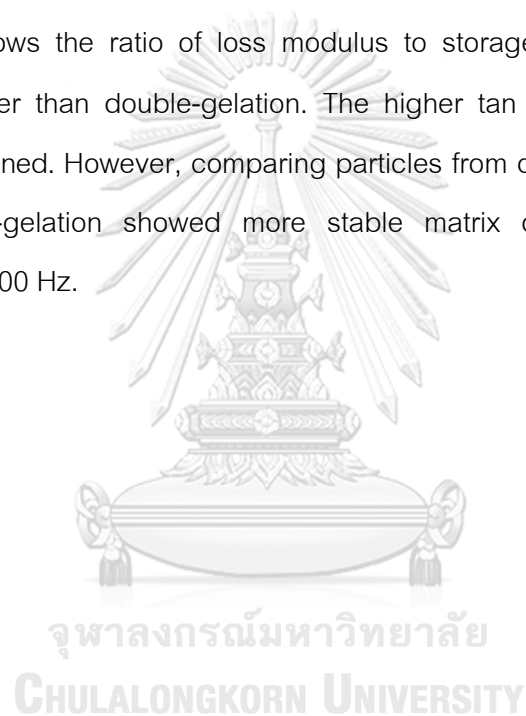


Figure 43 (a) Frequency dependence of  $G'$  and  $G''$  and (b)  $\tan \delta$  of internal gelation of 2%(w/w) alginate particles crosslinked with 0.1M Ca-EDTA and then external gelation with CaCl<sub>2</sub> at different concentration ; Legends refer to (Ca-EDTA concentration) [CaCl<sub>2</sub> concentration].

The rheological properties show in Figure 43. Compared to internal and then external gelation by  $\text{CaCl}_2$  solution, only internal gelation indicated the lower  $G'$  and higher  $G''$  which shows fewer rigid particles were obtained (Figure 43(a)). However, compared in only double-gelation, the  $G'$  was higher at all frequency when increasing of  $\text{CaCl}_2$  concentration while  $G''$  was quite constant. The double-gelation via external gelation after internal gelation enhanced the surface strength of the internal particles. The particles were more rigid because of the increase of  $\text{Ca}^{2+}$ , which promoted the formation of alginate matrix. The results point out in Figure 43(b) that the loss tangent ( $\tan \delta$ ) which shows the ratio of loss modulus to storage modulus of only internal gelation was higher than double-gelation. The higher  $\tan \delta$  indicated that the softer particles were obtained. However, comparing particles from only internal gelation, the  $G'$  profile of double-gelation showed more stable matrix of alginate particles from frequency of 1 to 100 Hz.



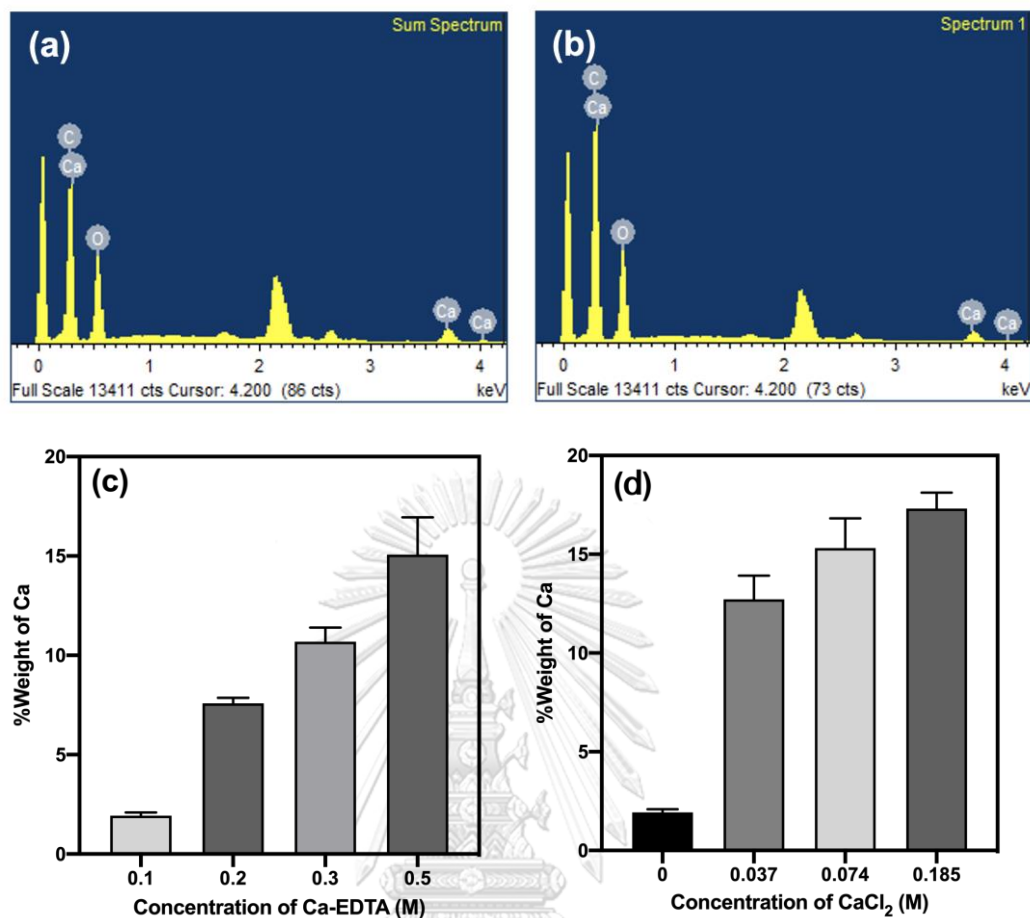


Figure 44 EDX analysis of (a) internal gelation of 2%(w/w) alginate particles crosslinked with 0.1M Ca-EDTA (b) 2%(w/w) alginate particles crosslinked with 0.1M Ca-EDTA and then external gelation with 0.185M CaCl<sub>2</sub>, and %Weight of Ca on (c) internal gelation of alginate particles prepared by 2%(w/w) sodium alginate solution at different Ca-EDTA concentration (d) the 2%(w/w) sodium alginate which internal crosslink with 0.1M Ca-EDTA and then external gelation at different concentration of CaCl<sub>2</sub>

The alginate particles were analyzed to determine calcium distribution by Field Emission Scanning Electron Microscope (FE-SEM) equipped with an Energy Dispersive X-Ray Spectrometer (EDX). EDX analysis in the point mode confirmed that the alginate particles contained calcium as shown in Figure 44(a) and (b). The results of %Ca were identified from calcium, carbon, and oxygen content. The peak of gold was not considered because it was from the coating layer of the samples. The %weight of Ca on

alginate particles prepared via internal gelation by 2%(w/w) sodium alginate solution at different Ca-EDTA concentrations was displayed in Figure 44(c). Figure 44(d) shows %weight of Ca of the 2%(w/w) sodium alginate which internal crosslink with 0.1M Ca-EDTA and then external gelation at different concentrations of  $\text{CaCl}_2$ . An increase of Ca-EDTA or  $\text{CaCl}_2$  concentration increased the %weight of Ca of particles due to the increased number of  $\text{Ca}^{2+}$ . The results agreed with the mechanical and rheological properties as mentioned earlier because increasing crosslinking agent increased the strength of particles due to the denser crosslinking network.

### 5.3 Microfluidic/internal gelation

The microfluidic technique has attracted attention in droplet production because of controllable droplets production. Generally, alginate particles can be produced by emulsification of an alginate solution in an oil phase and then ionic crosslinking with divalent ions in a gelling bath. The reaction could form at the interface between oil and water phase. Drawbacks of the technique included the irregular shape of particles, the clogging in the channel, and the crosslinking network at the interface while particle collecting [149, 150]. To solve these problems, the internal gelation, which  $\text{Ca}^{2+}$  could not interact with the alginate chain, was investigated.

Microfluidics mainly composed of two streams, continuous phase, and dispersed phase. The alginate particles which created from water in oil phase emulsion was generated by using 2%(w/w) sodium alginate solution with 0.1M Ca-EDTA as a dispersed phase whereas MCT oil with 1%(v/v) acetic acid was used as the continuous phase. The optimum condition of crosslinking was obtained from emulsification/internal gelation in previous study. The flow rate of each phase was control in a range of narrowing jet and tip streaming regime since the high yield of monodispersed droplets were obtained [90, 108, 151]. Droplets were collected by MCT oil which was stirring. After droplet collecting, the sample was washed with water as well as emulsification method. Alginate particles, which use Ca-EDTA of 0.1, 0.2, 0.2 and 0.5M, were successfully prepared as shown in Figure 45. A higher concentration of Ca-EDTA

tended to create aggregate particles due to the higher  $\text{Ca}^{2+}$  could interact with the alginate chain. The results were consistent with the emulsification method.

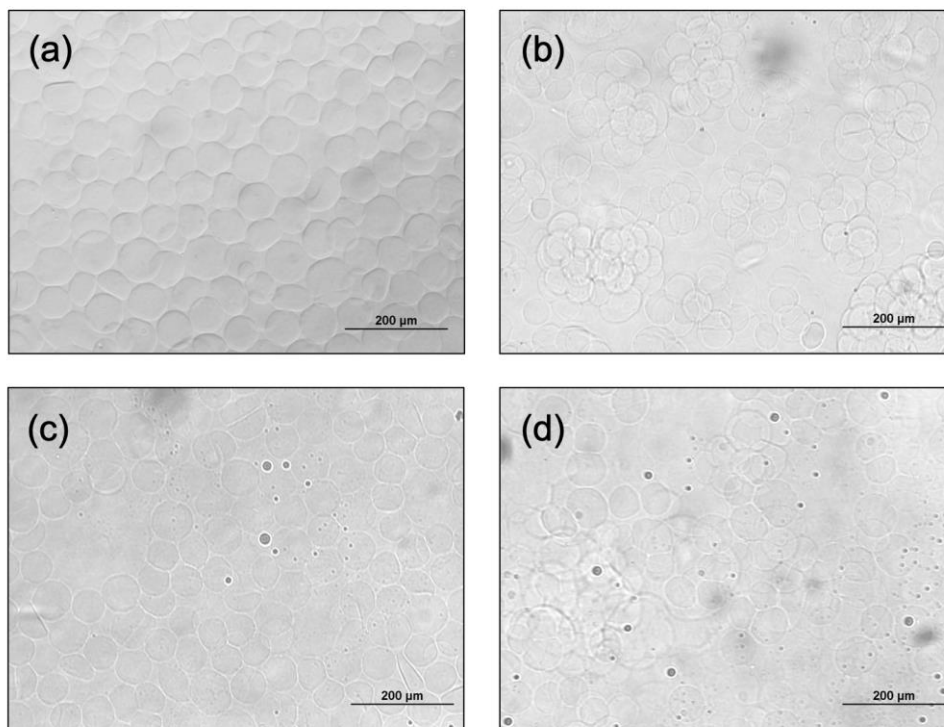


**Figure 45** Optical micrographs of alginate particles prepared via microfluidic method by 2%(w/w) sodium alginate solution with (a) 0.1M (b) 0.2M (c) 0.3M and (d) 0.5M of Ca-EDTA.

In narrowing jet and tip streaming regime, the particle size of alginate particles could control by both of fluid properties and operating condition. In case of keeping the fluid properties constant, the flow ratio which is the operating condition was the key factor. The experimental images of fluid characteristic in microfluidic channel at flow rate ratio ( $Q_c/Q_d$ ) 1.72, 2.09, and 2.50 was shown in Figure 46(a), (b), and (c), respectively. An increase in the flow rate ratio resulted in a decrease in droplet size. The high shear force was found at the high flow rate of the continuous phase, causing interruption of the dispersed phase to break up into smaller droplets. The W/O emulsion size of  $71.43 \pm$

6.66  $\mu\text{m}$  (Figure 46(d)),  $55.66 \pm 4.13 \mu\text{m}$  (Figure 46(e)), and  $41.64 \pm 3.25 \mu\text{m}$  (Figure 46(f)) were found at  $Q_c/Q_d$  1.72, 2.09, and 2.50, respectively. The result of the w/o emulsion size was agreed well with the predicted correlation of droplet size in narrowing jet and tip streaming regime in Eq. 6 [151].

The alginate particles form a complex matrix in which the spaces between polymeric chains could be filled with water molecules. So, the particle size of alginate particles in the water phase could increase. The alginate particles size could raise to  $107.71 \pm 8.47 \mu\text{m}$  (Figure 46(g)),  $70.48 \pm 4.22 \mu\text{m}$  (Figure 46(h)), and  $47.35 \pm 3.78 \mu\text{m}$  (Figure 46(i)) were found at  $Q_c/Q_d$  1.72, 2.09, and 2.50, respectively. The coefficient of variation (C.V.) from the microfluidic technique in both emulsion size and particles size were found to be below 10%. The results verified the monodispersity since the C.V. was smaller than 10%, which was the standard criterion for monodispersity [96-98] while the alginate particles from emulsification method showed the C.V. of 28.80%. Therefore, the microfluidic method could provide controllable particle sizes and monodispersed particles.

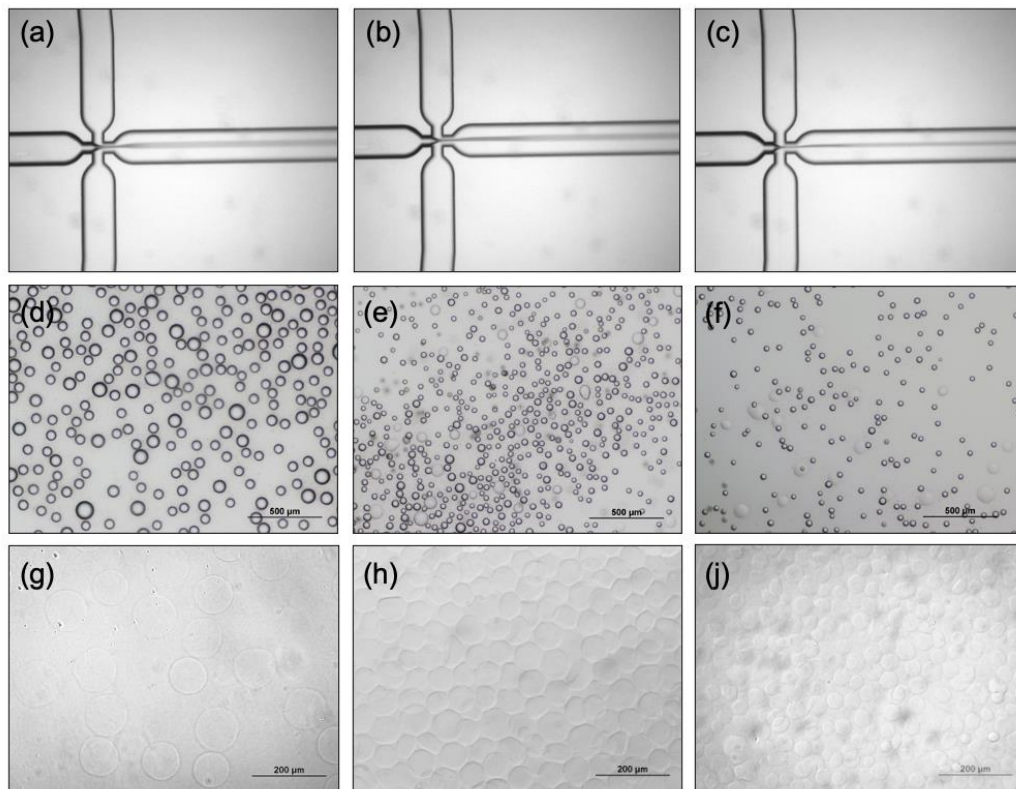


**Figure 46** Effect of operating condition in microfluidic method;  
 (a-c) experimental images of fluid characteristics in microfluidic channel,  
 and (d-f) micrograph of 2%(w/w) alginate droplet in MCT oil system  
 in a junction depth of 100  $\mu\text{m}$ .

(Flow rate ratio ( $Q_c/Q_d$ ) of (a,d) 1.72, (b,e) 2.09, and (c,f) 2.50)

CHULALONGKORN UNIVERSITY

## Chapter 6

### Fabrication of single- and multiplied-core-shell of alginate microcapsules via microfluidic flow-focusing

Core-shell microparticles are particles that are composed of two or more different material layers. One forms the inner core, and the others make the outer layer or shell. The composite material that has different characteristics and properties which not achievable by individual materials can combine into the core-shell structure. So, this type of structure has numerous potential for the development of encapsulation in many fields such as the food industry [152], agriculture [153], cosmetics [154, 155], and pharmaceuticals [156, 157]. Moreover, encapsulation of hydrophobic components that are water-insoluble has attracted increasing interest, since many active components are water-insoluble. Shell materials can be selected according to the particular application. The main purpose of the shell is to enhance the controlled release, protect chemically active components in the core against oxidative degradation, and increase biocompatibility. Alginate is well-known material due to its favorable properties, including biocompatibility, biodegradability, low toxicity, and low cost. This makes alginate one of the most suitable materials used as the shell in the design of encapsulation systems.

The alginate microcapsules which contain the oil phase inside offer excellent compartmentalized structures for encapsulation. The shell of microcapsules provides a matrix structure for protecting the components and controlling their release. Typically, the core-shell alginate microcapsules were produced by co-extrusion using vibration or electrostatic force [158, 159]. The limitation was the size of the particle. Two-stage emulsification process using an inverse gelation technique was also used [160, 161]. However, most of the oil used during process was not encapsulated and could not be recovered. Compared with microfluidic technique, emulsification method is associated with low batch-to-batch reproducibility, lack of precise control over process



parameters and high material and energy consumption. While the droplet size from microfluidic technique can be finely tuned by adjusting the flow rate of dispersed and continuous phase. The uniform droplet size could be obtained. Many glasses capillary microfluidic devices have fabricated to prepare double emulsion which is the template of core-shell microcapsules. The two round glass capillaries were inserted coaxially into the glass square tube was fabricated for preparation of core-shell droplets [61, 162, 163]. The device with two circular capillaries for injection and collection was also developed [164-166]. The glass capillaries device with a little difference in shape and surface modification were employed for production multiple emulsion drop [44, 165]. However, the limitation of capillary microfluidic is the production specificity. While the flow-focusing type is flexible and has a versatile process that allows for the generation of microemulsion with two, three, or even more cores. Liao et al. [167] used the two flow-focusing device to fabricate cell-laden calcium alginate microbead. Cells were firstly encapsulated in sodium alginate droplet, and then entrapped in oil droplet to form double emulsion. The water in oil in water (W/O/W) double emulsion strategy could help to improve their cell viability. The gas in water in oil (G/W/O) double emulsion also were studied in flow-focusing device [168]. The flow-focusing pattern was used to generate the porous polyacrylamide hydrogel microspheres in both single-core and multiple-core. Also, the high-order multiple emulsion could prepared in flow-focusing device [169].

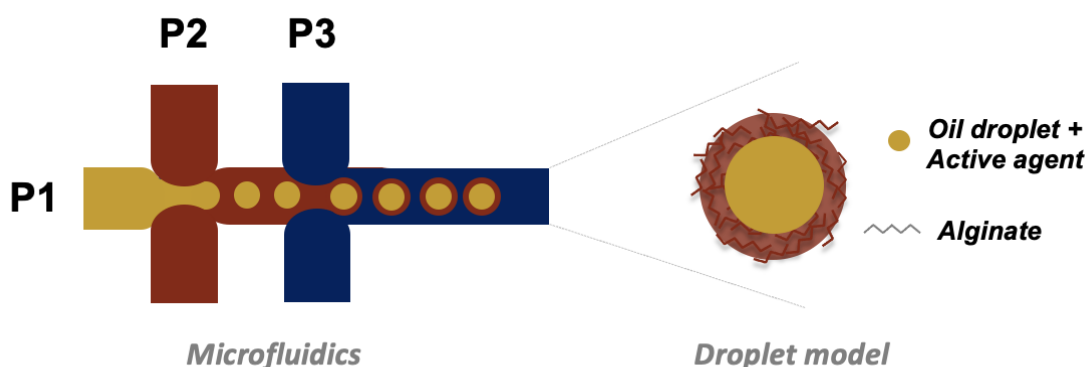


Figure 47 Schematic of core-shell microcapsule fabrication using microfluidic flow-focusing.

Thus, this chapter presents the fabrication of alginate microcapsules using microfluidic flow-focusing. Microcapsules were fabricated from continuously connected two flow-focusing microfluidic chips as shown in Figure 47. The core-shell microcapsules develop from oil in water in oil (O/W/O) double emulsions containing oil internals for encapsulating hydrophobic components. The first chip was hydrophilic coating with 100  $\mu\text{m}$  etch depth and the second chip size was hydrophobic with 190  $\mu\text{m}$  etch depth. The first chip would produce an O/W emulsion which has an oil phase as a dispersed phase and a water phase as a continuous phase. The oil phase could contain any active ingredient in the hydrophobic part which would be the core of the microcapsule. While the water phase (continuous phase) was an alginate solution and crosslinking agent of Ca-EDTA. The 2%(w/w) alginate solution with 0.1M Ca-EDTA was used. The product from the first chip would be dispersed phase of the second chip. The continuous phase was an oil phase in the second chip to produce O/W/O emulsion. Alginate microcapsules were fabricated in the second microfluidic chip via the internal gelation method. Firstly, acetic acid of 0.1%(v/v) which was added in the continuous phase diffused into the dispersed phase, leading to  $\text{Ca}^{2+}$  to be released from the Ca-EDTA complex. Then, the release  $\text{Ca}^{2+}$  was crosslinked with the alginate polymer to form calcium alginate hydrogel. This method could help maintain the morphology of the particles. The core-shell microcapsules which alginate as the shell and have an oil phase as the core was generated. In this experiment, alpha-mangostin was used as a model drug in an oil phase. The fluorescence dye of green from coumarin6 was used in the oil phase and red from rhodamine6G was used in the water phase for clear observation. The surfactant span<sup>®</sup>80 and tween<sup>®</sup>20 were added for stabilization in the oil phase and water phase, respectively. From now on, P1, P2, and P3 represent the dispersed phase and continuous phase of the first chip and the continuous phase of the second chip, respectively. Also, the  $Q_1$ ,  $Q_2$ , and  $Q_3$  represent the dispersed phase and continuous phase flow rate of the first microfluidic chip and the continuous phase flow rate of the second microfluidic chip, respectively.

### 6.1 Effect of flow rate on droplet regime

The effect of  $Q_1$ ,  $Q_2$ , and  $Q_3$  on transitions of droplet generation regimes have been investigated. The first chip would produce an O/W emulsion which has an oil phase as a dispersed phase and a water phase as a continuous phase. The oil phase contained alpha-mangostin as a model drug. While the water phase (continuous phase) was 2%(w/w) alginate solution and crosslinking agent of 0.1M Ca-EDTA. The transition between different regimes in the first microfluidic chip occurred by changing dispersed and/or continuous phase flow rates as shown in Figure 48. Five regimes of fluids were investigated at low flow rates ( $Q_1$  from 2.1 to 5.2  $\mu\text{l}/\text{min}$  and  $Q_2$  from 0.5 to 7.1  $\mu\text{l}/\text{min}$  at a constant  $Q_3$  of 1.2  $\mu\text{l}/\text{min}$ ). The co-flow was firstly observed. When the flow rate of the continuous phase was increased, the dispersed fluid was deformed to the squeezing regime. Then, the transition, the dripping, and the reverse regime were respectively found when the continuous phase flow rate was raised [151].

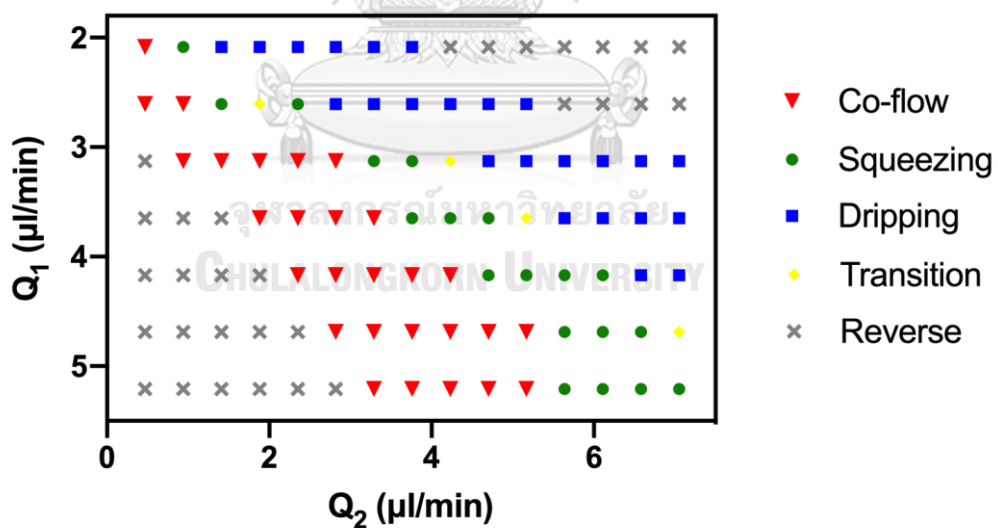


Figure 48 Flow regime of MCT oil in 2%(w/w) alginate droplets at various flow rate of dispersed phase ( $Q_1$ ) and continuous phase ( $Q_2$ ) in first chip (at constant  $Q_3$  of 1.2  $\mu\text{l}/\text{min}$ ).

As mentioned in chapter 4, monodisperse droplets could be produced in a squeezing and dripping regime at a low flow rate and narrowing jet and tip streaming at a high flow rate. So, core-shell microcapsules with uniform sizes could be created in these regimes. Figure 49 presents the flow regime in the first chip which produced O/W droplets at constant  $Q_1$  of 2.6  $\mu\text{l}/\text{min}$ . The results indicated that monodisperse O/W droplets would be generated at  $Q_2$  of 1.4 – 5.2  $\mu\text{l}/\text{min}$  which was the squeezing and dripping regime (Figure 49(a)). Then, the droplets in the second chip would be focused. The O/W emulsion from the first chip would be the dispersed phase of the second chip. The MCT oil was used as the continuous phase for the second chip. The flow regime of the second chip showed the same pattern (Figure 49(b)) as the first chip which transition between different occurred by changing dispersed and/or continuous phase flow rates. The co-flow has initially occurred in which O/W/O droplets could not generate in this regime (Figure 50(a)). When the flow rate of the continuous phase was increased, the dispersed fluid was deformed to the squeezing regime (Figure 50(b)). Figure 50(c) displays the squeezing-dripping transition which occurred due to an unstable force balance. Finally, the dripping regime which forms uniform particles was investigated (Figure 50(d)). However, at high flow rate (above the  $Ca_d$  of 0.031), the regime pattern was changed. The widening jet, narrowing jet, and tip streaming regimes were found instead of squeezing and dripping regime. The fluid thread ejected from the dispersed channel which was the widening jet regime (Figure 51(a)) and became polydisperse droplets due to Rayleigh-Plateau instability. The narrowing jet regime (Figure 51(b)) occurred when the viscous force of the continuous phase predominated over the capillary force. Then, a very thin jet was dragged and broken up into tiny and uniform droplets as in the tip streaming regime (Figure 51(c)). The regime pattern was consistent with the results in chapter 4.

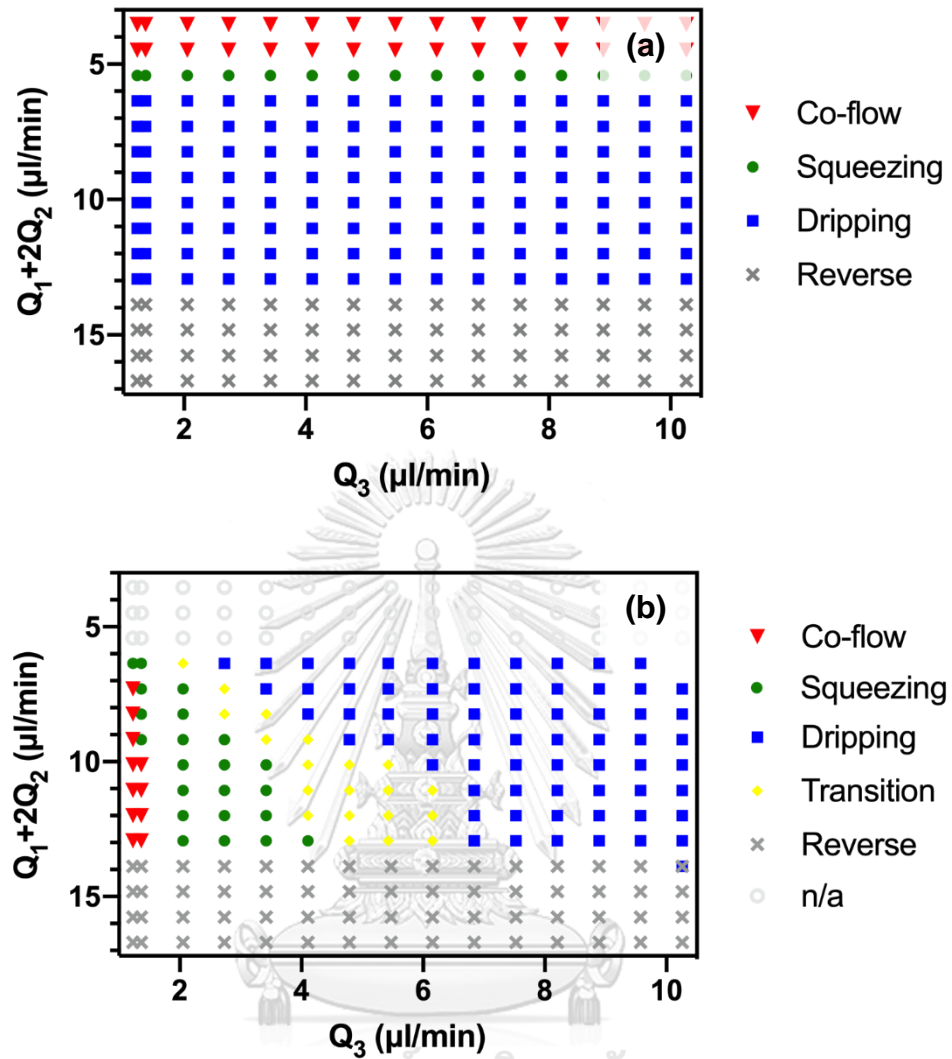
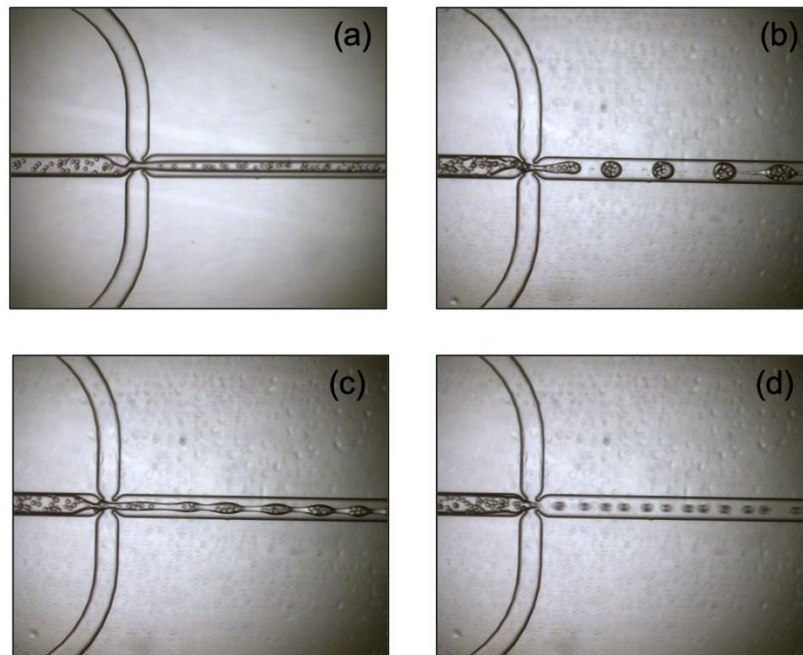
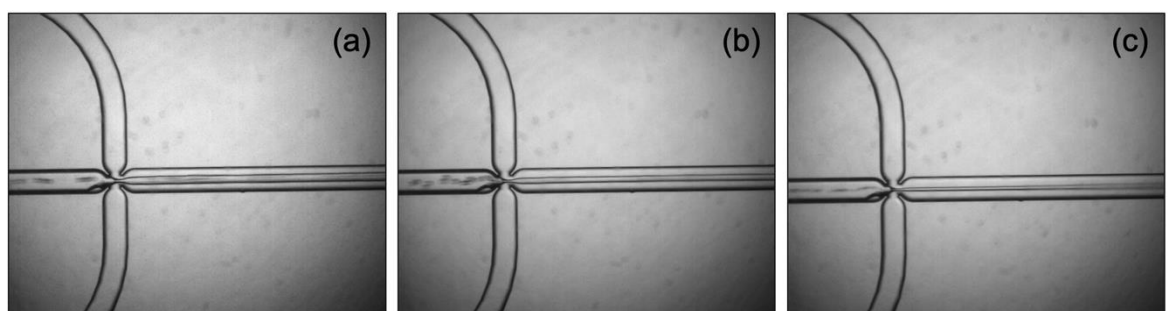


Figure 49 Flow regime of (a) O/W droplets in first chip and (b) O/W/O droplets in second chip at various flow rate (at constant  $Q_1$  of  $2.6 \mu\text{l}/\text{min}$ ).



**Figure 50** Experimental images of fluid characteristics in a microfluidic channel at different continuous phase flow rate of second chip ( $Q_3$ ) which (a)  $Q_3 = 1.2 \mu\text{l}/\text{min}$ ; co-flow, (b)  $Q_3 = 2.1 \mu\text{l}/\text{min}$ ; squeezing, (c)  $Q_3 = 4.1 \mu\text{l}/\text{min}$ ; transition, and (d)  $Q_3 = 6.2 \mu\text{l}/\text{min}$ ; dripping (at  $Q_1$  of  $2.6 \mu\text{l}/\text{min}$  and  $Q_2$  of  $3.3 \mu\text{l}/\text{min}$  in a junction depth of  $190 \mu\text{m}$ ).



**Figure 51** Experimental images of fluid characteristics in a microfluidic channel at different continuous phase flow rate of second chip ( $Q_3$ ) which (a)  $Q_3 = 17.6 \mu\text{l}/\text{min}$ ; widening jet, (b)  $Q_3 = 51.8 \mu\text{l}/\text{min}$ ; narrowing jet, and (c)  $Q_3 = 86.0 \mu\text{l}/\text{min}$ ; tip streaming (at  $Q_1$  of  $10.4 \mu\text{l}/\text{min}$  and  $Q_2$  of  $18.8 \mu\text{l}/\text{min}$  in a junction depth of  $190 \mu\text{m}$ ).

## 6.2 Effect of the dispersed phase flow rate of the first microfluidic chip ( $Q_1$ )

As mentioned earlier, under  $Ca_d$  of 0.031, the regimes which could produce monodisperse droplets were squeezing and dripping [151]. Therefore, microcapsules preparation under  $Ca_d$  of 0.031 would be focused on these two regimes. Effect of the dispersed phase flow rate of the first chip ( $Q_1$ ) when keeping  $Q_2$  at 3.3 and  $Q_3$  at 8.8  $\mu\text{l}/\text{min}$  is shown in Figure 52. Increasing  $Q_1$  which increased the O/W emulsion droplets due to the high dispersed phase flow rate resisted the shear force of the continuous phase. The fluid characteristic inside the channel is displayed in Figure 52(A1-E1). Figure 53 shows the results which indicated that the core size of the microcapsule increased with an increase in  $Q_1$ . However, at  $Q_1$  of 2.1  $\mu\text{l}/\text{min}$ , the dispersed phase flow rate of the second chip was too slow to create the droplet due to the slack flow rate in the first chip which shows the transition regime in Figure 52(A2). The irregular shape like bullet microcapsules was produced as shown in Figure 52(A3). The microcapsules were formed as singled-core-shell when  $Q_1$  of 2.6 to 3.6  $\mu\text{l}/\text{min}$  (Figure 52(B3-D3)) which was produced from the dripping regime in Figure 52(B2-D2). The shell size of microcapsules was nearly constant at 130 - 140  $\mu\text{m}$ . The thickness of singled-core-shell microcapsules was 59.10, 55.68, and 19.01  $\mu\text{m}$  at  $Q_1$  at 2.6, 3.1, and 3.6  $\mu\text{l}/\text{min}$ , respectively. However, when  $Q_1$  reached 4.2  $\mu\text{l}/\text{min}$ , the shell size was still constant while the core increased, and the smaller shell was unable to contain the bigger core. The core turned inside out from the shell as presented in Figure 52(E3).

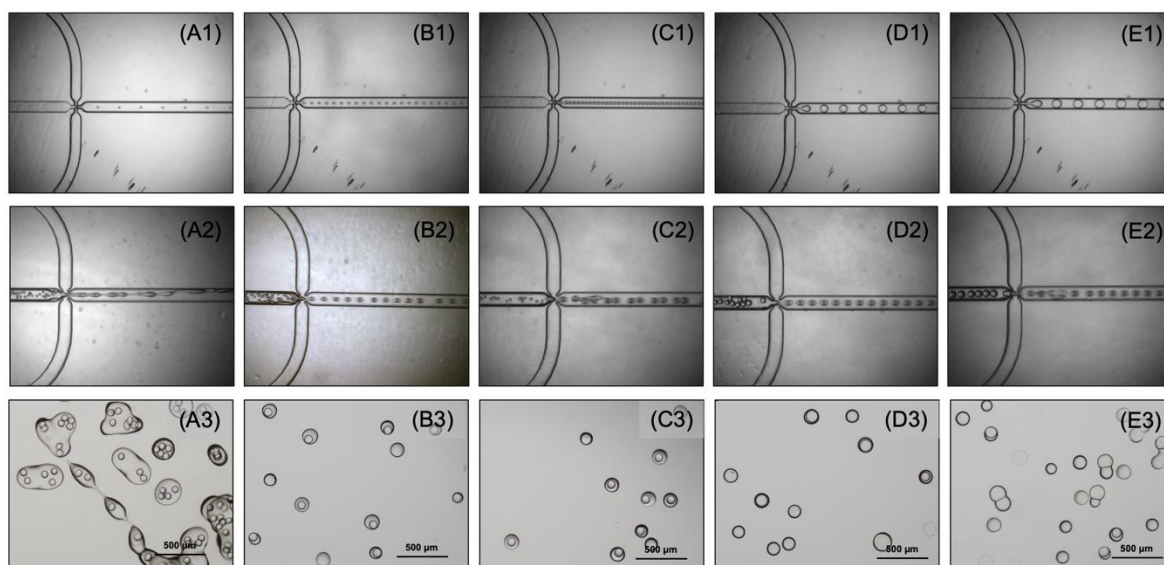


Figure 52 Experimental images of fluid characteristics in (A1-E1) the first microfluidic chip, (A2-E2) the second microfluidic chip, and (A3-E3) core-shell-microcapsules micrograph at constant  $Q_2$  of 3.3 and  $Q_3$  of 8.8  $\mu\text{l}/\text{min}$  which  $Q_1$  of (A1, A2, A3) 2.1  $\mu\text{l}/\text{min}$ , (B1, B2, B3) 2.6  $\mu\text{l}/\text{min}$ , (C1, C2, C3) 3.1  $\mu\text{l}/\text{min}$ , (D1, D2, D3) 3.6  $\mu\text{l}/\text{min}$ , and (E1, E2, E3) 4.2  $\mu\text{l}/\text{min}$ .

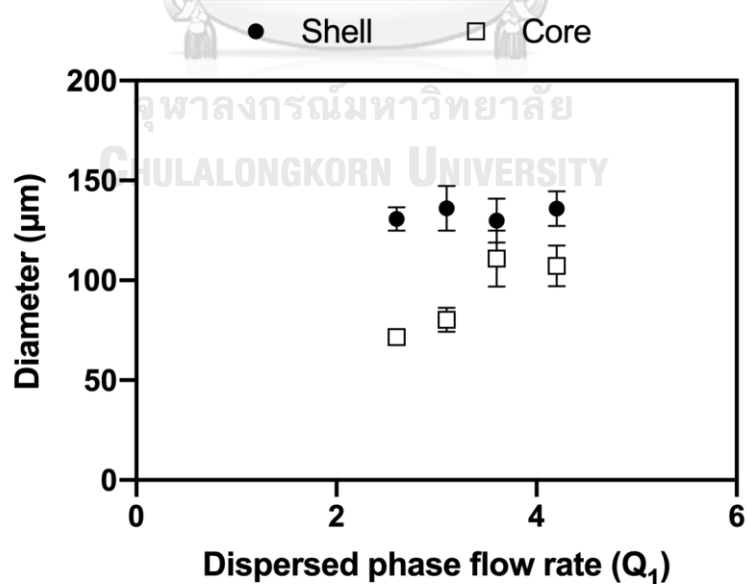


Figure 53 Effect of the dispersed flow rate of the first microfluidic chip ( $Q_1$ ) on core and shell diameter of microcapsules at constant  $Q_2$  of 3.3 and  $Q_3$  of 8.8  $\mu\text{l}/\text{min}$ .



Above the  $Ca_d$  of 0.031, the narrowing jet and tip streaming would be focused instead of a squeezing and dripping regime due to the potential of tiny and monodisperse droplets producing. The effect of  $Q_1$  was studied when keeping  $Q_2$  and  $Q_3$  constant at 3.3 and 8.8  $\mu\text{l}/\text{min}$ , respectively. The too low dispersed phase flow rate was the cause of the reverse regime (Figure 54(A1)). Microcapsules could not be produced at this stage (Figure 54(A2 and A3)). Increasing  $Q_1$  increased the O/W emulsion droplets in the first chip. The fluid characteristic inside the channel is displayed in Figure 54(B1-D1). However, raising  $Q_1$  in the high flow rate range also affected fluid characteristics in the second channel. The shell was increased by increasing  $Q_1$  due to the high dispersed phase flow rate resisted the continuous phase. The results affected the core and shell size of microcapsules (Figure 55). The singled-core-shell microcapsules with the thickness of 79.31 and 42.83  $\mu\text{m}$  were investigated at  $Q_1$  at 10.4 and 15.6  $\mu\text{l}/\text{min}$ , respectively. At  $Q_1$  of 20.8  $\mu\text{l}/\text{min}$ , the bigger cores were unable to contain in the smaller shells which make some cores turn inside out from the shell (Figure 54(D3)).

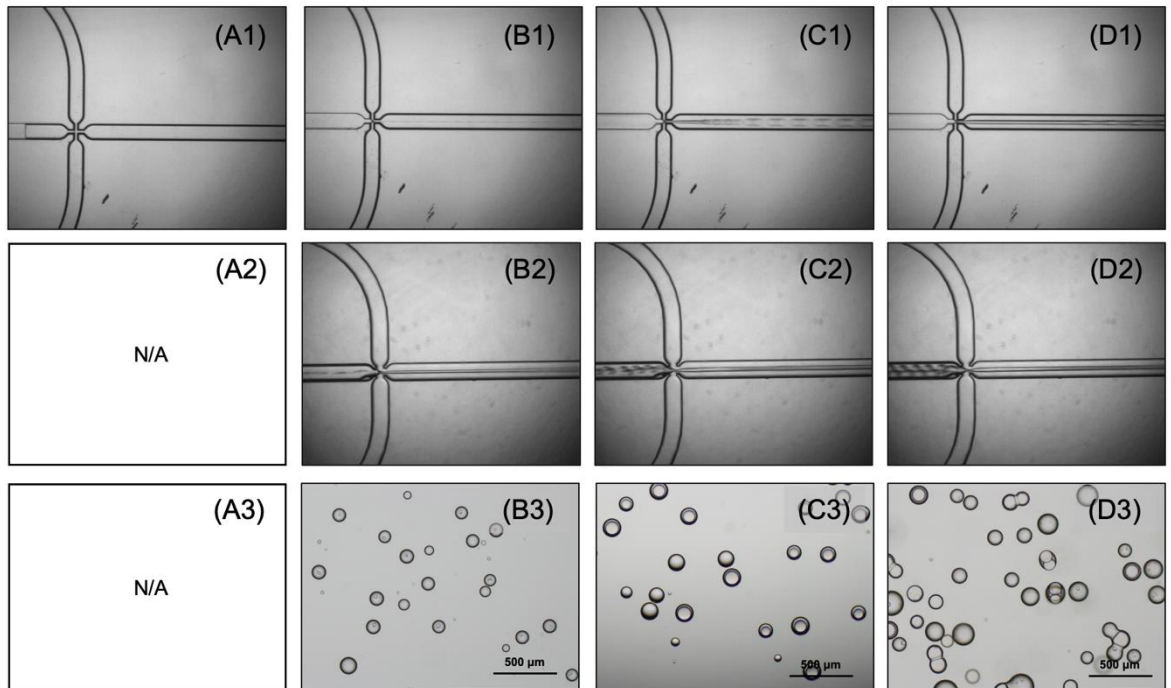


Figure 54 Experimental images of fluid characteristic in (A1-D1) the first microfluidic chip, (A2-D2) the second microfluidic chip, and (A3-D3) core-shell-microcapsules micrograph at constant  $Q_2$  of 18.8 and  $Q_3$  of 86.0  $\mu\text{l}/\text{min}$  which  $Q_1$  of (A1, A2, A3) 5.2  $\mu\text{l}/\text{min}$ , (B1, B2, B3) 10.4  $\mu\text{l}/\text{min}$ , (C1, C2, C3) 15.6  $\mu\text{l}/\text{min}$ , and (D1, D2, D3) 20.8  $\mu\text{l}/\text{min}$ .

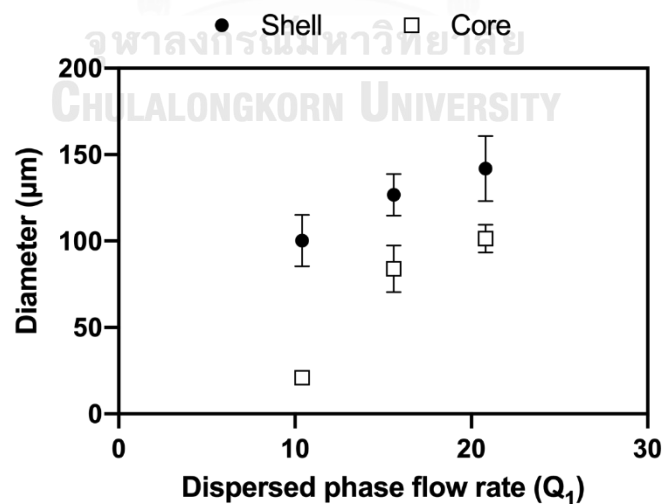


Figure 55 Effect of dispersed flow rate of the first microfluidic chip ( $Q_1$ ) on core and shell diameter of microcapsules at constant  $Q_2$  of 18.8 and  $Q_3$  of 86.0  $\mu\text{l}/\text{min}$ .

### 6.3 Effect of the continuous phase flow rate of the first microfluidic chip ( $Q_2$ )

Under  $Ca_d$  of 0.031, the effect of the continuous phase flow rate of the first chip ( $Q_2$ ) when keeping  $Q_1$  of 2.6 and  $Q_3$  of 8.8  $\mu\text{l}/\text{min}$  is shown in Figure 56. The  $Q_2$  affected both droplets from the first and the second channel. Increasing  $Q_2$  decreased the O/W emulsion droplets due to the high continuous phase flow rate resulting in high shear force which can interrupt the dispersed phase and break up into smaller droplets. The fluid characteristic inside the first channel is displayed in Figure 56(A1-E1). Figure 57 shows the results which indicated that the core size of the microcapsule decreased with an increase in  $Q_2$ . The bigger shell was affected by the high  $Q_2$  which makes a high flow rate in the dispersed phase in the second channel. As mentioned earlier, the high dispersed phase flow rate could resist the shear force of the continuous phase which produces the bigger droplets. The microcapsules were formed as singled-core-shell (Figure 56(A3-E3)) which was produced from the dripping regime in Figure 56(A2-E2). The thickness of microcapsules was 22.70, 25.23, 38.57, 59.10, and 63.10  $\mu\text{m}$  at  $Q_2$  of 1.9, 2.4, 2.8, 3.3, and 3.8  $\mu\text{l}/\text{min}$ , respectively.

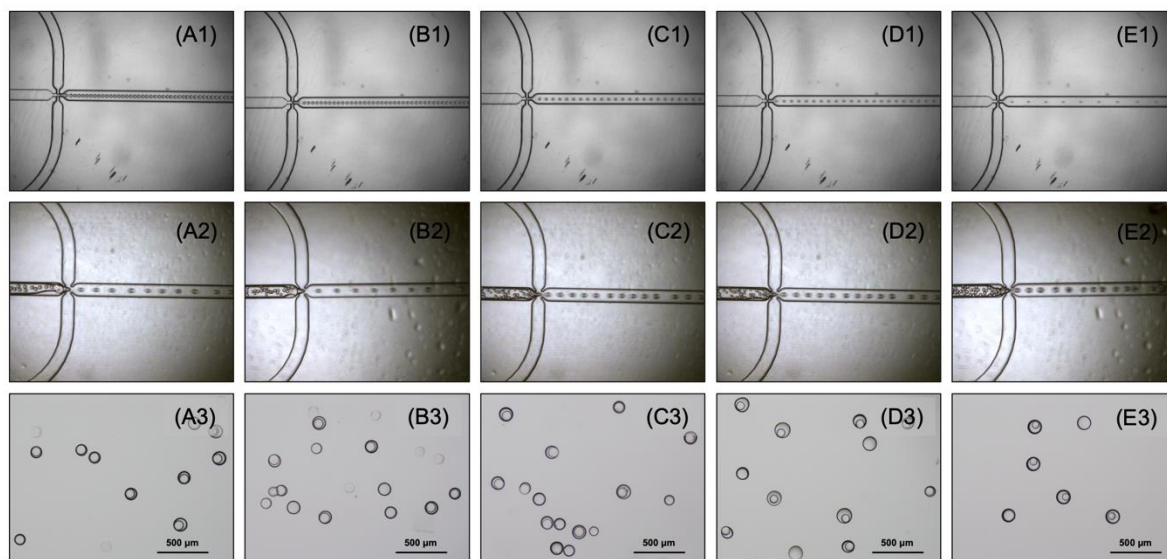


Figure 56 Experimental images of fluid characteristic in (A1-E1) the first microfluidic chip, (A2-E2) the second microfluidic chip, and (A3-E3) core-shell-microcapsules micrograph at constant  $Q_1$  of 2.6 and  $Q_3$  of 8.8  $\mu\text{l}/\text{min}$  which  $Q_2$  of (A1, A2, A3) 1.9  $\mu\text{l}/\text{min}$ , (B1, B2, B3) 2.4  $\mu\text{l}/\text{min}$ , (C1, C2, C3) 2.8  $\mu\text{l}/\text{min}$ , (D1, D2, D3) 3.3  $\mu\text{l}/\text{min}$ , and (E1, E2, E3) 3.8  $\mu\text{l}/\text{min}$ .

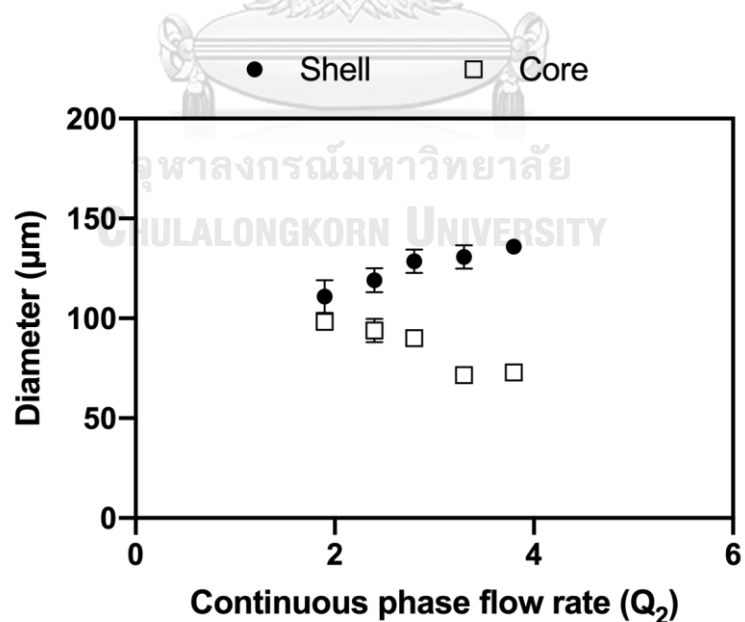
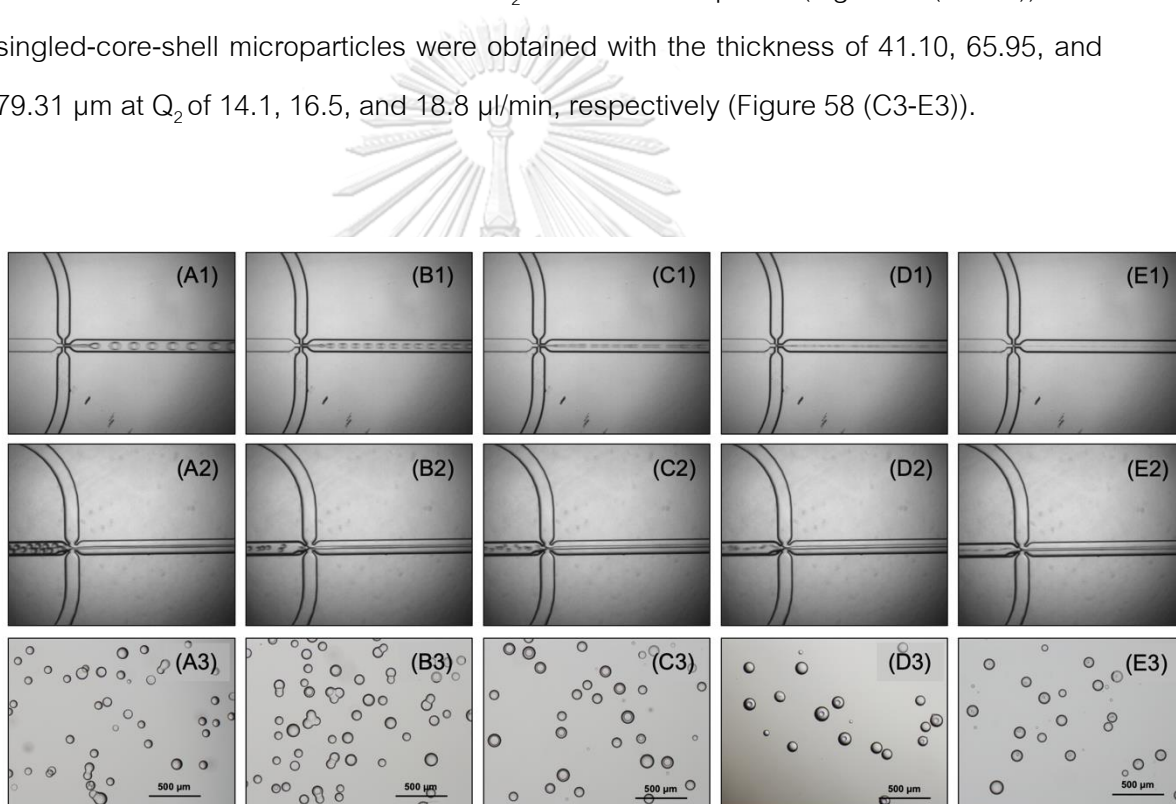


Figure 57 Effect of continuous flow rate of the first microfluidic chip ( $Q_2$ ) on core and shell diameter of microcapsules at constant  $Q_1$  of 2.6 and  $Q_3$  of 8.8  $\mu\text{l}/\text{ml}$ .

Above the  $Ca_d$  of 0.031, the narrowing jet and tip streaming would be focused instead of a squeezing and dripping regime. The effect of  $Q_2$  was studied when keeping  $Q_1$  and  $Q_3$  constant at 10.4 and 86.0  $\mu\text{l}/\text{min}$ , respectively. The  $Q_2$  also affected both droplets from the first and the second channel. Increasing  $Q_2$  decreased the core size (Figure 59). The fluid characteristic inside the first channel is displayed in Figure 58(A1-E1). Figure 58(A2-E2) represents the fluid characteristic inside the second channel. However, the bigger cores were unable to contain in the smaller shells which make the cores turn inside out from the shell at  $Q_2$  of 9.4 to 11.8  $\mu\text{l}/\text{min}$  (Figure 58(A3-B3)). The single-core-shell microparticles were obtained with the thickness of 41.10, 65.95, and 79.31  $\mu\text{m}$  at  $Q_2$  of 14.1, 16.5, and 18.8  $\mu\text{l}/\text{min}$ , respectively (Figure 58 (C3-E3)).



**Figure 58** Experimental images of fluid characteristic in (A1-E1) the first microfluidic chip, (A2-E2) the second microfluidic chip, and (A3-E3) core-shell-microcapsules micrograph at constant  $Q_1$  of 10.4 and  $Q_3$  of 86.0  $\mu\text{l}/\text{min}$  which  $Q_2$  of (A1, A2, A3) 9.4  $\mu\text{l}/\text{min}$ , (B1, B2, B3) 11.8  $\mu\text{l}/\text{min}$ , (C1, C2, C3) 14.1  $\mu\text{l}/\text{min}$ , (D1, D2, D3) 16.5  $\mu\text{l}/\text{min}$ , and (E1, E2, E3) 18.8  $\mu\text{l}/\text{min}$ .

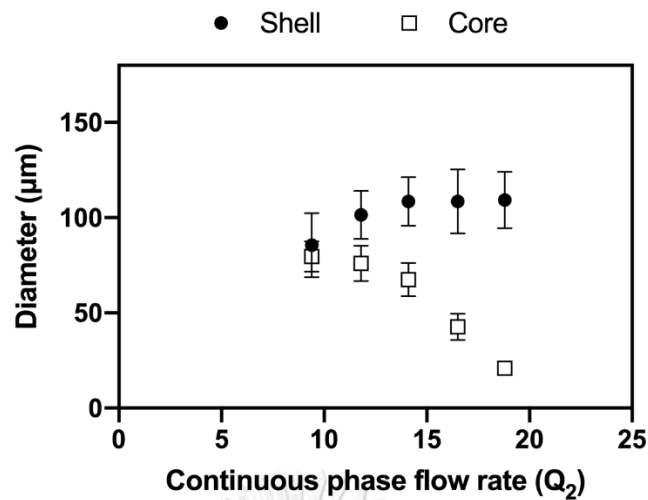


Figure 59 Effect of continuous flow rate of the first microfluidic chip ( $Q_2$ ) on core and shell diameter of microcapsules at constant  $Q_1$  of 10.4 and  $Q_3$  of 86.0  $\mu\text{l}/\text{min}$ .

#### 6.4 Effect of the continuous phase flow rate of the second microfluidic chip ( $Q_3$ )

The effect of the continuous phase flow rate of the second chip ( $Q_3$ ) when keeping  $Q_1$  at 2.6 and  $Q_2$  at 3.3  $\mu\text{l}/\text{min}$  is shown in Figure 60. Under  $Ca_d$  of 0.031, the  $Q_3$  did not show a significant effect on O/W emulsion in the first channel which made the core have an average size of 70-90  $\mu\text{m}$ . However,  $Q_3$  showed a major effect to shell size. At  $Q_3$  of 3.3  $\mu\text{l}/\text{min}$  indicated the squeezing regime (Figure 60(A1)) which the shell was big enough to contain the multiple cores as presented in Figure 60(A2). When  $Q_3$  increased, the size of the shell size was decreased due to the higher shear force of the continuous phase over the interfacial force (Figure 61). The singled-core-shell microcapsules were obtained at  $Q_3$  of 8.8  $\mu\text{l}/\text{min}$ . The average shell size was  $130.70 \pm 5.81 \mu\text{m}$  and the core size was  $71.60 \pm 2.21 \mu\text{m}$ . Thus, the thickness of singled-core-shell microcapsules was 59.10  $\mu\text{m}$  (Figure 60 (E2)). It can be said that  $Q_3$  is the key factor to control the number of core-shell microcapsules. Figure 62 presents the confocal laser scanning microscopy (CLSM) images to confirm the core-shell microcapsule structure. The fluorescence dye of red from rhodamine6G was used in the alginate solution phase which was the shell of the microcapsule (Figure 62 (A2, B2, C2)). The core of the

microcapsules which was the oil phase was added by green color from coumarin6 (Figure 62 (A3, B3, C3)). Figure 59(A4) shows the combined color of the core and shell of the microcapsule at  $Q_3$  of 3.3  $\mu\text{l}/\text{min}$  which indicated the multiplied-core-shell microcapsule. The number of the core in one shell decreased when increase in  $Q_3$  to 6.0  $\mu\text{l}/\text{min}$  (Figure 60(B4)). The singled-core-shell was obtained at  $Q_3$  of 8.8  $\mu\text{l}/\text{min}$  (Figure 60(C4)).

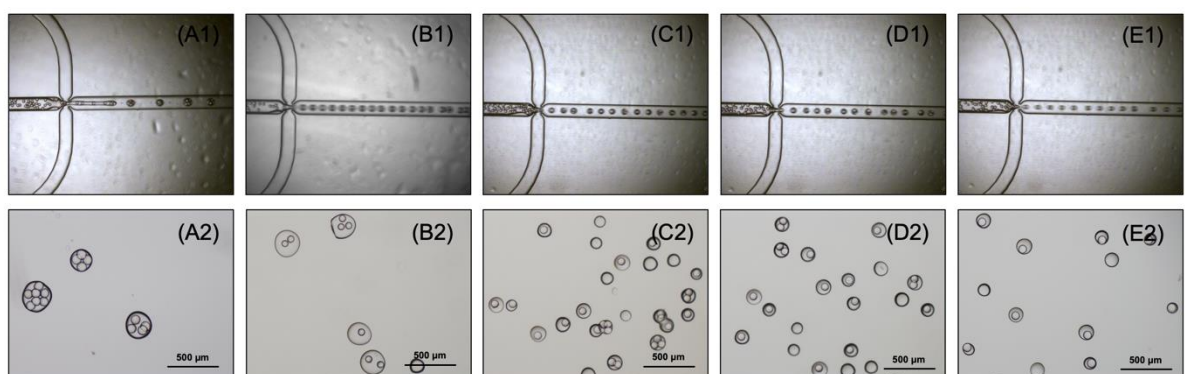


Figure 60 Experimental images of fluid characteristic in (A1-E1) the second microfluidic chip, and (A2-E2) core-shell-microcapsules micrograph at constant  $Q_1$  of 2.6 and  $Q_2$  of 3.3  $\mu\text{l}/\text{min}$  which  $Q_3$  of (A1, A2) 3.3  $\mu\text{l}/\text{min}$ , (B1, B2) 4.6  $\mu\text{l}/\text{min}$ , (C1, C2) 6.0  $\mu\text{l}/\text{min}$ , (D1, D2) 7.4  $\mu\text{l}/\text{min}$ , and (E1, E2) 8.8  $\mu\text{l}/\text{min}$ .

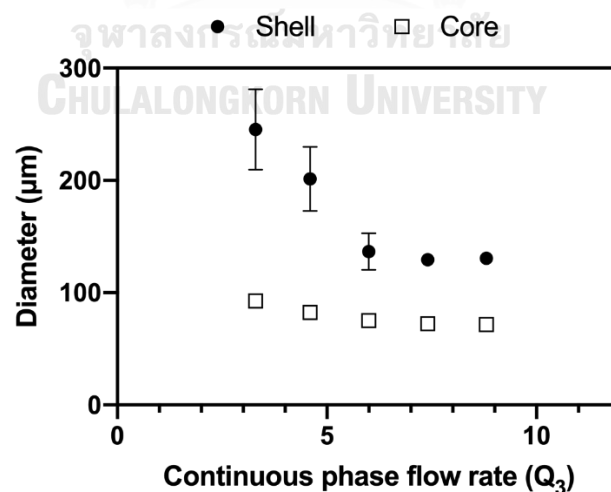


Figure 61 Effect of continuous flow rate of the second microfluidic chip ( $Q_3$ ) on core and shell diameter of microcapsules at constant  $Q_1$  of 2.6 and  $Q_2$  of 3.3  $\mu\text{l}/\text{min}$ .

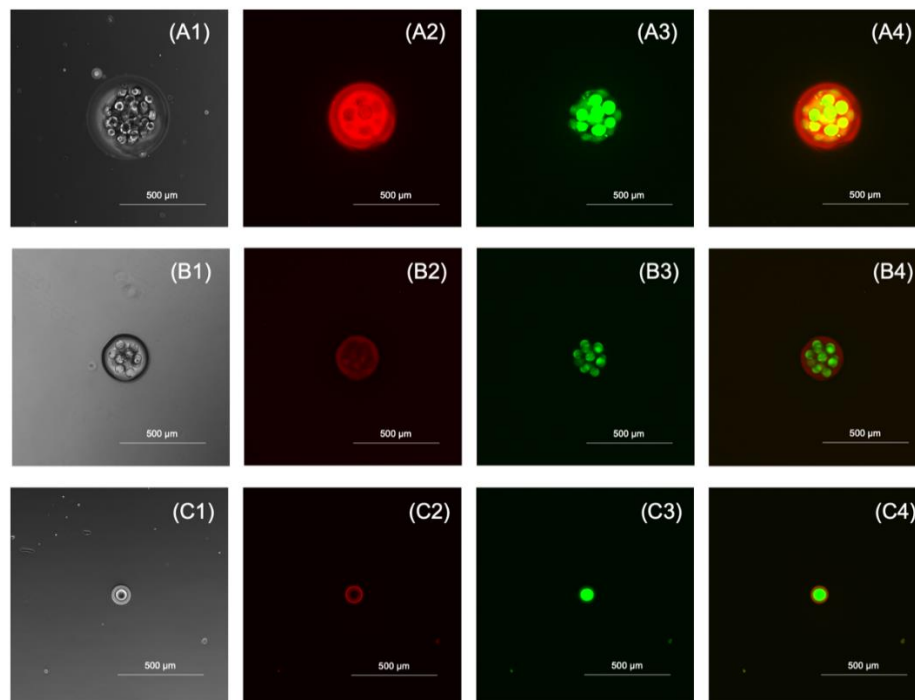
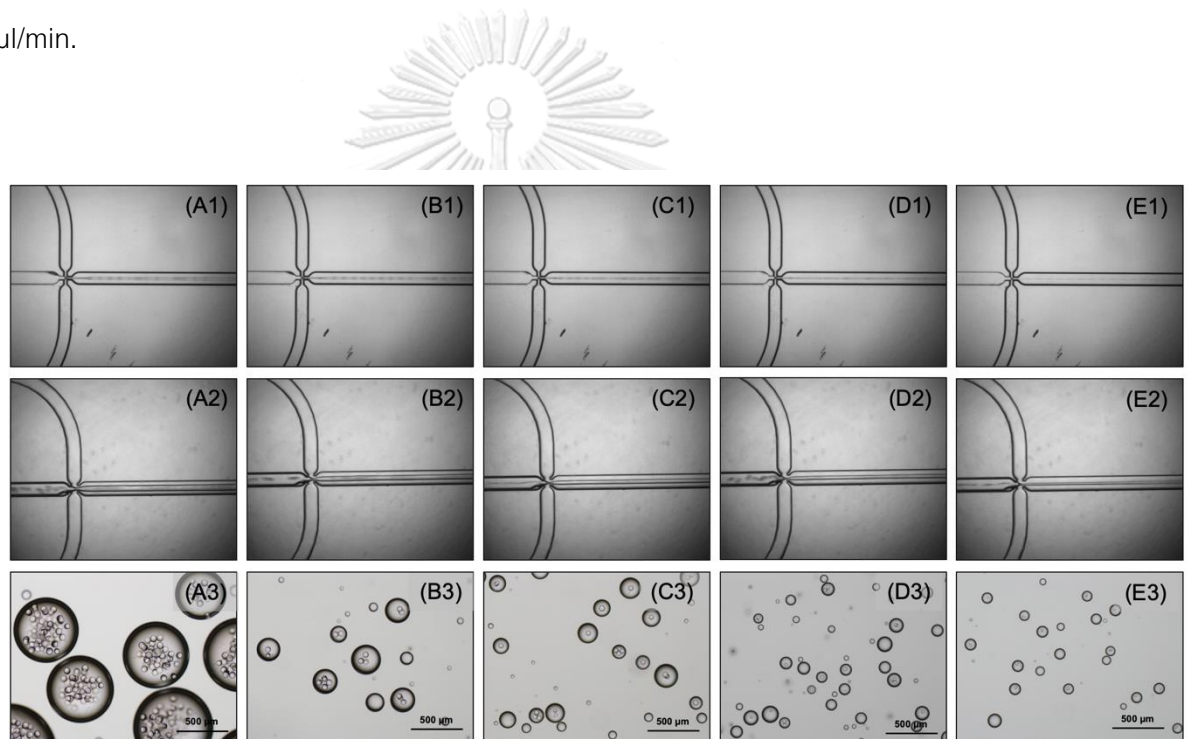


Figure 62 Confocal laser scanning microscopy (CLSM) images of core-shell microcapsules at constant  $Q_1$  of 2.6 and  $Q_2$  of 3.3  $\mu\text{l}/\text{min}$  which  $Q_3$  of (A1-A4) 3.3  $\mu\text{l}/\text{min}$ , (B1-B4) 6.0  $\mu\text{l}/\text{min}$ , and (C1-C4) 8.8  $\mu\text{l}/\text{min}$ ; (A2, B2, C2) images from rhodamine 6G with excitation at 559 nm and emission at 570-670 nm and (A3, B3, C3) images from coumarin6 with excitation at 473 nm and emission at 490-590 nm.

Above  $Ca_d$  of 0.031, the effect of  $Q_3$  was studied when keeping  $Q_1$  and  $Q_2$  constant at 10.4 and 18.8  $\mu\text{l}/\text{min}$ , respectively. The  $Q_3$  still did not show a significant effect on droplet in the first channel which made the core have an average size of 20-40  $\mu\text{m}$ . However,  $Q_3$  showed a higher impact on shell size than core size. The widening jet regime was investigated when  $Q_3$  was 17.6 to 34.4  $\mu\text{l}/\text{min}$  (Figure 63(A2 and B2)). The shell size of  $379.07 \pm 54.31$  and  $220.68 \pm 43.47$   $\mu\text{m}$  were obtained at  $Q_3$  was 17.6 and 34.4  $\mu\text{l}/\text{min}$ , respectively (Figure 63(A3 and B3)). The smaller size than junction size of droplet was obtained in narrowing jet regime which showed at  $Q_3$  of 51.8 to 68.9  $\mu\text{l}/\text{min}$  (Figure 63(C2 and D2)). The average of shell size was  $128.61 \pm 10.81$  and  $113.00 \pm 9.85$   $\mu\text{m}$  at  $Q_3$  of 51.8 and 68.9  $\mu\text{l}/\text{min}$ , respectively. When  $Q_3$  reach to 86.0  $\mu\text{l}/\text{min}$ , the tiny and uniform droplet from tip streaming regime were acquired (Figure 63(E2)). The shell



with average size of  $100.28 \pm 8.89 \mu\text{m}$  was obtained. The CV of droplets from  $Q_3$  of 51.8, 68.9, and 86.0  $\mu\text{l}/\text{min}$  were 8.4, 8.7, and 8.9, respectively. Results from narrowing jet and tip streaming regime also verified the monodispersity since the CV was smaller than 10%, as the standard criterion for monodispersity [96-98]. However, the singled-core-shell could be produced only in tip streaming regime which confirmed in confocal laser scanning microscopy (CLSM) images in Figure 65(B1-B4). While the multiplied-core-shell microcapsules were obtained in widening jet and narrowing jet regime. Figure 65(A1-A4) asserts the multiplied-core-shell from narrowing jet regime at  $Q_3$  of 51.8  $\mu\text{l}/\text{min}$ .



**Figure 63** Experimental images of fluid characteristic in (A1-E1) the first microfluidic chip, (A2-E2) the second microfluidic chip, and (A3-E3) core-shell-microcapsules micrograph at constant  $Q_1$  of 10.4 and  $Q_2$  of 18.8  $\mu\text{l}/\text{min}$  which  $Q_3$  of (A1, A2, A3) 17.6  $\mu\text{l}/\text{min}$ , (B1, B2, B3) 34.4  $\mu\text{l}/\text{min}$ , (C1, C2, C3) 51.8  $\mu\text{l}/\text{min}$ , (D1, D2, D3) 68.9  $\mu\text{l}/\text{min}$ , and (E1, E2, E3) 86.0  $\mu\text{l}/\text{min}$ .

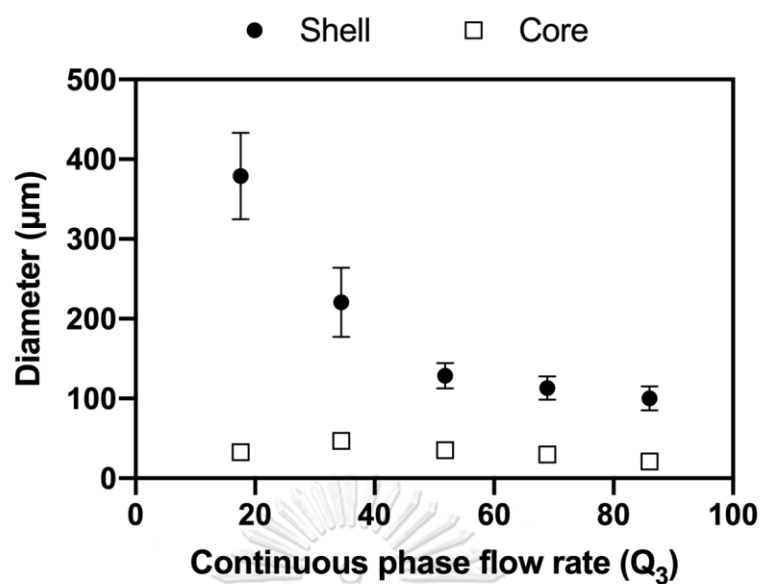


Figure 64 Effect of continuous flow rate of the second microfluidic chip ( $Q_3$ ) on core and shell diameter of microcapsules at constant  $Q_1$  of 10.4 and  $Q_2$  of 18.8  $\mu\text{l}/\text{min}$ .

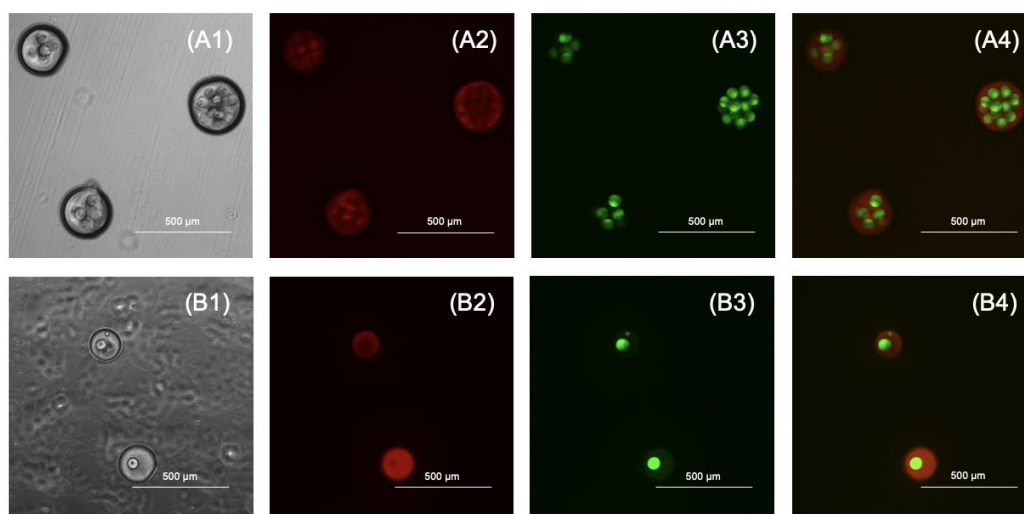


Figure 65 Confocal laser scanning microscopy (CLSM) images of core-shell microcapsules at constant  $Q_1$  of 10.4 and  $Q_2$  of 18.8  $\mu\text{l}/\text{min}$  which at  $Q_3$  of (A1-A4) 51.8  $\mu\text{l}/\text{min}$  and (B1-B4) 86.0  $\mu\text{l}/\text{min}$ ; (A2, B2) images from rhodamine 6G with excitation at 559 nm and emission at 570-670 nm and (A3, B3) images from coumarin 6 with excitation at 473 nm and emission at 490-590 nm.

### 6.5 Dimensionless correlation

Oil in water (W/O) emulsion was produced in the first microfluidic chip with a junction of 100  $\mu\text{m}$  etch depth. The alpha-mangostin in MCT oil and 2%(w/w) alginate solution with 0.1M Ca-EDTA were used as the dispersed and continuous phases, respectively. The flow rate of the dispersed phase ( $Q_1$ ) and continuous phase ( $Q_2$ ) were controlled. The ratio of W/O emulsion core size to microfluidic junction size ( $d_{\text{core}}/j$ ) decreased along with the flow rate ratio of the continuous phase to the dispersed phase ( $Q_2/Q_1$ ) as shown in Figure 66. The oil in water in oil (O/W/O) emulsions were generated in the second microfluidic chip with a junction of 190  $\mu\text{m}$  etch depth. The MCT oil was used as the continuous phase in the second chip. Also, the shell size to microfluidic junction size ( $d_{\text{shell}}/j$ ) decrease with an increase in the flow rate ratio of the continuous phase to the dispersed phase ( $Q_3/(Q_1+2Q_2)$ ) in the second chip. The result of shell size to junction size presents in Figure 67. Droplet size either core or shell decreased with increasing continuous phase flow rate when the dispersed phase flow rate was kept constant. By contrast, when keeping the continuous phase flow rate constant, increase in the dispersed phase flow led to increased droplet size. The results showed the same trend either in low or high flow rate system. At  $Ca_d < 0.031$ , the  $d_p/j$  was investigated around 1 due to the droplet sizes were obtained at squeezing and dripping regime. However, at  $Ca_d > 0.031$ , the  $d_p/j$  could show the lower value which indicated that a smaller droplet size was obtained from narrowing jet and tip streaming regimes. So, the narrowing jet and tip streaming regime were also remarkable due to the smaller than junction size, narrow size distribution, and high production yield in both single emulsion and double emulsion production.

The red symbols in Figure 66 and 67 show the singled-core-shell microcapsules while the black symbols show multiple-core-shell microcapsules. The effect of the flow rate ratio in the first chip could not differentiate the number of the core microcapsules as shown in Figure 66. However, Figure 67 displays the effect of the flow rate ratio in the second chip which shows that the single-core-microcapsules could be generated when increasing  $Q_3/(Q_1+2Q_2)$ . The results indicated that  $Q_3$  was the key factor to control the

number of core-shell microcapsules. Increase continuous flow rate, the flow regime pattern in a low flow rate ( $Ca_d < 0.031$ ) system could initiate from co-flow and then squeezing, transition, dripping, and reverse, respectively. The regime pattern was changed at a high flow rate system ( $Ca_d > 0.031$ ). The widening jet, narrowing jet, and tip streaming regimes were found instead of the squeezing and dripping regime. The single-core-shell microcapsules could be generated only in the dripping regime in a low flow rate system and the narrowing jet and tip streaming regime in a high flow rate system. While in other regime, the multiple-core-shell microcapsules could be produced.



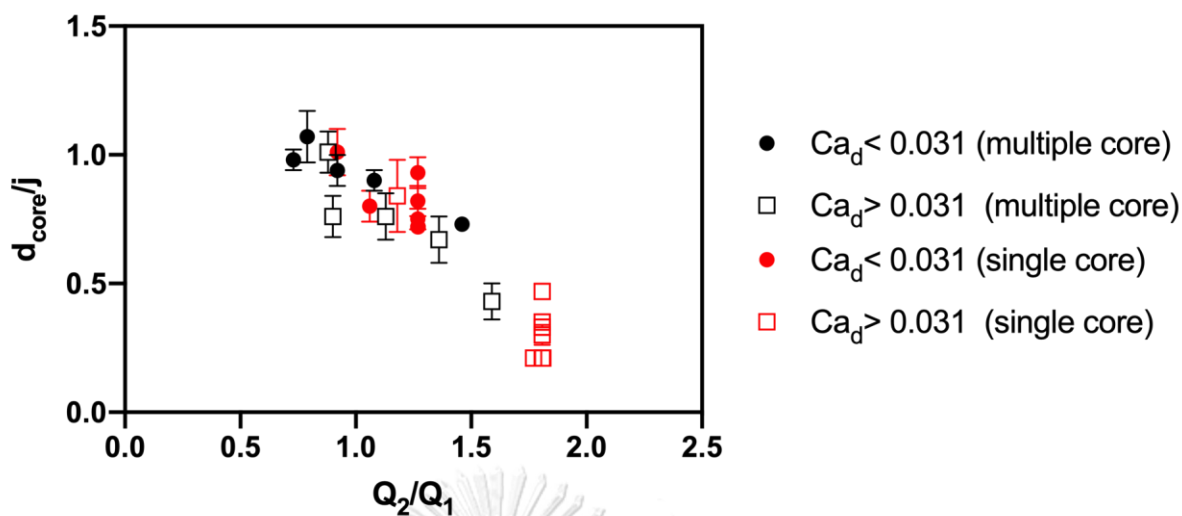


Figure 66 Effect of flow rate ratio ( $Q_2/Q_1$ ) on core size ( $d_{core}$ ) normalized by junction size ( $j$ ) at different conditions.

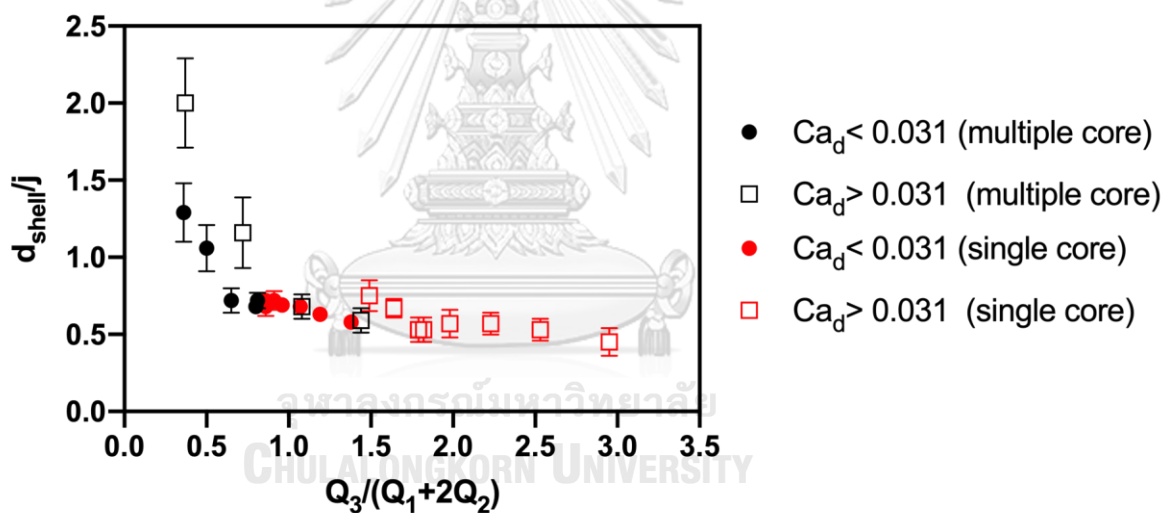


Figure 67 Effect of flow rate ratio ( $Q_3/(Q_1+2Q_2)$ ) on shell size ( $d_{shell}$ ) normalized by junction size ( $j$ ) at different conditions.

## Chapter 7

### Conclusion

This research firstly investigated W/O emulsion droplet formation of various fluid properties based on two junction sizes of a flow-focusing device. Seven flow regimes during droplet generation were identified as co-flow, squeezing, transition, dripping, jetting, tip streaming and reverse. Four regimes of squeezing, dripping, narrowing jet and tip streaming produced monodisperse droplets. Large production rate with tiny droplet was found in the narrowing jet and tip streaming regimes. The effect of flow rate ratio ( $Q_c/Q_d$ ), viscosity ratio ( $\mu_c/\mu_d$ ) and capillary number ( $Ca_c$ ) were also investigated on droplet size at both low and high flow rates. The results showed that droplet size decreased with increase of  $Q_c/Q_d$  and  $Ca_c$ , while  $\mu_c/\mu_d$  did not directly affect droplet size. The droplet forming process in the narrowing jet and tip streaming regimes was influenced by flow rate ratio, viscosity ratio and capillary number. An empirical correlation was presented to estimate the droplet size. The prediction agreed well with the experimental results from 12 data sets over 100 experiments in two different-sized channels. Therefore, the dimensionless correlation can be used as a guideline for droplet and microparticle preparation, with predictable and controllable size using the flow-focusing device.

Then, Internal gelation using water-soluble calcium-ethylenediaminetetraacetic acid (Ca-EDTA) complex as a calcium source was studied to use in biphasic system of alginate crosslinking. The effects of homogenizer speed, Ca-EDTA concentration and crosslinking time were investigated in W/O emulsification method. Isolated alginate particles with the average size of  $39.97 \pm 11.51 \mu\text{m}$  were obtained from emulsification using 5,000 rpm speed of a high-speed homogenizer. Increasing of Ca-EDTA increased the stiffness and %weight of Ca. However, the particles would aggregate at high concentration of Ca-EDTA. The crosslinking time of 5 min was the optimum time of internal gelation via Ca-EDTA, which showed the highest rigid particle with a reasonable high yield. The double-gelation which was internal gelation and then external gelation

resulted in the higher stiffness compared with the particles from only internal crosslinking. In comparison with the emulsification method, the microfluidic method produced particles with more uniform and controllable sizes.

Finally, the core-shell microcapsules were prepared using two connecting microfluidic chips. The first chip would produce an O/W emulsion which had an oil phase contained any active ingredient in the hydrophobic part which would be the core of the microcapsule. The crosslinking of shell was taken place in the second chip via internal gelation using acid to detach the  $\text{Ca}^{2+}$  from Ca-EDTA. The operating condition which was the flow rate was studied. Increasing the dispersed phase flow rate of the first chip ( $Q_1$ ) increased the core size due to the high dispersed phase flow rate resisted the shear force of the continuous phase in both of low and high flow rate system. In the between stream like the continuous phase flow rate of the first chip ( $Q_2$ ) affected both core and shell size. For the continuous phase flow rate of the second chip ( $Q_3$ ), when  $Q_3$  increased, the size of the shell was decreased due to the higher shear force of the continuous phase over the interfacial force. However, the  $Q_3$  had an effect to the ability of containing single or multiple cores. At low  $Q_3$ , the squeezing in low flow rate system and widening jet in high flow rate were obtained, the shells were big enough to contain the multiple cores. When increase  $Q_3$  to the point, dripping in low flow rate and tip streaming in high flow rate, the singled-core-shell microcapsules were investigated. So, the key factor to control the number of cores was  $Q_3$ .

## REFERENCES

- [1] N.J. Zuidam, V. Nedovic, Encapsulation technologies for active food ingredients and food processing, (2010).
- [2] N.-T. Nguyen, M. Hejazian, C. Ooi, N. Kashaninejad, Recent advances and future perspectives on microfluidic liquid handling, *Micromachines* 8 (2017) 186.
- [3] P. Umbanhowar, V. Prasad, D.A. Weitz, Monodisperse emulsion generation via drop break off in a coflowing stream, *Langmuir* 16 (2000) 347-351.
- [4] A.S. Utada, A. Fernandez-Nieves, H.A. Stone, D.A. Weitz, Dripping to jetting transitions in coflowing liquid streams, *Physical review letters* 99 (2007) 094502.
- [5] T. Thorsen, R.W. Roberts, F.H. Arnold, S.R. Quake, Dynamic pattern formation in a vesicle-generating microfluidic device, *Physical review letters* 86 (2001) 4163.
- [6] C.-X. Zhao, A.P. Middelberg, Two-phase microfluidic flows, *Chemical Engineering Science* 66 (2011) 1394-1411.
- [7] J. Xu, S. Li, J. Tan, Y. Wang, G. Luo, Preparation of highly monodisperse droplet in a T-junction microfluidic device, *AIChE journal* 52 (2006) 3005-3010.
- [8] M.L. Steegmans, K.G. Schroën, R.M. Boom, Characterization of emulsification at flat microchannel Y junctions, *Langmuir* 25 (2009) 3396-3401.
- [9] R. Lin, J.S. Fisher, M.G. Simon, A.P. Lee, Novel on-demand droplet generation for selective fluid sample extraction, *Biomicrofluidics* 6 (2012) 024103.
- [10] M. Rhee, P. Liu, R.J. Meagher, Y.K. Light, A.K. Singh, Versatile on-demand droplet generation for controlled encapsulation, *Biomicrofluidics* 8 (2014) 034112.
- [11] Y. Ding, X.C. i Solvas, "V-junction": a novel structure for high-speed generation of bespoke droplet flows, *Analyst* 140 (2015) 414-421.
- [12] U. Tangen, A. Sharma, P. Wagler, J.S. McCaskill, On demand nanoliter-scale microfluidic droplet generation, injection, and mixing using a passive microfluidic device, *Biomicrofluidics* 9 (2015) 014119.
- [13] L. Yobas, S. Martens, W.-L. Ong, N. Ranganathan, High-performance flow-focusing geometry for spontaneous generation of monodispersed droplets, *Lab on a Chip* 6 (2006)



1073-1079.

- [14] J. Guerrero, Y.W. Chang, A.A. Fragkopoulos, A. Fernandez-Nieves, Capillary-Based Microfluidics—Coflow, Flow-Focusing, Electro-Coflow, Drops, Jets, and Instabilities, *Small* 16 (2020) 1904344.
- [15] G.F. Christopher, S.L. Anna, Microfluidic methods for generating continuous droplet streams, *Journal of Physics D: Applied Physics* 40 (2007) R319.
- [16] P. Zhu, L. Wang, Passive and active droplet generation with microfluidics: a review, *Lab on a Chip* 17 (2017) 34-75.
- [17] J.D. Tice, A.D. Lyon, R.F. Ismagilov, Effects of viscosity on droplet formation and mixing in microfluidic channels, *Analytica chimica acta* 507 (2004) 73-77.
- [18] P. Garstecki, M.J. Fuerstman, H.A. Stone, G.M. Whitesides, Formation of droplets and bubbles in a microfluidic T-junction—scaling and mechanism of break-up, *Lab on a Chip* 6 (2006) 437-446.
- [19] M. De Menech, P. Garstecki, F. Jousse, H. Stone, Transition from squeezing to dripping in a microfluidic T-shaped junction, *Journal of Fluid Mechanics* 595 (2008) 141-161.
- [20] I. Kobayashi, S. Mukataka, M. Nakajima, Effects of type and physical properties of oil phase on oil-in-water emulsion droplet formation in straight-through microchannel emulsification, experimental and CFD studies, *Langmuir* 21 (2005) 5722-5730.
- [21] C. Cramer, P. Fischer, E.J. Windhab, Drop formation in a co-flowing ambient fluid, *Chemical Engineering Science* 59 (2004) 3045-3058.
- [22] K.-S. Huang, T.-H. Lai, Y.-C. Lin, Manipulating the generation of Ca-alginate microspheres using microfluidic channels as a carrier of gold nanoparticles, *Lab on a Chip* 6 (2006) 954-957.
- [23] C.-H. Yeh, Q. Zhao, S.-J. Lee, Y.-C. Lin, Using a T-junction microfluidic chip for monodisperse calcium alginate microparticles and encapsulation of nanoparticles, *Sensors and Actuators A: Physical* 151 (2009) 231-236.
- [24] R. Vasiliauskas, D. Liu, S. Cito, H. Zhang, M.-A. Shahbazi, T. Sikanen, L. Mazutis, H.I.A. Santos, Simple microfluidic approach to fabricate monodisperse hollow

microparticles for multidrug delivery, *ACS applied materials & interfaces* 7 (2015) 14822-14832.

[25] Z. Luo, G. Zhao, F. Panhwar, M.F. Akbar, Z. Shu, Well-designed microcapsules fabricated using droplet-based microfluidic technique for controlled drug release, *Journal of Drug Delivery Science and Technology* 39 (2017) 379-384.

[26] C.-H. Yeh, Y.-C. Chen, Y.-C. Lin, Generation of droplets with different concentrations using gradient-microfluidic droplet generator, *Microfluidics and nanofluidics* 11 (2011) 245-253.

[27] Q. Xu, M. Nakajima, The generation of highly monodisperse droplets through the breakup of hydrodynamically focused microthread in a microfluidic device, *Applied Physics Letters* 85 (2004) 3726-3728.

[28] H. Liu, Y. Zhang, Droplet formation in microfluidic cross-junctions, *Physics of Fluids* 23 (2011) 082101.

[29] G.F. Christopher, N.N. Noharuddin, J.A. Taylor, S.L. Anna, Experimental observations of the squeezing-to-dripping transition in T-shaped microfluidic junctions, *Physical Review E* 78 (2008) 036317.

[30] H. Liu, Y. Zhang, Droplet formation in a T-shaped microfluidic junction, *Journal of applied physics* 106 (2009) 034906.

[31] J. Xu, S. Li, J. Tan, G. Luo, Correlations of droplet formation in T-junction microfluidic devices: from squeezing to dripping, *Microfluidics and Nanofluidics* 5 (2008) 711-717.

[32] J. Xu, G. Luo, S. Li, G. Chen, Shear force induced monodisperse droplet formation in a microfluidic device by controlling wetting properties, *Lab on a Chip* 6 (2006) 131-136.

[33] J. Xu, S. Li, J. Tan, Y. Wang, G. Luo, Controllable preparation of monodisperse O/W and W/O emulsions in the same microfluidic device, *Langmuir* 22 (2006) 7943-7946.

[34] J.D. Tice, H. Song, A.D. Lyon, R.F. Ismagilov, Formation of droplets and mixing in multiphase microfluidics at low values of the Reynolds and the capillary numbers, *Langmuir* 19 (2003) 9127-9133.

[35] J. Xu, S. Li, Y. Wang, G. Luo, Controllable gas-liquid phase flow patterns and monodisperse microbubbles in a microfluidic T-junction device, *Applied Physics Letters* 88

(2006) 133506.

[36] T. Fu, Y. Ma, D. Funfschilling, C. Zhu, H.Z. Li, Squeezing-to-dripping transition for bubble formation in a microfluidic T-junction, *Chemical engineering science* 65 (2010) 3739-3748.

[37] J. Tan, J. Xu, S. Li, G. Luo, Drop dispenser in a cross-junction microfluidic device: Scaling and mechanism of break-up, *Chemical Engineering Journal* 136 (2008) 306-311.

[38] F. Lapierre, N. Wu, Y. Zhu, Influence of flow rate on the droplet generation process in a microfluidic chip, *Smart Nano-Micro Materials and Devices*, International Society for Optics and Photonics, 2011, pp. 82040H.

[39] A. Matalanis, O.G. Jones, D.J. McClements, Structured biopolymer-based delivery systems for encapsulation, protection, and release of lipophilic compounds, *Food Hydrocolloids* 25 (2011) 1865-1880.

[40] D.J. McClements, Designing biopolymer microgels to encapsulate, protect and deliver bioactive components: Physicochemical aspects, *Advances in colloid and interface science* 240 (2017) 31-59.

[41] A.A. Thorat, S.V. Dalvi, Liquid antisolvent precipitation and stabilization of nanoparticles of poorly water soluble drugs in aqueous suspensions: Recent developments and future perspective, *Chemical Engineering Journal* 181 (2012) 1-34.

[42] J.-Y. Leong, W.-H. Lam, K.-W. Ho, W.-P. Voo, M.F.-X. Lee, H.-P. Lim, S.-L. Lim, B.-T. Tey, D. Poncelet, E.-S. Chan, Advances in fabricating spherical alginate hydrogels with controlled particle designs by ionotropic gelation as encapsulation systems, *Particuology* 24 (2016) 44-60.

[43] D. Liu, H. Zhang, F. Fontana, J.T. Hirvonen, H.A. Santos, Microfluidic-assisted fabrication of carriers for controlled drug delivery, *Lab on a Chip* 17 (2017) 1856-1883.

[44] C.-X. Zhao, Multiphase flow microfluidics for the production of single or multiple emulsions for drug delivery, *Advanced drug delivery reviews* 65 (2013) 1420-1446.

[45] D. Liu, H. Zhang, B. Herranz-Blanco, E. Mäkilä, V.P. Lehto, J. Salonen, J. Hirvonen, H.A. Santos, Microfluidic Assembly of Monodisperse Multistage pH-Responsive Polymer/Porous Silicon Composites for Precisely Controlled Multi-Drug Delivery, *Small* 10

(2014) 2029-2038.

[46] Q. Xu, M. Hashimoto, T.T. Dang, T. Hoare, D.S. Kohane, G.M. Whitesides, R. Langer, D.G. Anderson, Preparation of monodisperse biodegradable polymer microparticles using a microfluidic flow-focusing device for controlled drug delivery, *small* 5 (2009) 1575-1581.

[47] M.A. Neves, H.S. Ribeiro, I. Kobayashi, M. Nakajima, Encapsulation of lipophilic bioactive molecules by microchannel emulsification, *Food Biophysics* 3 (2008) 126-131.

[48] Q. Wang, S. Liu, H. Wang, J. Zhu, Y. Yang, Alginate droplets pre-crosslinked in microchannels to prepare monodispersed spherical microgels, *Colloids and surfaces A: physicochemical and engineering aspects* 482 (2015) 371-377.

[49] V. Zamora-Mora, D. Velasco, R. Hernández, C. Mijangos, E. Kumacheva, Chitosan/agarose hydrogels: Cooperative properties and microfluidic preparation, *Carbohydrate polymers* 111 (2014) 348-355.

[50] D. Jagadeesan, I. Nasimova, I. Gourevich, S. Starodubtsev, E. Kumacheva, Microgels for the Encapsulation and Stimulus-Responsive Release of Molecules with Distinct Polarities, *Macromolecular bioscience* 11 (2011) 889-896.

[51] J. Tan, S. Li, K. Wang, G. Luo, Gas-liquid flow in T-junction microfluidic devices with a new perpendicular rupturing flow route, *Chemical Engineering Journal* 146 (2009) 428-433.

[52] K.-S. Huang, Y.-S. Lin, C.-H. Yang, C.-W. Tsai, M.-Y. Hsu, In situ synthesis of twin monodispersed alginate microparticles, *Soft Matter* 7 (2011) 6713-6718.

[53] L.M.C. Aguilar, S. Duchi, C. Onofrillo, C.D. O'Connell, C. Di Bella, S.E. Moulton, Formation of alginate microspheres prepared by optimized microfluidics parameters for high encapsulation of bioactive molecules, *Journal of Colloid and Interface Science* 587 (2021) 240-251.

[54] K. Jiang, C. Xue, C. Arya, C. Shao, E.O. George, D.L. DeVoe, S.R. Raghavan, A New Approach to In-Situ "Micromanufacturing": Microfluidic Fabrication of Magnetic and Fluorescent Chains Using Chitosan Microparticles as Building Blocks, *Small* 7 (2011) 2470-2476.

[55] C.-H. Yang, K.-S. Huang, P.-W. Lin, Y.-C. Lin, Using a cross-flow microfluidic chip and

external crosslinking reaction for monodisperse TPP-chitosan microparticles, *Sensors and actuators B: Chemical* 124 (2007) 510-516.

[56] C.-H. Yang, K.-S. Huang, J.-Y. Chang, Manufacturing monodisperse chitosan microparticles containing ampicillin using a microchannel chip, *Biomedical microdevices* 9 (2007) 253-259.

[57] M. Windbergs, Y. Zhao, J. Heyman, D.A. Weitz, Biodegradable core-shell carriers for simultaneous encapsulation of synergistic actives, *Journal of the American Chemical Society* 135 (2013) 7933-7937.

[58] D. Lensen, K. van Breukelen, D.M. Vriezema, J.C. van Hest, Preparation of biodegradable liquid core PLLA microcapsules and hollow PLLA microcapsules using microfluidics, *Macromolecular bioscience* 10 (2010) 475-480.

[59] S.-H. Kim, J.W. Kim, J.-C. Cho, D.A. Weitz, Double-emulsion drops with ultra-thin shells for capsule templates, *Lab on a Chip* 11 (2011) 3162-3166.

[60] H.C. Shum, D. Lee, I. Yoon, T. Kodger, D.A. Weitz, Double emulsion templated monodisperse phospholipid vesicles, *Langmuir* 24 (2008) 7651-7653.

[61] P.-W. Ren, X.-J. Ju, R. Xie, L.-Y. Chu, Monodisperse alginate microcapsules with oil core generated from a microfluidic device, *Journal of colloid and interface science* 343 (2010) 392-395.

[62] L. Liu, J.-P. Yang, X.-J. Ju, R. Xie, Y.-M. Liu, W. Wang, J.-J. Zhang, C.H. Niu, L.-Y. Chu, Monodisperse core-shell chitosan microcapsules for pH-responsive burst release of hydrophobic drugs, *Soft Matter* 7 (2011) 4821-4827.

[63] K.-S. Huang, K. Lu, C.-S. Yeh, S.-R. Chung, C.-H. Lin, C.-H. Yang, Y.-S. Dong, Microfluidic controlling monodisperse microdroplet for 5-fluorouracil loaded genipin-gelatin microcapsules, *Journal of Controlled Release* 137 (2009) 15-19.

[64] S. Seiffert, J. Thiele, A.R. Abate, D.A. Weitz, Smart microgel capsules from macromolecular precursors, *Journal of the American Chemical Society* 132 (2010) 6606-6609.

[65] P. Stolzenburg, T. Lorenz, A. Dietzel, G. Garnweitner, Microfluidic synthesis of metal oxide nanoparticles via the nonaqueous method, *Chemical Engineering Science* 191

(2018) 500-510.

[66] M.V. Bandulasena, G.T. Vladislavljević, B. Benyahia, Droplet-based microfluidic method for robust preparation of gold nanoparticles in axisymmetric flow focusing device, *Chemical Engineering Science* 195 (2019) 657-664.

[67] S. Akbari, T. Pirbodaghi, Microfluidic encapsulation of cells in alginate particles via an improved internal gelation approach, *Microfluidics and nanofluidics* 16 (2014) 773-777.

[68] R. Chen, Z. Sun, D. Chen, Droplet-based microfluidics for cell encapsulation and delivery, *Microfluidics for Pharmaceutical Applications*, Elsevier 2019, pp. 307-335.

[69] K. Keohane, D. Brennan, P. Galvin, B.T. Griffin, Silicon microfluidic flow focusing devices for the production of size-controlled PLGA based drug loaded microparticles, *International journal of pharmaceutics* 467 (2014) 60-69.

[70] C. Zhang, R. Grossier, L. Lacaria, F. Rico, N. Candoni, S. Veessler, A microfluidic method generating monodispersed microparticles with controllable sizes and mechanical properties, *Chemical Engineering Science* 211 (2020) 115322.

[71] R. Ran, Q. Sun, T. Baby, D. Wibowo, A.P. Middelberg, C.-X. Zhao, Multiphase microfluidic synthesis of micro-and nanostructures for pharmaceutical applications, *Chemical Engineering Science* 169 (2017) 78-96.

[72] C.-J. Hsiao, J.-F. Lin, H.-Y. Wen, Y.-M. Lin, C.-H. Yang, K.-S. Huang, J.-F. Shaw, Enhancement of the stability of chlorophyll using chlorophyll-encapsulated polycaprolactone microparticles based on droplet microfluidics, *Food chemistry* 306 (2020) 125300.

[73] M. Marquis, J. Davy, B. Cathala, A. Fang, D. Renard, Microfluidics assisted generation of innovative polysaccharide hydrogel microparticles, *Carbohydrate polymers* 116 (2015) 189-199.

[74] X. Sun, C. Zhu, T. Fu, Y. Ma, H.Z. Li, Dynamics of droplet breakup and formation of satellite droplets in a microfluidic T-junction, *Chemical Engineering Science* 188 (2018) 158-169.

[75] Y. Yan, D. Guo, S. Wen, Numerical simulation of junction point pressure during droplet formation in a microfluidic T-junction, *Chemical engineering science* 84 (2012) 591-601.

- [76] M.Y.A. Jamalabadi, M. DaqiqShirazi, A. Kosar, M.S. Shadloo, Effect of injection angle, density ratio, and viscosity on droplet formation in a microfluidic T-junction, *Theoretical and Applied Mechanics Letters* 7 (2017) 243-251.
- [77] S. Zhang, C. Guivier-Curien, S. Veessler, N. Candoni, Prediction of sizes and frequencies of nanoliter-sized droplets in cylindrical T-junction microfluidics, *Chemical Engineering Science* 138 (2015) 128-139.
- [78] Q. Zhang, C. Zhu, W. Du, C. Liu, T. Fu, Y. Ma, H.Z. Li, Formation dynamics of elastic droplets in a microfluidic T-junction, *Chemical Engineering Research and Design* 139 (2018) 188-196.
- [79] R.M. Santos, M. Kawaji, Numerical modeling and experimental investigation of gas-liquid slug formation in a microchannel T-junction, *International Journal of Multiphase Flow* 36 (2010) 314-323.
- [80] S. Van Loo, S. Stoukatch, M. Kraft, T. Gilet, Droplet formation by squeezing in a microfluidic cross-junction, *Microfluidics and Nanofluidics* 20 (2016) 146.
- [81] P.A. Romero, A.R. Abate, Flow focusing geometry generates droplets through a plug and squeeze mechanism, *Lab on a Chip* 12 (2012) 5130-5132.
- [82] A. Gupta, H.S. Matharoo, D. Makkar, R. Kumar, Droplet formation via squeezing mechanism in a microfluidic flow-focusing device, *Computers & Fluids* 100 (2014) 218-226.
- [83] W. Du, T. Fu, Y. Duan, C. Zhu, Y. Ma, H.Z. Li, Breakup dynamics for droplet formation in shear-thinning fluids in a flow-focusing device, *Chemical Engineering Science* 176 (2018) 66-76.
- [84] P. Garstecki, H.A. Stone, G.M. Whitesides, Mechanism for flow-rate controlled breakup in confined geometries: A route to monodisperse emulsions, *Physical review letters* 94 (2005) 164501.
- [85] Z. Nie, M. Seo, S. Xu, P.C. Lewis, M. Mok, E. Kumacheva, G.M. Whitesides, P. Garstecki, H.A. Stone, Emulsification in a microfluidic flow-focusing device: effect of the viscosities of the liquids, *Microfluidics and Nanofluidics* 5 (2008) 585-594.
- [86] L. Peng, M. Yang, S.-s. Guo, W. Liu, X.-z. Zhao, The effect of interfacial tension on

droplet formation in flow-focusing microfluidic device, *Biomedical microdevices* 13 (2011) 559-564.

[87] Z. Wu, Z. Cao, B. Sundén, Liquid-liquid flow patterns and slug hydrodynamics in square microchannels of cross-shaped junctions, *Chemical Engineering Science* 174 (2017) 56-66.

[88] T. Fu, Y. Wu, Y. Ma, H.Z. Li, Droplet formation and breakup dynamics in microfluidic flow-focusing devices: from dripping to jetting, *Chemical engineering science* 84 (2012) 207-217.

[89] S.L. Anna, H.C. Mayer, Microscale tipstreaming in a microfluidic flow focusing device, *Physics of Fluids* 18 (2006) 121512.

[90] S. Lignel, A.-V. Salsac, A. Drelich, E. Leclerc, I. Pezron, Water-in-oil droplet formation in a flow-focusing microsystem using pressure-and flow rate-driven pumps, *Colloids and Surfaces A: Physicochemical and Engineering Aspects* 531 (2017) 164-172.

[91] E. Castro-Hernández, F. Campo-Cortés, J.M. Gordillo, Slender-body theory for the generation of micrometre-sized emulsions through tip streaming, *Journal of fluid mechanics* 698 (2012) 423.

[92] L. Shui, F. Mugele, A. van den Berg, J.C. Eijkel, Geometry-controlled droplet generation in head-on microfluidic devices, *Applied physics letters* 93 (2008) 153113.

[93] P. Zhu, T. Kong, Z. Kang, X. Tian, L. Wang, Tip-multi-breaking in capillary microfluidic devices, *Scientific reports* 5 (2015) 11102.

[94] M. De Menech, P. Garstecki, F. Jousse, H.A. Stone, Transition from squeezing to dripping in a microfluidic T-shaped junction, *journal of fluid mechanics* 595 (2008) 141-161.

[95] Y. Chen, J.-H. Xu, G.-S. Luo, The dynamic adsorption of different surfactants on droplet formation in coaxial microfluidic devices, *Chemical Engineering Science* 138 (2015) 655-662.

[96] I. Kobayashi, M. Nakajima, H. Nabetani, Y. Kikuchi, A. Shohno, K. Satoh, Preparation of micron-scale monodisperse oil-in-water microspheres by microchannel emulsification, *Journal of the american oil chemists' society* 78 (2001) 797-802.



- [97] S. Gu, J. Onishi, Y. Kobayashi, D. Nagao, M. Konno, Preparation and colloidal stability of monodisperse magnetic polymer particles, *Journal of colloid and interface science* 289 (2005) 419-426.
- [98] S. Inukai, T. Tanma, S. Orihara, M. Konno, A simple method for producing micron-sized, highly monodisperse polystyrene particles in aqueous media: Effects of impeller speed on particle size distribution, *Chemical Engineering Research and Design* 79 (2001) 901-905.
- [99] P. Day, A. Manz, Y. Zhang, *Microdroplet technology: principles and emerging applications in biology and chemistry*, Springer Science & Business Media 2012.
- [100] J.H. Xu, S. Li, J. Tan, G. Luo, Correlations of droplet formation in T-junction microfluidic devices: from squeezing to dripping, *Microfluidics and Nanofluidics* 5 (2008) 711-717.
- [101] L. Bai, Y. Fu, S. Zhao, Y. Cheng, Droplet formation in a microfluidic T-junction involving highly viscous fluid systems, *Chemical Engineering Science* 145 (2016) 141-148.
- [102] A. Gupta, S.S. Murshed, R. Kumar, Droplet formation and stability of flows in a microfluidic T-junction, *Applied physics letters* 94 (2009) 164107.
- [103] T. Fu, Y. Ma, H.Z. Li, Breakup dynamics of slender droplet formation in shear-thinning fluids in flow-focusing devices, *Chemical Engineering Science* 144 (2016) 75-86.
- [104] W. Yu, X. Liu, Y. Zhao, Y. Chen, Droplet generation hydrodynamics in the microfluidic cross-junction with different junction angles, *Chemical Engineering Science* 203 (2019) 259-284.
- [105] Z. Wu, Z. Cao, B. Sunden, Flow patterns and slug scaling of liquid-liquid flow in square microchannels, *International Journal of Multiphase Flow* 112 (2019) 27-39.
- [106] Q. Chen, J. Li, Y. Song, B. Chen, D.M. Christopher, X. Li, Pressure-driven microfluidic droplet formation in Newtonian and shear-thinning fluids in glass flow-focusing microchannels, *International Journal of Multiphase Flow* 140 (2021) 103648.
- [107] C. Deng, H. Wang, W. Huang, S. Cheng, Numerical and experimental study of oil-in-water (O/W) droplet formation in a co-flowing capillary device, *Colloids and Surfaces A: Physicochemical and Engineering Aspects* 533 (2017) 1-8.

- [108] A. Marín, F. Campo-Cortés, J. Gordillo, Generation of micron-sized drops and bubbles through viscous coflows, *Colloids and Surfaces A: Physicochemical and Engineering Aspects* 344 (2009) 2-7.
- [109] T. Cubaud, T.G. Mason, Capillary threads and viscous droplets in square microchannels, *Physics of fluids* 20 (2008) 053302.
- [110] M. George, T.E. Abraham, Polyionic hydrocolloids for the intestinal delivery of protein drugs: alginate and chitosan—a review, *Journal of controlled release* 114 (2006) 1-14.
- [111] B. Rashidzadeh, E. Shokri, G.R. Mahdavinia, R. Moradi, S. Mohamadi-Aghdam, S. Abdi, Preparation and characterization of antibacterial magnetic-/pH-sensitive alginate/Ag/Fe<sub>3</sub>O<sub>4</sub> hydrogel beads for controlled drug release, *International journal of biological macromolecules* 154 (2020) 134-141.
- [112] Y. Li, R. Fan, H. Xing, Y. Fei, J. Cheng, L. Lu, Study on swelling and drug releasing behaviors of ibuprofen-loaded bimetallic alginate aerogel beads with pH-responsive performance, *Colloids and Surfaces B: Biointerfaces* (2021) 111895.
- [113] S. Kulanthaivel, T. Agarwal, V.S. Rathnam, K. Pal, I. Banerjee, Cobalt doped nano-hydroxyapatite incorporated gum tragacanth-alginate beads as angiogenic-osteogenic cell encapsulation system for mesenchymal stem cell based bone tissue engineering, *International Journal of Biological Macromolecules* 179 (2021) 101-115.
- [114] K.Y. Lee, D.J. Mooney, Alginate: properties and biomedical applications, *Progress in polymer science* 37 (2012) 106-126.
- [115] Y. Deng, A. Shavandi, O.V. Okoro, L. Nie, Alginate modification via click chemistry for biomedical applications, *Carbohydrate Polymers* (2021) 118360.
- [116] Z. Majidnia, A. Idris, Evaluation of cesium removal from radioactive waste water using maghemite PVA–alginate beads, *Chemical engineering journal* 262 (2015) 372-382.
- [117] M.E. Mahmoud, M.M. Saleh, M.M. Zaki, G.M. Nabil, A sustainable nanocomposite for removal of heavy metals from water based on crosslinked sodium alginate with iron oxide waste material from steel industry, *Journal of Environmental Chemical Engineering* 8 (2020) 104015.
- [118] Z. Majidnia, A. Idris, M. Majid, R. Zin, M. Ponraj, Efficiency of barium removal from

- radioactive waste water using the combination of maghemite and titania nanoparticles in PVA and alginate beads, *Applied Radiation and Isotopes* 105 (2015) 105-113.
- [119] J. Girón-Hernández, P. Gentile, M. Benlloch-Tinoco, Impact of heterogeneously crosslinked calcium alginate networks on the encapsulation of  $\beta$ -carotene-loaded beads, *Carbohydrate Polymers* (2021) 118429.
- [120] B. Lupo, A. Maestro, J.M. Gutiérrez, C. González, Characterization of alginate beads with encapsulated cocoa extract to prepare functional food: Comparison of two gelation mechanisms, *Food Hydrocolloids* 49 (2015) 25-34.
- [121] S. Wichchukit, M. Oztop, M. McCarthy, K. McCarthy, Whey protein/alginate beads as carriers of a bioactive component, *Food Hydrocolloids* 33 (2013) 66-73.
- [122] J. Guo, J. Jiang, X. Gu, X. Li, T. Liu, Encapsulation of  $\beta$ -carotene in calcium alginate hydrogels templated by oil-in-water-in-oil (O/W/O) double emulsions, *Colloids and Surfaces A: Physicochemical and Engineering Aspects* 608 (2021) 125548.
- [123] N. Gorbunova, A. Bannikova, A. Evteev, I. Evdokimov, S. Kasapis, Alginate-based encapsulation of extracts from beta Vulgaris cv. beet greens: Stability and controlled release under simulated gastrointestinal conditions, *LWT* 93 (2018) 442-449.
- [124] A. Doderò, L. Pianella, S. Vicini, M. Alloisio, M. Ottonelli, M. Castellano, Alginate-based hydrogels prepared via ionic gelation: An experimental design approach to predict the crosslinking degree, *European Polymer Journal* 118 (2019) 586-594.
- [125] J.P. Paques, Alginate nanospheres prepared by internal or external gelation with nanoparticles, *Microencapsulation and microspheres for food applications*, Elsevier 2015, pp. 39-55.
- [126] Ý.A. Mørch, I. Donati, B.L. Strand, G. Skjak-Bræk, Effect of  $\text{Ca}^{2+}$ ,  $\text{Ba}^{2+}$ , and  $\text{Sr}^{2+}$  on alginate microbeads, *Biomacromolecules* 7 (2006) 1471-1480.
- [127] L. Hu, D. Kong, Q. Hu, X. Yang, H. Xu, Preparation and optimization of a novel microbead formulation to improve solubility and stability of curcumin, *Particulate Science and Technology* 35 (2017) 448-454.
- [128] S.-F. Lin, Y.-C. Chen, R.-N. Chen, L.-C. Chen, H.-O. Ho, Y.-H. Tsung, M.-T. Sheu, D.-Z. Liu, Improving the stability of astaxanthin by microencapsulation in calcium alginate

beads, PLoS One 11 (2016) e0153685.

[129] C.K. Kuo, P.X. Ma, Ionically crosslinked alginate hydrogels as scaffolds for tissue engineering: Part 1. Structure, gelation rate and mechanical properties, *Biomaterials* 22 (2001) 511-521.

[130] L.W. Chan, H.Y. Lee, P.W. Heng, Mechanisms of external and internal gelation and their impact on the functions of alginate as a coat and delivery system, *Carbohydrate Polymers* 63 (2006) 176-187.

[131] I. Donati, S. Paoletti, Material properties of alginates, *Alginates: Biology and applications*, Springer 2009, pp. 1-53.

[132] X. Liu, W. Yu, Y. Zhang, W. Xue, W. Yu, Y. Xiong, X. Ma, Y. Chen, Q. Yuan, Characterization of structure and diffusion behaviour of Ca-alginate beads prepared with external or internal calcium sources, *Journal of microencapsulation* 19 (2002) 775-782.

[133] J.M.C. Puguan, X. Yu, H. Kim, Characterization of structure, physico-chemical properties and diffusion behavior of Ca-Alginate gel beads prepared by different gelation methods, *Journal of colloid and interface science* 432 (2014) 109-116.

[134] J.M. Radovich, Mass transfer effects in fermentations using immobilized whole cells, *Enzyme and microbial technology* 7 (1985) 2-10.

[135] D. Poncelet, B.P. De Smet, C. Beaulieu, M. Huguet, A. Fournier, R. Neufeld, Production of alginate beads by emulsification/internal gelation. II. Physicochemistry, *Applied Microbiology and Biotechnology* 43 (1995) 644-650.

[136] J. Jang, Y.-J. Seol, H.J. Kim, J. Kundu, S.W. Kim, D.-W. Cho, Effects of alginate hydrogel cross-linking density on mechanical and biological behaviors for tissue engineering, *Journal of the mechanical behavior of biomedical materials* 37 (2014) 69-77.

[137] H. Song, W. Yu, M. Gao, X. Liu, X. Ma, Microencapsulated probiotics using emulsification technique coupled with internal or external gelation process, *Carbohydrate polymers* 96 (2013) 181-189.

[138] S. Cai, M. Zhao, Y. Fang, K. Nishinari, G.O. Phillips, F. Jiang, Microencapsulation of *Lactobacillus acidophilus* CGMCC1.2686 via emulsification/internal gelation of alginate using Ca-EDTA and CaCO<sub>3</sub> as calcium sources, *Food hydrocolloids* 39 (2014) 295-300.

- [139] M.M. Ahmed, S. Abd El-Rasoul, S.H. Auda, M.A. Ibrahim, Emulsification/internal gelation as a method for preparation of diclofenac sodium–sodium alginate microparticles, *Saudi Pharmaceutical Journal* 21 (2013) 61-69.
- [140] L. Chen, M. Subirade, Effect of preparation conditions on the nutrient release properties of alginate–whey protein granular microspheres, *European Journal of Pharmaceutics and Biopharmaceutics* 65 (2007) 354-362.
- [141] M. Alnaief, M. Alzaitoun, C. García-González, I. Smirnova, Preparation of biodegradable nanoporous microspherical aerogel based on alginate, *Carbohydrate Polymers* 84 (2011) 1011-1018.
- [142] I.F. Farrés, I. Norton, Formation kinetics and rheology of alginate fluid gels produced by in-situ calcium release, *Food Hydrocolloids* 40 (2014) 76-84.
- [143] A. Ström, P. Ribelles, L. Lundin, I. Norton, E.R. Morris, M.A. Williams, Influence of pectin fine structure on the mechanical properties of calcium–pectin and acid–pectin gels, *Biomacromolecules* 8 (2007) 2668-2674.
- [144] T. Ramdhan, S.H. Ching, S. Prakash, B. Bhandari, Time dependent gelling properties of cuboid alginate gels made by external gelation method: Effects of alginate-CaCl<sub>2</sub> solution ratios and pH, *Food Hydrocolloids* 90 (2019) 232-240.
- [145] S.J. Bidarra, C.C. Barrias, P.L. Granja, Injectable alginate hydrogels for cell delivery in tissue engineering, *Acta biomaterialia* 10 (2014) 1646-1662.
- [146] K.I. Draget, K. Østgaard, O. Smidsrød, Homogeneous alginate gels: A technical approach, *Carbohydrate polymers* 14 (1990) 159-178.
- [147] E. Secchi, F. Munarin, M.D. Alaimo, S. Bosisio, S. Buzzaccaro, G. Ciccarella, V. Vergaro, P. Petrini, R. Piazza, External and internal gelation of pectin solutions: microscopic dynamics versus macroscopic rheology, *Journal of Physics: Condensed Matter* 26 (2014) 464106.
- [148] H.R. Moreira, F. Munarin, R. Gentilini, L. Visai, P.L. Granja, M.C. Tanzi, P. Petrini, Injectable pectin hydrogels produced by internal gelation: pH dependence of gelling and rheological properties, *Carbohydrate polymers* 103 (2014) 339-347.
- [149] E. Pariset, C. Pudda, F. Boizot, N. Verplanck, F. Revol-Cavalier, J. Berthier, A.

- Thuair, V. Agache, Purification of complex samples: Implementation of a modular and reconfigurable droplet-based microfluidic platform with cascaded deterministic lateral displacement separation modules, *Plos one* 13 (2018) e0197629.
- [150] S. Utech, R. Prodanovic, A.S. Mao, R. Ostafe, D.J. Mooney, D.A. Weitz, Microfluidic generation of monodisperse, structurally homogeneous alginate microgels for cell encapsulation and 3D cell culture, *Advanced healthcare materials* 4 (2015) 1628-1633.
- [151] N. Paiboon, S. Surassmo, U.R. Ruktanonchai, A. Soottitantawat, Hydrodynamic control of droplet formation in narrowing jet and tip streaming regime using microfluidic flow-focusing, *International Journal of Multiphase Flow* (2022) 104013.
- [152] S. Leclercq, K.R. Harlander, G.A. Reineccius, Formation and characterization of microcapsules by complex coacervation with liquid or solid aroma cores, *Flavour and Fragrance Journal* 24 (2009) 17-24.
- [153] B.K. Azagheswari, S. Padma, S.P. Priya, A review on microcapsules, *Global Journal of Pharmacology* 9 (2015) 28-39.
- [154] B. Pena, C. Panisello, G. Aresté, R. Garcia-Valls, T. Gumí, Preparation and characterization of polysulfone microcapsules for perfume release, *Chemical Engineering Journal* 179 (2012) 394-403.
- [155] H. Lee, C.-H. Choi, A. Abbaspourrad, C. Wesner, M. Caggioni, T. Zhu, D.A. Weitz, Encapsulation and enhanced retention of fragrance in polymer microcapsules, *ACS applied materials & interfaces* 8 (2016) 4007-4013.
- [156] P.B. O'Donnell, J.W. McGinity, Preparation of microspheres by the solvent evaporation technique, *Advanced drug delivery reviews* 28 (1997) 25-42.
- [157] A. Abbaspourrad, S.S. Datta, D.A. Weitz, Controlling release from pH-responsive microcapsules, *Langmuir* 29 (2013) 12697-12702.
- [158] W. Wang, G.I. Waterhouse, D. Sun-Waterhouse, Co-extrusion encapsulation of canola oil with alginate: Effect of quercetin addition to oil core and pectin addition to alginate shell on oil stability, *Food research international* 54 (2013) 837-851.
- [159] D. Sun-Waterhouse, J. Zhou, G. Miskelly, R. Wibisono, S. Wadhwa, Stability of encapsulated olive oil in the presence of caffeic acid, *Food Chemistry* 126 (2011) 1049-

1056.

- [160] E. Martins, D. Renard, J. Davy, M. Marquis, D. Poncelet, Oil core microcapsules by inverse gelation technique, *Journal of microencapsulation* 32 (2015) 86-95.
- [161] E. Martins, D. Poncelet, D. Renard, A novel method of oil encapsulation in core-shell alginate microcapsules by dispersion-inverse gelation technique, *Reactive and Functional Polymers* 114 (2017) 49-57.
- [162] A.S. Utada, E. Lorenceau, D.R. Link, P.D. Kaplan, H.A. Stone, D. Weitz, Monodisperse double emulsions generated from a microcapillary device, *Science* 308 (2005) 537-541.
- [163] S.A. Nabavi, G.T. Vladisavljević, S. Gu, E.E. Ekanem, Double emulsion production in glass capillary microfluidic device: Parametric investigation of droplet generation behaviour, *Chemical Engineering Science* 130 (2015) 183-196.
- [164] S.H. Kim, D.A. Weitz, One-step emulsification of multiple concentric shells with capillary microfluidic devices, *Angewandte Chemie* 123 (2011) 8890-8893.
- [165] S.A. Nabavi, G.T. Vladisavljević, V. Manović, Mechanisms and control of single-step microfluidic generation of multi-core double emulsion droplets, *Chemical Engineering Journal* 322 (2017) 140-148.
- [166] S.A. Nabavi, G.T. Vladisavljević, M.V. Bandulasena, O. Arjmandi-Tash, V. Manović, Prediction and control of drop formation modes in microfluidic generation of double emulsions by single-step emulsification, *Journal of colloid and interface science* 505 (2017) 315-324.
- [167] Q.-Q. Liao, S.-K. Zhao, B. Cai, R.-X. He, L. Rao, Y. Wu, S.-S. Guo, Q.-Y. Liu, W. Liu, X.-Z. Zhao, Biocompatible fabrication of cell-laden calcium alginate microbeads using microfluidic double flow-focusing device, *Sensors and Actuators A: Physical* 279 (2018) 313-320.
- [168] W.-T. Wang, R. Chen, J.-H. Xu, Y.-D. Wang, G.-S. Luo, One-step microfluidic production of gas-in-water-in-oil multi-cores double emulsions, *Chemical Engineering Journal* 263 (2015) 412-418.
- [169] A. Abate, D. Weitz, High-order multiple emulsions formed in poly (dimethylsiloxane)

microfluidics, Small 5 (2009) 2030-2032.







จุฬาลงกรณ์มหาวิทยาลัย  
**CHULALONGKORN UNIVERSITY**

## VITA

**NAME** Narin Paiboon

**DATE OF BIRTH** 31 October 1990

**PLACE OF BIRTH** Nonthaburi, Thailand

**INSTITUTIONS ATTENDED** Master of Engineering: Chemical Engineering, 2013-2016,  
Chulalongkorn University, Thailand  
Bachelor of Science: Chemical Technology, 2009-2013,  
Chulalongkorn University, Thailand

**HOME ADDRESS** Nonthaburi, Thailand

**PUBLICATION**

1. Paiboon, N., Surassmo, S., Ruktanonchai, U.R., Soottitantawat, A., 2022. Hydrodynamic control of droplet formation in narrowing jet and tip streaming regime using microfluidic flow-focusing. *International Journal of Multiphase Flow*, 104013.
2. Paiboon, N., Surassmo, S., Ruktanonchai, U.R., Kappl, M., Soottitantawat, A., Internal gelation of alginate microparticle prepared by emulsification and microfluidic method: Effect of Ca-EDTA as a calcium source. Submitted to *Colloids and Surfaces A : Physicochemical and Engineering Aspects*.
3. Paiboon N., Surassmo S., Ruktanonchai U.R., Soottitantawat A. Microdroplet Generation in Microfluidic Flow-focusing Device. Present at the oral presentation of 18th Asian Pacific Confederation of Chemical Engineering Congress: APCCHE 2019, Sapporo, Japan.
4. Paiboon N., Surassmo S., Ruktanonchai U.R., Soottitantawat A. Fundamental Study on Throughput Properties of Microfluidics Synthesis for Polymeric Micro-Nanoparticles. Present at the poster presentation of The 6th Joint Conference on Renewable Energy and Nanotechnology: JCREN 2017, Bangkok, Thailand.